Parson, L., Hawkins, J., Allan, J., et al., 1992
Proceedings of the Ocean Drilling Program, Initial Reports, Vol. 135

6. SITE 836[1]

Shipboard Scientific Party[2]

HOLE 836A

Date occupied: 6 January 1991

Date departed: 7 January 1991

Time on hole: 1 day, 3 hr, 42 min

Position: 20°08.494′S, 176°30.008′W

Bottom felt (rig floor; m, drill-pipe measurement): 2466.3

Distance between rig floor and sea level (m): 10.90

Water depth (drill-pipe measurement from sea level, m): 2455.4

Total depth (rig floor; m): 2504.5

Penetration (m): 38.20

Number of cores (including cores with no recovery): 9

Total length of cored section (m): 38.20

Total core recovered (m): 24.46

Core recovery (%): 64.1

Oldest sediment cored:
Depth (mbsf): 22.8
Nature: nannofossil ooze with foraminifers
Earliest age: middle Pleistocene
Measured velocity (km/s): 1.5

Hard rock:
Depth (mbsf): 25.7
Nature: basalt
Measured velocity (km/s): 4.60–4.75

Basement:
Depth (mbsf): 25.7
Nature: basalt
Measured velocity (km/s): 4.60–4.75

HOLE 836B

Date occupied: 7 January 1991

Date departed: 8 January 1991

Time on hole: 1 day, 6 hr, 30 min

Position: 20°08.505′S, 176°30.011′W

Bottom felt (rig floor; m, drill-pipe measurement): 2468.5

Distance between rig floor and sea level (m): 10.80

Water depth (drill-pipe measurement from sea level, m): 2457.7

Total depth (rig floor; m): 2526.80

Penetration (m): 58.30

Number of cores (including cores with no recovery): 8

Total length of cored section (m): 44.8

Total core recovered (m): 17.00

Core recovery (%): 37.9

Oldest sediment cored:
Depth (mbsf): 23.60
Nature: vitric claystone
Earliest age: middle Pleistocene
Measured velocity (km/s): 3.91–4.79

Hard rock:
Depth (mbsf): 23.60
Nature: basalt

Basement:
Depth (mbsf): 23.60
Nature: basalt
Measured velocity (km/s): 3.91–4.79

Principal results: Site 836 is located in the western Lau Basin about 220 km east of the Lau Ridge and about 48 km west of the Eastern Lau Spreading Center (ELSC). The Lau Ridge is the remnant arc of the trench-arc-backarc system related to the convergent plate margin of the Tonga Trench. The ELSC is the present locus of crustal generation caused by seafloor spreading processes in the Lau Basin at the latitude of Site 836. Site 836 is in a small, elongated, oval-shaped basin for which we use the informal name "Basin 836" in this discussion. Basin 836 trends north-northeast (020°), and is about 20 km long and about 5 km wide in a north-northwest direction at the 2400-m isobath. It is one of a number of linear depressions bounded on the west and east by discontinuous ridges that we interpret as horsts separating grabens and half grabens, although we lack data to delineate faults that may control their form. The ridge on the west side of Basin 836 has an irregular crest line with several small peaks rising to <1900 m. The ridge on the east side rises to <1500 m. It has a northwesterly trend and appears to be part of an en echelon ridge system. The maximum depth of Basin 836 is in a narrow elongated area near the center that is in excess of 2500 m deep.

Site surveys provided seismic and bathymetric data to help select the drill site, but as discussed in the "Background and Objectives" section (this chapter), the seismic reflection data proved difficult to interpret. Our interpretation of these records is that the data may show a thin sediment cover or indicate scatter from a bare rock basement swept clean of sediment by bottom currents. Unlike the other sites in the western Lau Basin, Site 836 showed little or no seismic layering that could be assigned to either seismic Units A or B. Magnetic anomaly data in the area have also proved difficult to interpret, and ages ranging from about 2 Ma to about 1 Ma have been inferred for the area near Basin 836. Site 836 was selected as a likely place to sample crust that had formed shortly after a postulated ridge jump or initiation of a new ridge at the present location of the ELSC.

A tabulation of some of the results from Site 836 is provided in Figure 1. The sedimentary sequence at Site 836 was sampled only through the mid-Pleistocene to 20.8 m below seafloor (mbsf). The sequence is distinguished by an abundance of volcaniclastic material at all depths but in particular in the deeper levels of the core from about 12 mbsf downward. The uppermost 12 m are hemipelagic deposits, mostly dark brown to brown clayey nannofossil ooze interbedded with volcaniclastic sediments. They may contain up to 25 volume% interspersed glass shards and are commonly mottled by bioturbation. Rapid deposition of volcaniclastic sediments that make up as much as 50% of the lower half of the hole, with individual layers as thick as 1 m, started soon after the end of volcanism that formed the igneous basement, at perhaps 0.5 Ma. The volcanic-derived sediments came from a basaltic andesite source (55%–56% SiO_2), as shown by shipboard chemical analyses by X-ray fluorescence (XRF)

[1] Parson, L., Hawkins, J., Allan, J., et al., 1992. *Proc. ODP, Init. Repts.*, 135: Ocean Drilling Program (College Station, TX).
[2] Shipboard Scientific Party is as given in the list of participants preceding the contents.

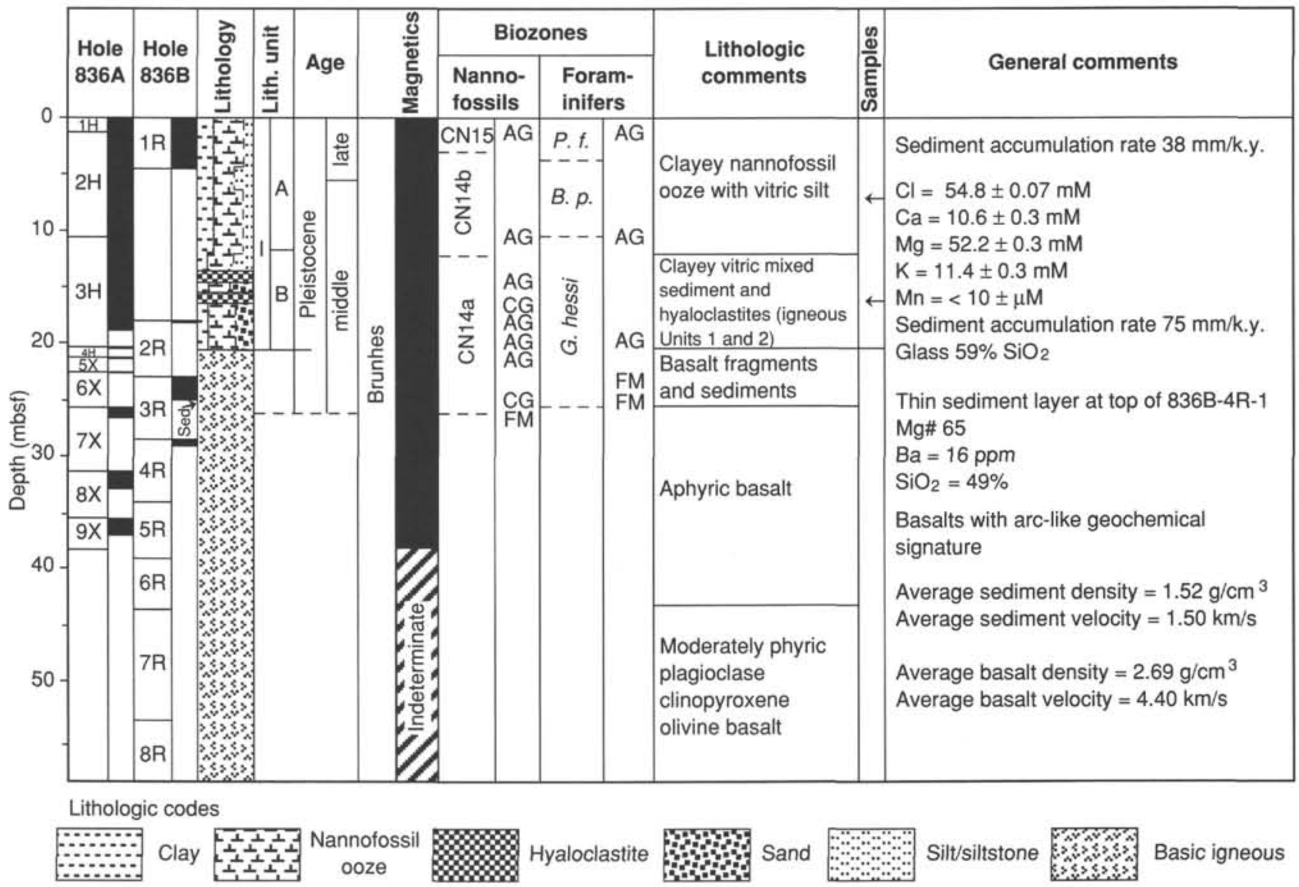

Figure 1. Site summary, Site 836. Abbreviations for abundance are as follows: A = abundant, C = common, F = few, R = rare, and B = barren. Those for preservation are as follows: G = good, M = moderate, and P = poor. Planktonic foraminifer zones are abbreviated as follows: *P. f.* = *Pulleniatina finalis*, *B. p.* = *Bolliella praeadamsi*, and *G. hessi* = *Globorotalia crassaformis hessi*.

and refractive index studies. Many of the glass shards are medium brown with blocky to angular shapes and low to intermediate vesicularity. They are interpreted as indicating derivation from spalling of glassy rinds of pillowed flows or sheet flows or both to form hyaloclastites. It is likely that the source of the volcanic detritus was <10 km from the site of deposition. There was negligible input of turbidites carrying silicic shards.

The biostratigraphic and paleomagnetic data indicate that only the middle and late parts of the Pleistocene, all within the Brunhes Normal Polarity Chron (0.73 Ma), are present in the Site 836 sediments. The calcareous nannofossil flora indicate Zone CN15 (e.g., *Emiliania huxleyi*) and Subzones CN14a (e.g., *Gephyrocapsa oceanica*) and CN14b (e.g., *Emiliania ovata*). The planktonic foraminifers are abundant and well preserved; Zones N23 (e.g., *Pulleniatina finalis*) and N22 (e.g., *Bolliella praeadamsi*) and *Globorotalia* (*Truncorotalia*) *crassaformis hessi* are present. The sediment sequence consists of calcareous oozes with interbedded coarse volcanic ash horizons; the amount of volcanic material greatly increases downcore, beginning with Core 135-836A-3H. The calcareous planktonic assemblages in the Pleistocene oozes and volcanic ash sands are very well preserved, but diversity and preservation deteriorate in sediments associated with the igneous rocks. The sediment accumulation rates determined for Site 836 may be separated into two parts that reflect the differences in the volcaniclastic component. The sediments accumulated before 0.5 Ma have a thick volcaniclastic component and represent that part of the section overlying and interbedded with the mafic igneous rocks. A sediment accumulation rate of 75 mm/k.y. is indicated. The younger part of the sediment column, <0.5 Ma in age, has a lesser volcanic component with an estimated sediment accumulation rate of around 25 mm/k.y.

Sediments recovered in Cores 135-836A-1H through -3H, as well as basaltic and basaltic andesite rocks from Cores 135-836A-7X through -9X, were all normally polarized and evidently formed during the Brunhes Normal Polarity Chron (i.e., in the last 0.73 m.y.). Magnetic susceptibility in the sediment column of Hole 836A displayed small oscillations that may be related to Milankovitch climate cycles. Magnetic susceptibility in the basalts recovered in Holes 836A and 836B is about 50% higher in Units 3 and 4 than in Unit 5; this implies a slight compositional difference and that the former contain more magnetic minerals.

The shipboard analyses for hydrocarbons in the sediments of Site 836 indicated methane concentrations on the order of 2–3 ppm, which was considered to be the background level. No ethane or propane was detected. The extremely low concentration of methane indicates that methanogenesis was not occurring in these sediments. This would be expected because of the shallow sediment depths penetrated and because it is extremely unlikely that the bottom waters were anoxic in an open-ocean setting. The $CaCO_3$ percentage was calculated from a determination of inorganic carbon measured on selected samples and gave values ranging from 15.7% to 56.3%. Total organic carbon was calculated from the difference between total carbon and inorganic carbon and produced values that range from 0.07% to 0.53%. Sulfur ranged from 0.01% to 0.07%.

Five igneous rock units were identified on the basis of mineralogy, mineral proportions, and texture. The two uppermost units are glassy, sparsely phyric, andesitic hyaloclastites. Underlying these andesitic rocks are three basalt units: moderately phyric olivine-plagioclase basalt; sparsely phyric plagioclase basalt; and moderately phyric olivine-clinopyroxene-plagioclase basalt. All of the units are highly vesicular, with up to 40% vesicles in some samples, indicating a high volatile content of the parental magmas. Trace and minor element data suggest that the samples all have an arc-like geochemical signature and are distinct from lavas erupted at the nearby ELSC. In spite of the arc-like signature, they also are distinctly different from the modern lavas of the Tofua Arc.

The GRAPE and *P*-wave logger data show a good correlation of the hyaloclastite layers to measured values of high density and high velocity in the sediment section. Marked variations in basalt *P*-wave velocities could be a result of alteration or could represent the variable vesicularity of the samples.

BACKGROUND AND OBJECTIVES

Introduction

The geographical proximity of the Sites 836, 837, 838, and 839 to each other, and the similarity of their objectives, allow consideration of their background and objectives together. To avoid repetition, a summary of the principal rationale and background for the selection of all four sites is presented below; more detailed syntheses of tectonic and geophysical setting of individual sites is included with each of the following site chapters.

Geologic Setting of Sites 836 through 839

Sites 836, 837, 838, and 839 (Fig. 2) are all in the west central Lau Basin bounded by longitudes 176°30′W and 177°00′W and by latitudes 20°00′S and 21°00′S. We will informally refer to this area as the central Lau Basin for purposes of this discussion. All of the sites share a common geologic history and, rather than repeat it in each of the subsequent site descriptions, we present here a summary of the geologic setting that applies to all four sites.

On a regional scale, the submarine topography of this part of the Lau Basin is characterized by a series of upstanding crustal blocks that possess a variety of dimensions. These blocks are as much as 80 km long and range from 4 to 35 km wide. The blocks are aligned on north-south to northeast-southwest trends, between the strike of the ELSC and that of the Lau Ridge (Parson et al., this volume). The high standing blocks separate troughs and linear basins that have dimensions comparable to the shoal areas. Site 836 is located centrally to an elongated north-northeast-trending basin flanked to the west by 500-m high scarps, with more subdued topography to the east. We refer to the trough informally as Basin 836 (Fig. 3). To the east of longitude 176°45′W, the seafloor morphology is dominated by a less dramatic topographic grain, defined by regular, linear scarps and ridges closely spaced at intervals between 1 and 5 km, and locally continuous over lengths of up to 25 km. This fabric continues eastward and merges imperceptibly with the neotectonic faulting associated with the ELSC. This contrast in seafloor fabric can be traced along a line running approximately north-south that approaches the southern termination of the Central Lau Spreading Center (CLSC) to the north, and extends southward into the unsurveyed south-central portion of the Lau Basin. As discussed elsewhere (Parson et al., this volume), a major break in style of crustal formation occurs across this zone of contrasting seafloor fabric.

Several estimates for the age of the crust in this area have been made using magnetic anomaly data, yielding ages of about 1–2 Ma. The magnetic profiles, however, have proved difficult to interpret in terms of understanding the regional tectonic/magnetic fabric and the evolutionary history of the sites. Two general trends are suggested by the data as shown in Figure 4. East of 177°W, including the area of Basins 836–839, there is a north-northeast (025°) trend to the anomalies; west of 177°W, a lack of data makes the pattern less distinct but there is a suggestion of a more northerly (010°) trend to the anomalies (Lawver et al., 1976). The 020°–025° trend of the anomalies is comparable with the present strike of the ELSC at this latitude. The northeastern trends are identified as representing the Jaramillo magnetic event (Malahoff et al., in press) and are related to the seafloor spreading process. Murthy (1990) places the location of the Jaramillo Event so that Site 836 overlies the older, western edge of the anomaly (i.e., at the reversed to normal transition), thereby suggesting that the age of the crust beneath 836 is about 1 Ma. As discussed in the "Introduction and Principal Results" chapter, the northerly trends to the west of the sites may not be direct correlatives with anomalies generated by seafloor spreading. There are two heat flow stations in this area; a heat flow value of 1.04 $\mu cal/cm^2$ sec was measured at a site near 20°20′S, 176°48′W, about 22 km south of Site 837, and a value of 0.60 $\mu cal/cm^2$ sec was measured at a site near 20°00′S, 176°43′W, about 22 km northwest of Site 836 (Sclater, 1972).

An extensive collection exists of fresh MORB-like tholeiitic basalt from the ELSC (e.g., Hawkins, 1989; Ernewein et al., in press), but only three dredge collections exist from within the general area around these drill sites. One collection from a scarp 16 km from Site 837 on the northeastern side of Basin 837 comprises tholeiitic basalt transitional in trace and minor element chemistry between MORB and arc tholeiite (dredge Site RNDB 15-2, Hawkins, 1989); a similar rock type was collected from a west-facing ridge slope 22 km southeast of Site 837 (dredge Site ANT-223, Hawkins, 1976; Hawkins and Melchior, 1985). The other collection (dredge Site ANT-221, Hawkins, 1976) is of broadly andesitic volcaniclastic material that was collected from a ridge slope 95 km south of Site 839.

The ELSC is the closest major morphotectonic feature lying to the east of the central basin drill sites (Parson et al., 1990). The ELSC can be traced for over 180 km from near 19°20′S at longitude 175°55′W to about 21°S where it merges with the Valu Fa Ridge. The ELSC has a well-defined central rift zone 5–10 km wide, characterized on high-resolution seismic profiles and echosounder profiles by a strong acoustic return interpreted as bare rock, or thinly sedimented extrusive seafloor. GLORIA sidescan sonar data image the axial zone as a wider, strongly backscattering region up to 20 km wide, cut by axial-parallel fault scarps. SeaBeam data show that the axial zone separates major rift mountain walls that rise as much as 500 m (to depths of about 2200 m) above the axial valley floor. Inward-facing fault scarps form a series of small terraces that step down to the axial floor; in some places the innermost part of the axial zone is a 1.5–3 km wide notch about 50–100 m deep. The axial floor of the ELSC is at a depth of about 2600 m near 19°40′S and deepens to over 2700 m near 20°20′S. It is thinly sedimented and fresh basalt glasses have been dredged along the axis between 19°20′S and 21°00′S (Hawkins et al., 1989: Ernewein et al., in press). Magnetic anomaly data, together with the fresh glass and aphyric rock dredged from the axial zone, support the interpretation that it is a young active zone of rifting and magmatism.

Site 836

Location and Bathymetry

Site 836 is located in the central Lau Basin approximately 220 km east of the axis of the Lau Ridge and about 50 km west of the active axial ridge of the ELSC (Fig. 2). It is situated in 2441 m of water at 20°08.5′S, 176°30.1′W. The age of the crust at the site was inferred to be approximately 1 m.y., from an interpretation of the regional magnetic and tectonic fabric (Parson et al., 1990). The drill site is in one of many small basins, having a general north-northeast trend, that characterize the central and western parts of the Lau Basin (see Fig. 2 in the "Introduction and Principal Results" chapter, this volume). We will use the informal name "Basin 836" in our discussion of the drill site.

Basin 836 (Fig. 3) extends about 20 km in a north-northeast direction and is about 5 km wide; these dimensions were taken at

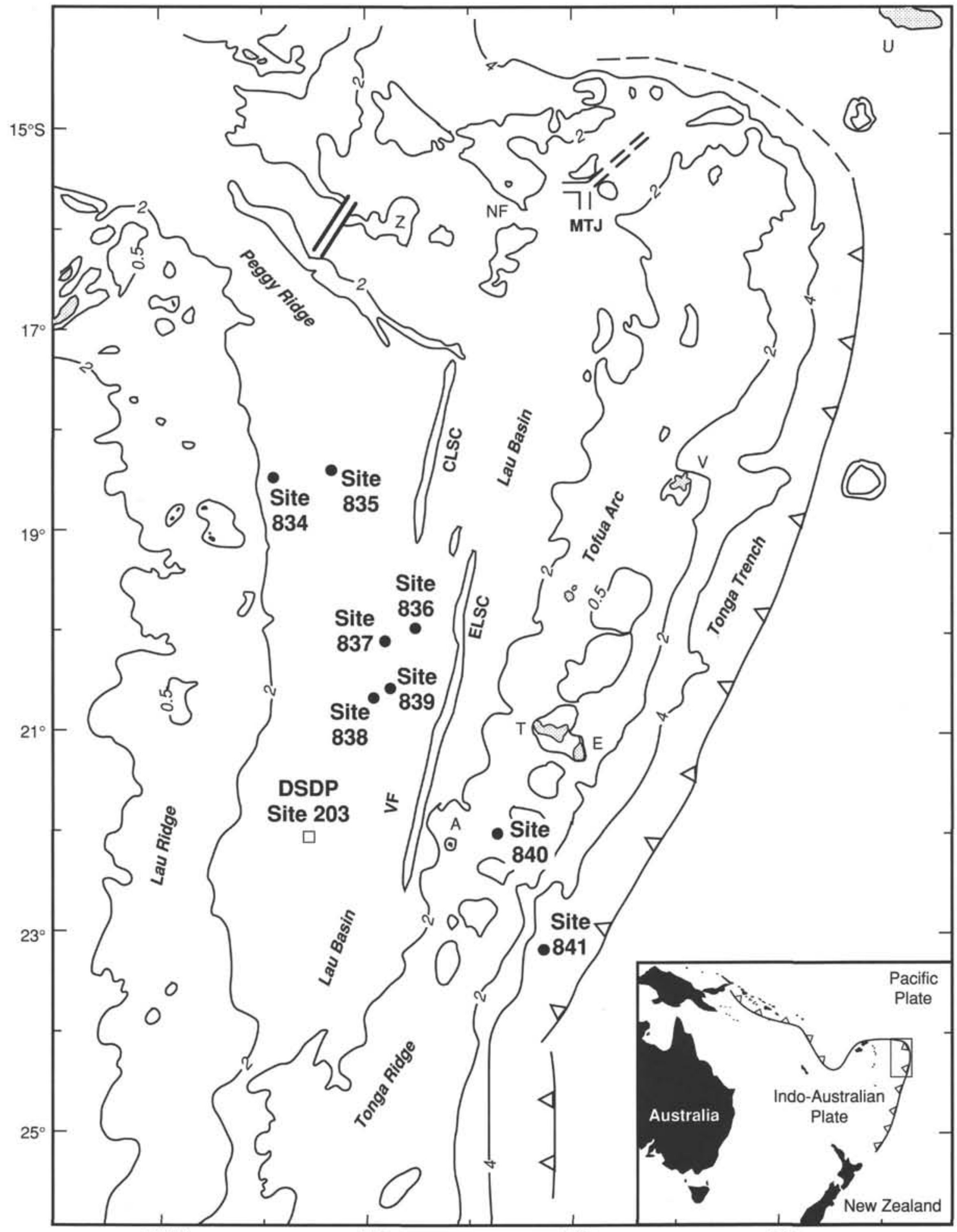

Figure 2. Regional bathymetry of the Lau Basin and location of Site 836. Also illustrated are the regional setting for the other drill site locations in the Lau Basin and the major geologic features of the Tonga Trench and Lau Basin system. Z = Zephyr Shoal; islands include T = Tongatapu, E = 'Eua, V = Vavau, NF = Niua Fo'ou, A = Ata, and U = Upolu. The locations of the Central Lau (CLSC) and Eastern Lau (ELSC) spreading centers, Valu Fa Ridge (VF), and Mangatolu Triple Junction (MTJ) are from von Stackelberg (1990), Parson et al. (1989), Hawkins et al. (1989), and Nilsson et al. (1989). The location of DSDP Site 203 is shown as an open square. Contours in thousands of meters.

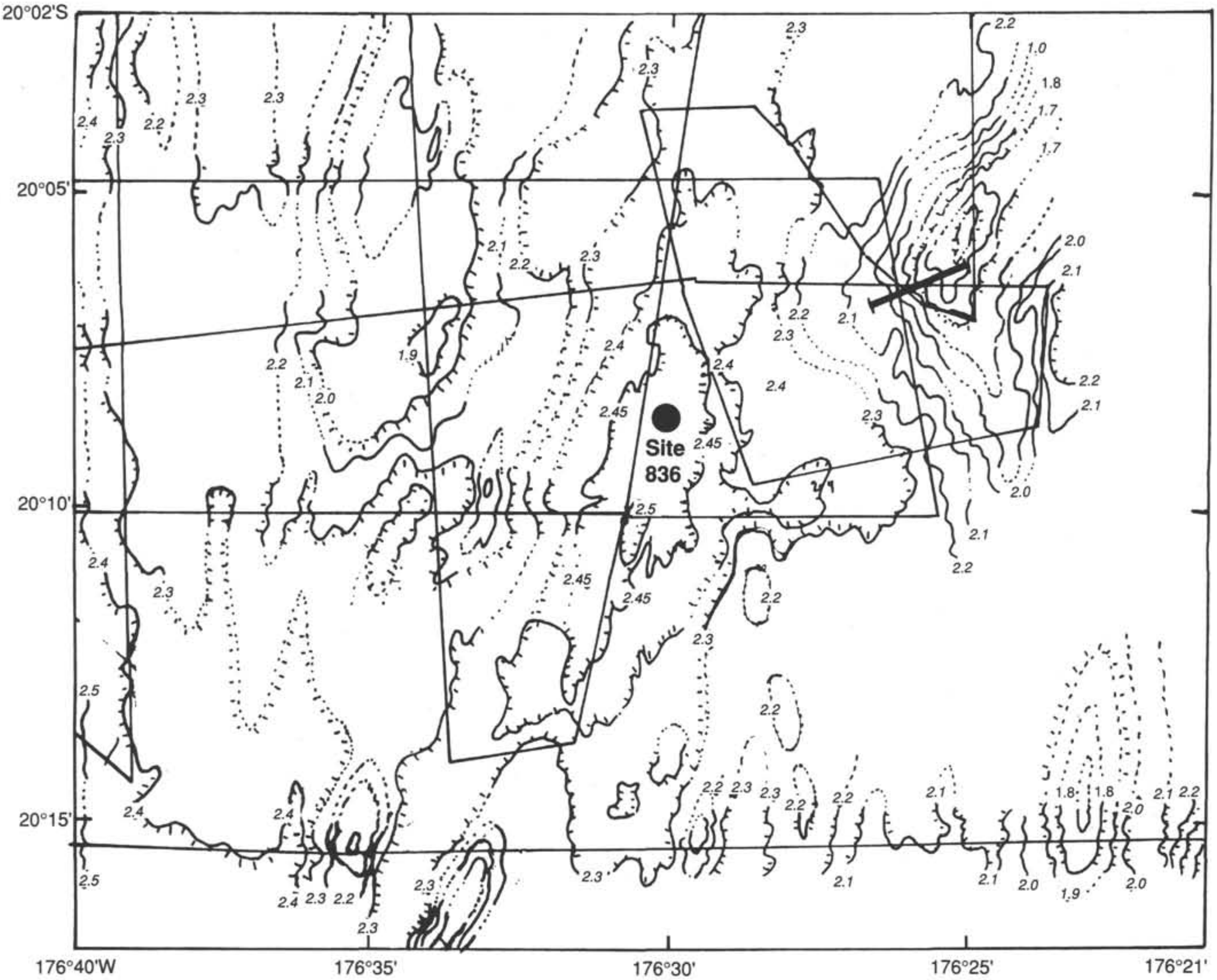

Figure 3. Bathymetric sketch chart showing the location of Site 836 in the western Lau Basin. The chart has been compiled from multibeam swath bathymetry, seismic reflection profiles, and conventional echo-sounder data (tracks as fine lines). Contours in thousands of meters. Dredge haul RNDB-15-2 marked as a bold line (after Hawkins, 1989).

the 2400-m isobath, which defines a narrow oval-shaped basin with minor spurs and embayments along its perimeter. The ridge on the northwestern side of the basin has an irregular crest, parts of which shoal to <1900 m. The deepest part of the basin surveyed is a small elongate area between 2500 and 2600 m in depth that parallels the basin margins. The eastern side of the basin is bordered by several large irregular seamounts, or uplifted blocks of seafloor, that appear to be arranged in a crude en echelon fashion. These masses trend northwesterly and their irregular summit ridges rise to <1500 m depth (Figs. 3 and 5).

Regional Structural Synthesis

Basin 836 is bounded on the east and west by ridges rising to depths <2000 m. We suggest that these ridges are horsts separating half-grabens, although we lack data to delineate the nature of the faults controlling their geometry (Fig. 3). There are no data to indicate the composition of the ridges to the west of Site 836 but rocks from the ridge forming the high standing block 7.5 km northeast of the site are relatively unaltered, moderately fractionated basalts (dredge Site RNDB-15-2, 20°06.4′S, 176°26.6′W; J. W. Hawkins, unpubl. data, 1991). The southwestern side of the northeastern block is cut by a northwesterly trending scarp, defining a rhomb-shaped block in contrast to the more linear ridges to the west of Basin 836. The tectonic interpretation of Parson et al. (1990) predicts that the northeastern ridge, and perhaps the ridges on both sides of the basin, are remnants of the earliest crust formed on the western flank of the ELSC. The site was selected to sample crust that was formed shortly after the spreading center had made a ridge jump to the east from a postulated former location, approximately 55 km to the west.

Geologic Setting

Site 836 is located on crust that was estimated to be <1 m.y. old on the basis of interpretations of regional magnetic anomaly patterns by Weissel (1977) and Malahoff et al. (in press), but was estimated to be about 1 m.y. old according to Murthy (1990; and see Fig. 4). Although no samples of the crust near this site had been collected, it was assumed that the seafloor would be basalt overlain by a thin cover of clayey carbonate ooze. The site lies between the active axial zone of the ELSC, where tholeiitic basalt

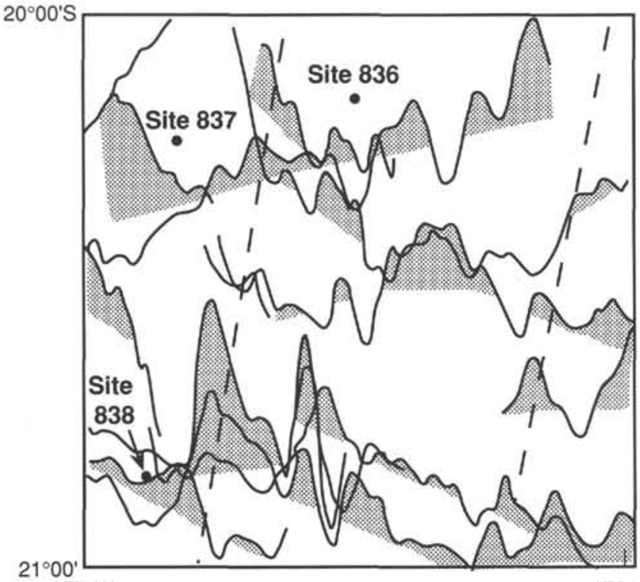

Figure 4. Sketch map illustrating available magnetic anomaly data. Maximum anomalies do not exceed 250 nT. General trend of lineaments is suggested by dashed lines, but overall correlation is poor.

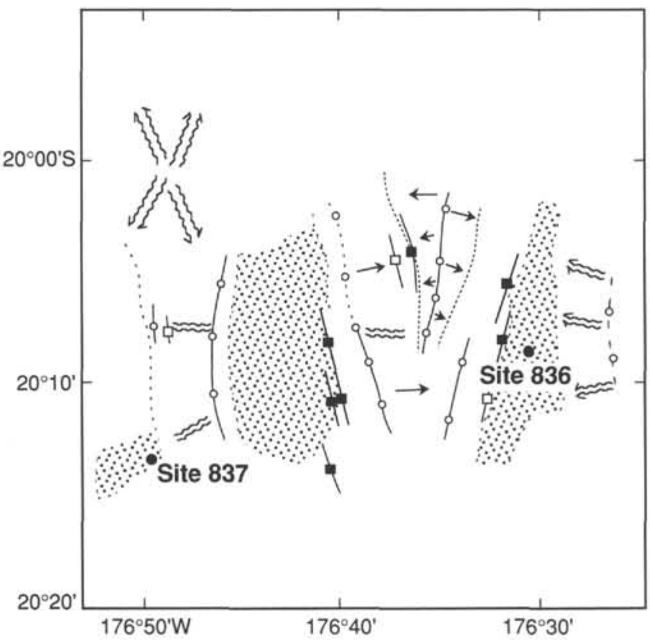

Figure 5. Morphotectonic sketch of the seafloor around Sites 836 and 837. Stippled areas denote planar-laminated, flat-lying sediments. Paired wavy lines are sites of undulatory, laminated sediments and indicate regional dip. Antiformal (open circles), synformal (open squares), and fault (filled squares) ornaments on linear trends denote regional morphology.

is erupted, and the western Lau Basin where rocks intermediate in composition between arc and "MORB-like" have been recovered (Hawkins, 1976; Hawkins and Melchior, 1985). Thus, it seemed likely that Site 836 igneous rocks would show some affinity to arc samples. Parson et al. (1990) noted the extremely asymmetric position of the ELSC relative to the Tonga and Lau ridges and discussed the possibility that it was a relatively young feature having formed as the result of a ridge jump toward Tonga Ridge. They observed that the magnetic anomaly pattern was difficult to interpret but it did not appear to support this model. They assumed, as have all others who have attempted to interpret Lau Basin magnetic data, that all of the magnetic fabric can be related to magnetic "stripes" formed by seafloor spreading. As discussed in the "Introduction and Principal Results" chapter, the history of the Lau Basin may have been more complex than envisioned by this simple model.

Seismic Stratigraphy

Seismic reflection profiles, collected by *Charles Darwin* (Parson et al., 1989) and *Thomas Washington* (Hawkins, 1989) were used to select the original Site 836 location (Fig. 6A). The approach track and site survey line recorded by the *JOIDES Resolution* are located in Figures 6B and 6C. These data consistently show a strongly reflecting, undulating seafloor in Basin 836 (Fig. 7A). The seismic profiles indicate some sub-bottom reflections in the uppermost 0.1 sec two-way traveltime (TWT), which are almost completely masked by acoustic reverberations from the gun signal. This acoustic character persists over both bathymetric lows and highs. The 3.5-kHz, high-resolution seismic profiler provided the best information on shallow sediment thickness in the basin, showing sediments up to 70 m thick on the flanks of the basin. However, the 3.5-kHz seismic data show little or no penetration in the central, deepest part of Basin 836, where the strongly reflecting acoustic texture is interpreted as a bare rock surface from which the sediments have been stripped.

Scientific Objectives: Sites 836, 837, 838, and 839

The primary objectives of the sites in the central Lau Basin were to sample the sedimentary column so as to determine the lithostratigraphy, biostratigraphy, and magnetic stratigraphy, the physical properties of the sedimentary column and underlying basement rocks, and to sample igneous rocks for petrologic and geochemical study. Specific objectives for the sediment samples included (1) determining the age of the beginning of sediment deposition in the basins and, by inference, the age of basin formation; (2) analysis of variations in the volcaniclastic, carbonate, and clay constituents of the sediments and the implications for provenance and depositional processes; and (3) regional correlations in the sedimentary record at the drill sites. Objectives of the igneous rock studies include determination of the nature of the mantle source; recognizing and modeling effects of petrogenetic processes such as fractionation, magma mixing, or crustal assimilation; and using these data to make inferences about the relationship between tectonic processes and magmatism.

These investigations had several goals, but two primary objectives were to test tectonic models that postulated jumps and/or migration of backarc spreading ridge (as invoked by Parson et al., 1990), and to evaluate the hypothesis of Hawkins and Melchior (1985) that there was a compositional zonation from more arc-like basalts on the margins of the basin to more MORB-like basalts at the active spreading centers. A major objective for all of the sites was to understand the tectonic framework of the Lau Basin and to use this to understand how backarc basins develop. Drilling at Sites 836 and 837 did not satisfy all of the original objectives and, consequently, alternate Sites 838 and 839 were drilled. Collectively, the objectives for the central Lau Basin were attained.

OPERATIONS

Introduction

After completion of Site 835, the *JOIDES Resolution* began a 211-nmi-long transit at 2118 hr UTC on 3 January 1991 to Site

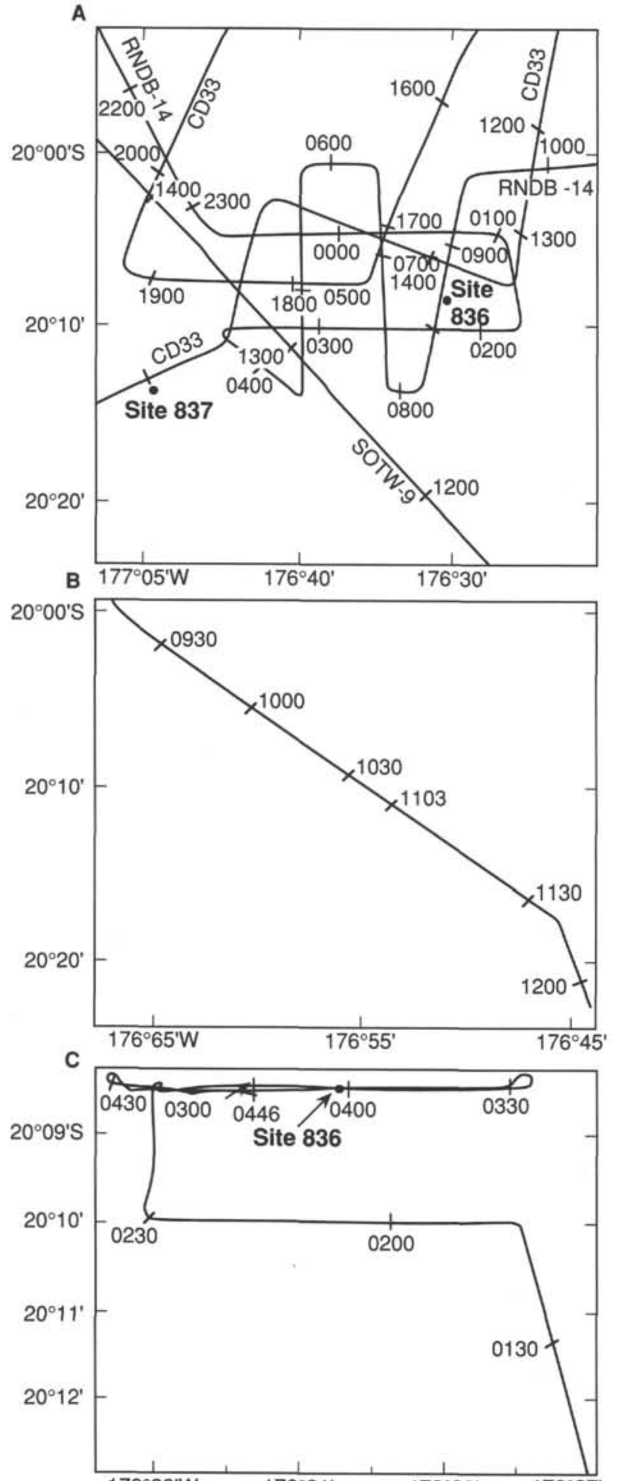

Figure 6. Track charts showing the locations of the seismic lines used to select Site 836, including (**A**) the *Charles Darwin* (CD33, Parson et al., 1989) and the *Thomas Washington* (SOTW-9, Hawkins, 1976; RNDB-14, Hawkins, 1989); (**B**) the *JOIDES Resolution* for the initial site survey of Site 836 on 4 January 1991; and (**C**) the approach site survey lines of the *JOIDES Resolution* on 6 January 1991.

840 (LG-3) for acquisition of seismic data to assist in the assessment of possible hydrocarbon risks at the site. A 90-nmi-long survey began at 2200 hr UTC on 4 January, and the results from it are presented in the "Operations" section of the Site 840 chapter. Site 836 was planned to be cored during the time required to evaluate the prospective Site 840 seismic data. During the transit to the prospective Site 840, the *JOIDES Resolution* conducted a short (19 nmi) seismic survey across the Site 836 area to aid in the selection of a specific drilling site. This survey is further described below together with the site approach. After the survey of the prospective Site 840 was completed at 1300 hr UTC on 5 January, the ship steamed 113 nmi back to the northwest, arriving at the Site 836 area at 1305 hr UTC on 6 January.

Site Approach and Site Survey

This site lies in a north-northeast-trending, narrow, lens-shaped basin of about 16 km in length and 3 km in width at the 2400-m isobath. Scarps defining the basin rise locally to <1800 m depth. The deepest part of the basin lies in its center at 20°10′S, 176°30′W, at a depth greater than 2600 m. The basin is located in the central Lau Basin on relatively young crust, about 55 km from the presently active backarc spreading axis of the ELSC. One suggestion is that this crust may represent the oldest seafloor generated at the ELSC following an eastward ridge jump that occurred about 1 Ma. Site 836 had previously been surveyed with a combination of single-channel seismic data from *Charles Darwin* (CD33) and *Thomas Washington* RNDB-14 cruises, as well as with the GLORIA and SeaBeam systems (Fig. 6A). With <100 m of sediment overlying basement, the site was considered to be the youngest backarc site that could be selected for drilling without requiring a bare-rock guide base.

Initial Geophysical Survey During Transit to Prospective Site 840

The initial survey over Site 836 occurred during the transit to prospective Site 840 and covered 19 nmi. Two 80-in.^{3} water guns, a 60-element single-channel Teledyne hydrophone, and a proton precession magnetometer were deployed. The tracks of the *JOIDES Resolution* for this pre-site survey are given in Figure 6B.

Geophysical Survey During Site Approach

After slowing to deploy two 80-in.^{3} water guns, a 60-element single-channel Teledyne hydrophone, and a proton precession magnetometer (at 20°13°697′S, 176°26.747′W, 11 nmi from Site 836), the ship conducted a 32-nmi-long survey that began at 0105 hr UTC on 6 January (Fig. 6C). The survey comprised two east-west traverses of the basin, offset from one another by 1.5 nmi. At 0231 hr UTC the ship made a Williamson turn, took a reciprocal course, and dropped a beacon to mark the site at 0358 hr UTC at 20°08.506′S, 176°30.041′W (Fig. 6C). Underway geophysical gear was recovered by 0422 hr UTC; the ship came on station at Site 836 at 0454 hr UTC on 6 January 1991 to begin coring operations.

Drilling and Logging Summary

Our original plan was to drill three adjacent holes at Site 836, with the principal objective of reaching 200 m of basement penetration. Hole 836A was planned as an advanced hydraulic piston corer (APC) hole to obtain a complete and relatively undisturbed sediment section. As the sediments were expected to be thin (<100 m thick from the 5–6 January 1991 *JOIDES Resolution* survey), use of the extended core barrel (XCB) corer was not expected. Hole 836B was to be a rotary core barrel (RCB) hole that washed through most of the sediments, beginning coring just above the sediment-basement interface and continuing to 50-m basement penetration or bit destruction. The sedimentary section and sediment-basement interface in Hole 836B would then be logged.

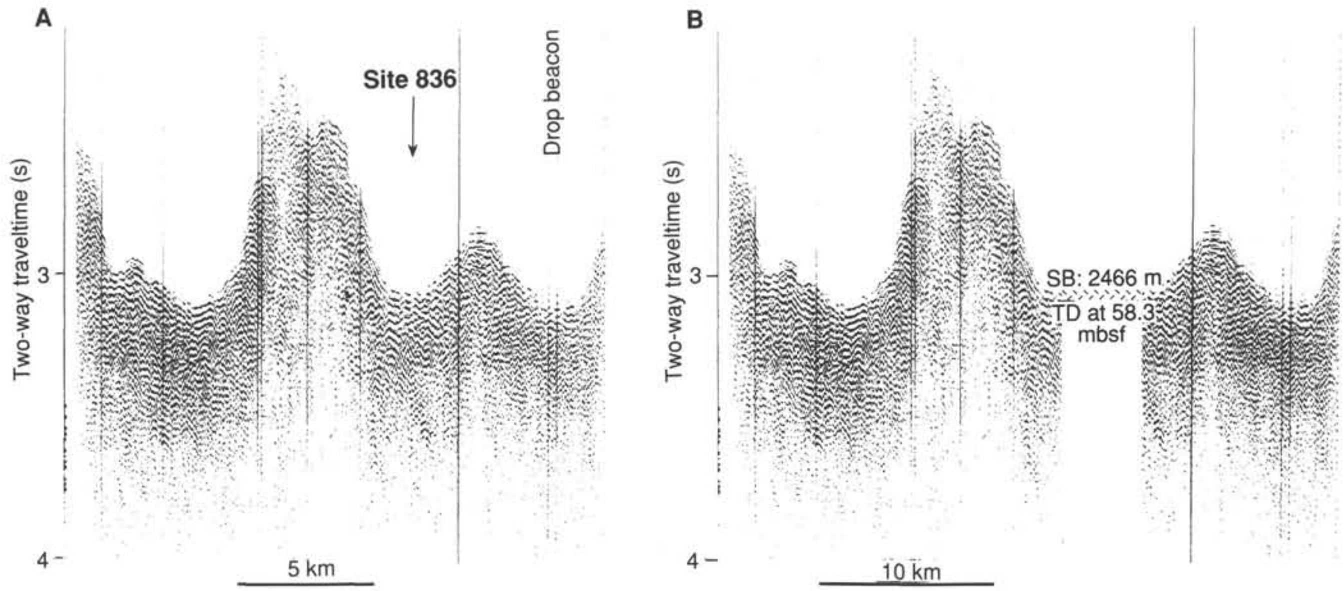

Figure 7. **A.** Single-channel seismic reflection profile across Basin 836 recorded by the *JOIDES Resolution*. Vertical exaggeration is approximately 15:1. **B.** Interpretation of seismostratigraphy at Site 836. SB = seismic bottom reflector and TD = total depth.

Hole 836C was planned to be a deep-penetration reentry hole, using either a reentry cone on a guide-base or a drill-in casing topped with a reentry cone, with casing in both instances installed through the sediments and sediment-basement interface. The total penetration into basement was hoped to be 200 m, giving a total hole depth of about 350 m. The section below the casing would then be logged, followed by a drill-string packer experiment in the interval made through the basement section to assess permeability in this young backarc crust. Coring results from the site are presented in Table 1.

Hole 836A

Hole 836A was located at 20°08.494'S, 176°30.008'W. It was spudded in at 1112 hr UTC, 6 January 1991, with a mud-line core establishing the seafloor depth as 2466.3 m below the driller's datum. Four cores were taken with the APC to a depth of 21.2 mbsf, with refusal reached during the fourth core. Basalt was encountered at 20.2 mbsf in the core catcher of Core 135-836A-3H, and Core 135-836A-4H consisted of basaltic breccia. Recovery using the APC was excellent (97.7%). A nonmagnetic drill

Table 1. Coring summary, Site 836.

Core no.	Date (Jan. 1991)	Time (local)	Depth (mbsf)	Cored (m)	Recovered (m)	Recovery (%)	Age
135-836A-							
1H	6	1130	0.0–1.2	1.2	1.24	103.0	upper Pleistocene
2H	6	1200	1.2–10.7	9.5	9.71	102.0	middle Pleistocene
3H	6	1250	10.7–20.2	9.5	9.73	102.0	middle Pleistocene
4H	6	1330	20.2–21.2	1.0	0.13	13.0	middle Pleistocene
5X	6	1550	21.2–22.7	1.5	0.11	7.3	
6X	6	1745	22.7–25.7	3.0	0.10	3.3	middle Pleistocene
7X	6	2025	25.7–31.2	5.5	0.63	11.4	middle-lower Pleistocene
8X	6	2325	31.2–35.2	4.0	1.20	30.0	
9X	7	0220	35.2–38.2	3.0	1.61	53.6	
Coring totals				38.2	24.46	64.0	
135-836B-							
1R	7	1345	0.0–4.5	4.5	4.34	96.4	upper Pleistocene
2R	7	1515	18.0–23.0	5.0	0.14	2.8	middle Pleistocene
3R	7	1735	23.0–28.5	5.5	2.22	40.3	
4R	7	2050	28.5–34.0	5.5	0.69	12.5	middle-lower Pleistocene
5R	7	2340	34.0–39.0	5.0	4.17	83.4	
6R	8	0135	39.0–43.7	4.7	2.11	44.9	
7R	8	0325	43.7–53.3	9.6	1.70	17.7	middle-lower Pleistocene
8R	8	0500	53.3–58.3	5.0	0.62	12.4	
9M	8	0920	58.3	0	1.01	N/A	
Coring totals				44.8	17.00	38.0	

Notes: Core 135-836B-9M represents no advance, and recovered material fallen into the hole from above. N/A = not applicable.

collar was used, and the multishot tool provided orientation for Cores 135-836A-3H and -4H. The encounter with basaltic fragments required a change to the XCB. Five more cores of basalt with intercalated sediment were taken with the hard formation XCB, with fair recovery (21.5%) to a depth of 38.2 mbsf. Difficult drilling conditions required taking short cores; coring was ended because of the low rate of penetration (2 m/hr), wear on the hard-formation bit, and deteriorating hole conditions. As a result of poor hole conditions, no temperature measurements were taken with the downhole water sampler temperature probe (WSTP).

Hole 836B

The *JOIDES Resolution* then moved 20 m south to 20°08.505'S, 176°30.011'W. A 9⅞-in. RCB bottom-hole assembly (BHA) was run on the end of the drill string to the seafloor, and Hole 836B was spudded at 1210 hr UTC, 7 January 1991. A wash core (135-836B-1R) determined the water depth to be 2468.5 m below the driller's datum. The hole was washed from 4.5 to 18.0 mbsf, and Cores 135-836B-2R to -8R were taken from 18.0 to 58.4 mbsf. Basalt was first encountered at 18.1 mbsf, with a total of 44.8 m of intercalated basalt and sediment cored and 17.0 m recovered (recovery of 38.0%). Unstable, sloughing basalt and basaltic breccia, encountered at 50–59 mbsf, caused the hole to be filled in with debris repeatedly, despite multiple reaming with the drill string and pumping of mud. Coring ended therefore at Core 135-836B-9M, after no advance in 4.5 hr. Although the objective of reaching 200 m of basement penetration was not met, it was not considered prudent to either set the re-entry cone with casing or the drill-in casing because of the unstable hole conditions at such a shallow level into basement. No logging was attempted because of the poor hole conditions.

LITHOSTRATIGRAPHY

Introduction

We recovered 21 m of clayey nannofossil ooze with interbedded volcanic sands and silts, rare pyroclastic ashes, and thick, mafic hyaloclastites at Site 836. Volcaniclastic beds are typically graded, passing progressively into sediments with greater nannofossil content upsection. Between end-member sediments (nannofossil ooze and hyaloclastite), a variety of lithologies occurs, including clayey nannofossil ooze with foraminifers, volcanic sand and silt, vitric clay with nannofossils and foraminifers, clayey nannofossil mixed sediment with glass, nannofossil vitric mixed sediment with clay, vitric nannofossil mixed sediment with clay, nannofossil chalk with foraminifers and clay, vitric claystone, and almost pure hyaloclastite (Fig. 1). Vesicular basaltic breccia was reached at 20.20 mbsf, corresponding to the cessation of basement volcanism at Site 836 at about 0.64 Ma (middle Pleistocene).

Lithologic Units

Unit I

Intervals: Cores 135-836A-1H to -4H and Core 135-836A-6X; Cores 135-836B-1R to -3R
Depth: 0 mbsf (as defined in Hole 836A)
Age: middle Pleistocene to Holocene

One lithostratigraphic unit has been defined at Site 836, comprising a sequence of generally thick-bedded, clayey nannofossil oozes with thin and medium interbeds of volcaniclastic sediment. Subunit IA contains rare, normally graded, gray (10YR 6/1) ash layers, 2–3 cm thick (Fig. 8), separated by hemipelagic deposits, 50–100 cm thick. Hemipelagic deposits comprise brown to dark brown (10YR 4/3), clayey nannofossil oozes containing up to 25 vol% of dispersed glass shards. Mottling caused by burrowing is common in the otherwise homogenous ooze. Fragments of pumice

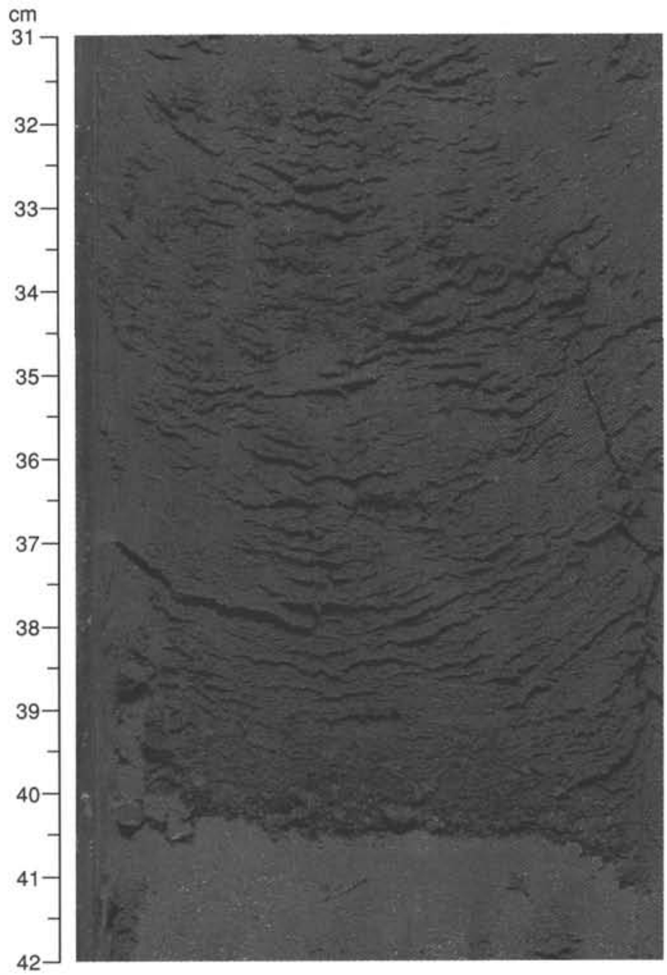

Figure 8. Thin layer of vitric sand grading upward into vitric siltstone and clayey nannofossil ooze. Note eroded basal surface at 40 cm and the presence of intraclasts of the underlying depositional unit (Section 135-836A-2H-6, 31–42 cm).

and mafic volcanic rocks occur randomly scattered throughout the sequence. A thin bed of breccia in Section 135-836A-2H-3, 79–95 cm (4.99–5.15 mbsf), consists of angular pumice lapilli with clasts up to 4 cm in diameter enclosed in a matrix of brown to dark brown (10YR 4/3) clayey nannofossil ooze.

Farther downhole, in Subunit IB, the number of volcaniclastic layers increases markedly. Very pale brown to very dark gray (10YR 7/3 to 10YR 3/1) units of graded volcanic sands and silts are up to 17 cm thick (e.g. in Section 135-836A-2H-4, 31–48 cm). They are coarse grained in their lower parts and some contain foraminifers; they pass upward into massive or parallel-laminated sand and eventually into brown to dark brown (10YR 4/3) clayey nannofossil ooze. An interval of pure, grayish brown to dark brown (10YR 5/2 to 10YR 3/3), clayey nannofossil ooze (Section 135-836A-2H-6, 40 cm, to -3H-1, 133 cm) with scattered fragments of pumice lapilli is followed by a succession of multiple, dark brown to black (10YR 3/3 to 10YR 2/1) volcanic sands and black (10YR 2/1) mafic hyaloclastites. These occur as distinct, normally graded layers (each 2–26 cm thick) with scoured bases and very rare planar lamination. These layers may comprise up to 50 vol% of the sequence. Individual layers grade upwards into nannofossil-dominated, generally slightly mottled clayey oozes.

Black (10YR 2/1) hyaloclastite layers, up to 100 cm thick, occur in Section 135-836A-3H-3, 8–99 cm, and in Sections 135-836A-3H-4, 50 cm, through -3H-5, 1 cm. These deposits are generally moderately sorted with angular clasts up to 3 cm in diameter. The thick and coarse hyaloclastites are overall inversely graded, but internally, normal grading may occur in thin, centimeter-thick layers.

The lowermost part of Subunit IB (Sections 135-836A-3H-6, 135 cm, to -3H-7, 79 cm) is dominated by homogeneous, occasionally mottled, dark yellowish brown (10YR 4/4) nannofossil ooze with minor clay and dispersed glass shards. Within the oozes there are, however, a few normally graded volcanic sand layers with eroded bases (Fig. 9). Angular mafic volcanic fragments, up to 2 cm in diameter, occur in poorly sorted, disrupted layers, up to 5 cm thick (Section 135-836-3H-7; Fig. 10). Immediately above

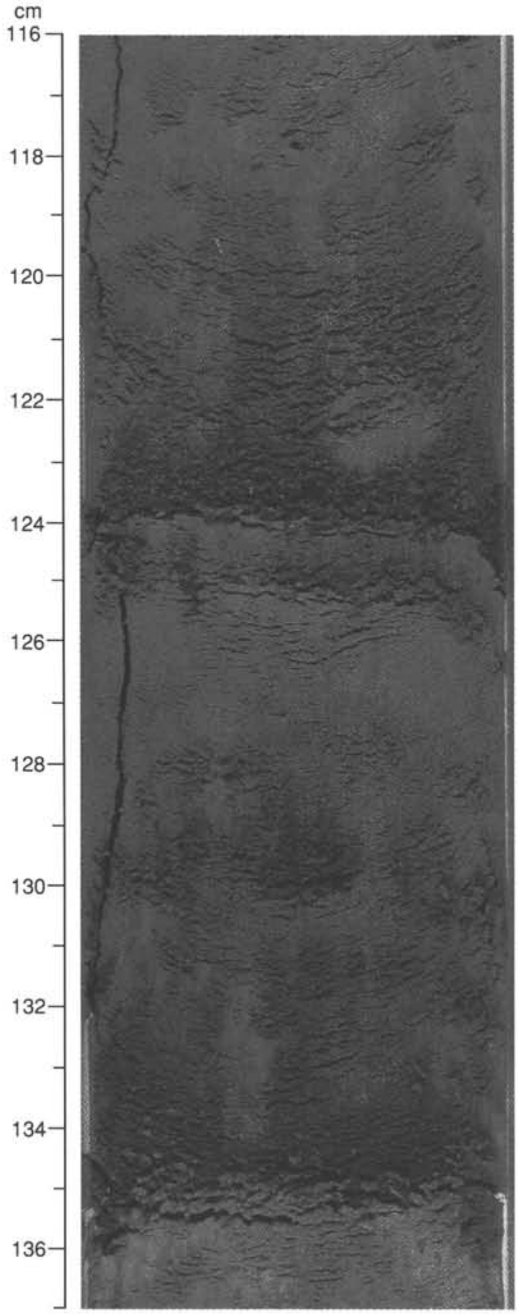

Figure 9. Two thin layers of vitric sand and silt, at 124 and 135 cm, grading upward into mottled nannofossil ooze (Section 135-836A-3H-6, 116–137 cm).

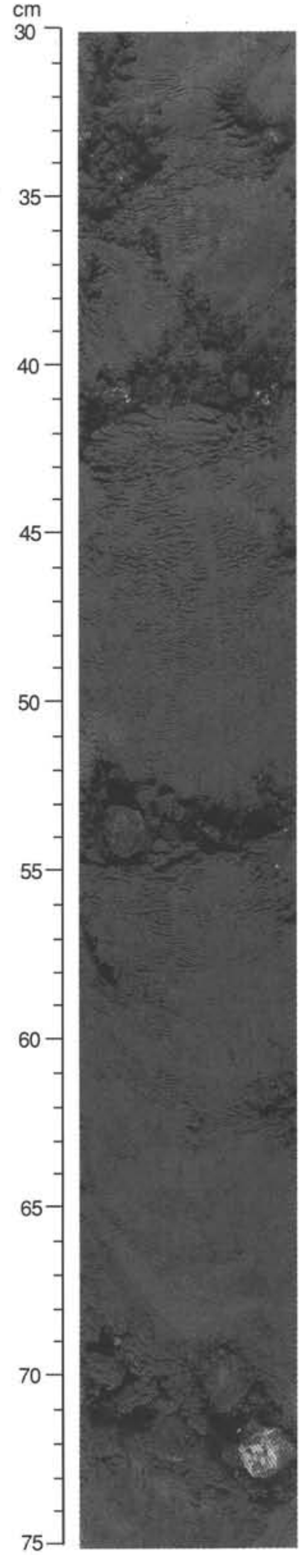

Figure 10. Disrupted, 2–3-cm-thick layers of angular mafic fragments, up to 16 mm in diameter, embedded in nannofossil ooze with clay, glass, and foraminifers (Section 135-836A-3H-7, 30–75 cm).

the igneous basement a thin unit of black (10YR 2/1) basaltic breccia was recovered (Section 135-836A-4H, 0–14 cm).

In Hole 836B (Section 135-836-3R-1, 0–59 cm), a sequence of light yellowish green to light greenish gray (10Y 5/2 to 2.5Y 6/4) bioturbated vitric claystone with graded layers and planar and ripple cross-lamination was recovered. This presumably represents an intralava sediment.

Volcaniclastic Sediments

Forty-one sediment layers containing more than about 50 vol% and up to almost 100 vol% volcanic material occur in Hole 836A (Table 2). The volcanic-derived components are predominantly ash-sized. Lapilli-sized clasts are more abundant in Subunit IB.

We examined 26 samples in smear slides. Refractive indices of optically clear, isotropic glass shards were determined in six samples (Table 3) to evaluate their SiO_2 concentrations by the method described in detail in the site reports for Sites 834 and 835 (this volume). Primary tephras were excluded because of their small volumes.

In the core we distinguish three important types of volcaniclastic sediments: (1) three well-preserved primary fallout tephra layers (2–3 cm thick) in the uppermost 7 m of the core; (2) reworked, epiclastic deposits; and (3) hyaloclastites.

Primary Fallout Tephra Layers

Well-preserved primary fallout tephras are found in Sections 135-836A-2H, 1–77 cm (T1), 135-836A-2H-2, 139 cm (T2), and 135-836A-2H-4, 92 cm (T3). All tephra beds are bioturbated, resulting in destruction of most primary bedding features, as well as the mixing of bioclastic components such as foraminifers,

Table 2. List of discrete ash layers, ash turbidites, and hyaloclastites in Holes 836A and 836B.

Core, section, depth	Depth to top (mbsf)	Depth to base (mbsf)	Smear slide	Thickness (cm)	Type of unit	Glass (vol%)	Maximum grain size (µm)	Significant shard morphologies: Tubular	Bubble wall	Angular	Igneous minerals present (>1 vol%)
135-836A-											
1H-1, 68	0.68	0.69	X	1	P, H	60	500	X	X	X	plag, augite
1H-1, 85	0.84	0.86	X	2	P, H	47	400		X		plag, augite, opaques
2H-1, 77	1.96	1.98	X	2	P, G	77	120		X	X	plag
2H-2, 84	3.53	3.54	X	1	E, G	30	ND				
2H-2, 139	4.07	4.09	X	2	P, G	86	100				
2H-3	4.99	5.15		16	E, H	ND	ND				
2H-4, 46	6.01	6.18	X	17	E, G	85	ND				
2H-4, 92	6.61	6.64	X	3	P, G	70	500				
2H-4, 127	6.96	6.98		2	E, G	ND	ND				
2H-5, 36	7.55	7.59	X	4	E, G	50	600				
2H-5, 93	8.12	8.15	X	3	E, G	40	300				
2H-6, 39	9.05	9.10	X	5	E, H	71	270	X	X	X	augite, opaques, plag
3H-2, 5	12.20	12.28	X	8	E, H	45	ND				
3H-2	12.28	12.43		15	E, G	ND	ND				
3H-2, 26	12.43	12.48	X	5	E, G	98	700	X	X	X	
3H-2, 34	12.48	12.70	X		E, H	45	ND				
3H-2	12.70	12.75		5	E, G	ND	ND				
3H-2	12.75	12.80		5	E, G	ND	ND				
3H-2	12.80	12.91		11	E, G	ND	ND				
3H-2, 102	13.00	13.03	X	3	E, G	ND	900	X	X	X	
3H-2, 106	13.03	13.07	X	4	E, G	ND	600	X		X	augite
3H-2	13.09	13.13		4	E, G	ND	ND				
3H-2	13.13	13.22		9	E, G	ND	ND				
3H-2	13.22	13.30		8	E, G	ND	ND				
3H-3, 6	13.70	13.78	X	8	E, H	55	260		X	X	
3H-3	13.78	14.69		91	E, G	ND	ND				
3H-3, 127	14.95	14.98	X	3	E, G	98	700	X	X	X	plag
3H-3	15.12	15.15		3	E, G	ND	ND				
3H-4, 27	15.20	15.70	X	50	E, H	95	ND				
3H-4	15.70	16.71		101	E, H	ND	ND				
3H-5, 32	16.97	17.05	X	8	E, G	85	800		X	X	plag, opaques, augite
3H-5, 50	17.05	17.26	X	21	E, G	50	400	X	X	X	plag, opaques, augite
3H-5	17.70	17.81		11	E, G	ND	ND				
3H-5	17.81	17.92		11	E, G	ND	ND				
3H-5	17.92	17.94		2	E, G	ND	ND				
3H-5, 127	17.94	17.98	X	4	E, G	30	480		X	X	plag, augite
3H-6, 28	18.48	18.49	X	1	E, G	80	ND				
3H-6	18.76	18.78		2	E, G	ND	ND				
3H-6	19.04	19.08		4	E, G	ND	ND				
3H-6, 124	19.38	19.44	X	6	E, G	100	600	X	X	X	opaques, augite
3H-6	19.44	19.49		5	E, G	ND	ND				
3H-6, 134	19.49	19.55	X	6	E, G	20	350	X	X	X	
4X-1	20.20	20.34		14	E, H	ND	ND				
135-836B-											
1R-2, 21	1.68	1.73	X	5	E, H	ND	250	X		X	plag (minor)
1R-2	1.90	1.9		7	E, H	ND	ND				
1R-2	2.87	2.8		2	E, H	ND	ND				
1R-3, 24	3.19	3.28	X	9	E, G	ND	ND				
1R-3	3.44	3.53		9	E, H	ND	ND				

Notes: Glass percentages indicate maximum modal content as estimated from smear slides. Glass content may, however, be highly variable, especially in turbidite sequences. Key to columns: Type: P = pyroclastic, E = epiclastic, H = homogeneous, and G = graded. Dominant morphologies: tub. = pumiceous shards with tubular vesicles, bubble wall = bubble-wall shards, ang. = angular shards. Igneous minerals present: plag = plagioclase.

Table 3. Refractive indices (n) and SiO_2 concentrations (estimated from Church and Johnson [1980] and Schmincke [1981]) of optically clear vitric shards (5ϕ grain-size fraction) from Site 836.

Core, section, interval (cm)	Depth (mbsf)	Comments	n	SiO_2 (wt%)
135-836A-				
1H-1, 84	0.84	Brown/green	1.565	56.1
1H-1, 84	0.84	Clear	1.516	68.3
2H-4, 45	6.15	Clear	1.531	64.2
2H-6, 38	9.08	Brown/green	1.566	55.9
2H-6, 38	9.08	Clear	1.533	63.7
3H-2, 25	12.45	Brown/green	1.569	55.2
3H-2, 25	12.45	Clear	1.538	62.4
3H-4, 60	15.80	Brown/green	1.570	55.0
3H-4, 60	15.80	Clear	1.541	61.7
3H-6, 123	19.43	Brown/green	1.569	55.2
3H-6, 123	19.43	Clear	1.522	66.6

radiolarians, and calcareous nannofossils. Some of the thin, more intensely bioturbated ash bands occurring in the upper part of the core may also represent primary fallout deposits.

Tephras (T1) and (T2) both consist of well-sorted colorless vitric shards with maximum grain sizes rarely exceeding 100 µm and mean grain sizes of around 50 µm. Both have few fibrous or pumiceous shards with tubular vesicles, but abundant platy angular, bubble-wall and bubble-junction shards. The latter two types are especially abundant in tephra (T1). Minerals of igneous origin are extremely rare. Both tephra units are interpreted as very distal (>1000 km) fallout ashes from Plinian-type eruptions of evolved, dacitic to rhyolitic magmas.

Tephra (T3) is largely composed of well-sorted, brown vitric shards <500 µm in diameter, comprising vesicular and fibrous types with tubular vesicles, in addition to angular platy shards. The associated mineral assemblage includes plagioclase and clinopyroxene. Tephra (T3) is interpreted as a medial fallout tephra of andesitic or basaltic andesitic composition.

Reworked Epiclastic Deposits

Thin turbidites with bases rich in dacitic to rhyodacitic vitric shards contain the largest proportion of volcaniclastic material in Sites 834 and 835, but occur very rarely in Hole 836A. These sequences are rare, poorly defined, and restricted to the upper part of Hole 836A (e.g., base at Cores 135-836-2H, 4–46 cm).

Hyaloclastites

Hyaloclastites make up the biggest part of the volcaniclastic input into the sediments of Hole 836A. In Site 836 they differ significantly from those in Sites 834 and 835 by (1) chemical composition, (2) origin of the shards, (3) mode of emplacement, (4) grain size, (5) inferred distance to the source, and (6) relative abundance in the sediment.

Shards found throughout Hole 836A are predominantly brown to slightly green vitric basaltic andesites with a rather small compositional range of 55–56 wt% SiO_2, judging from their refractive indices of 1.570 to 1.565 (Table 3 and Fig. 11). A bulk sample from the coarse-grained, thick hyaloclastite in Section 135-836A-3H-4 was taken for XRF analyses (see "Igneous Petrology" section, this chapter). The XRF analyses of cleaned and handpicked samples yielded 56.8–57.0 wt% SiO_2. These values are 1.8–2 wt% above estimates from refractive indices from the same depositional interval.

Vitric shards of basaltic andesitic to andesitic composition typically make up >90 vol% of the sediment. They often occur in almost pure, dark gray to black vitric beds, up to 100 cm thick,

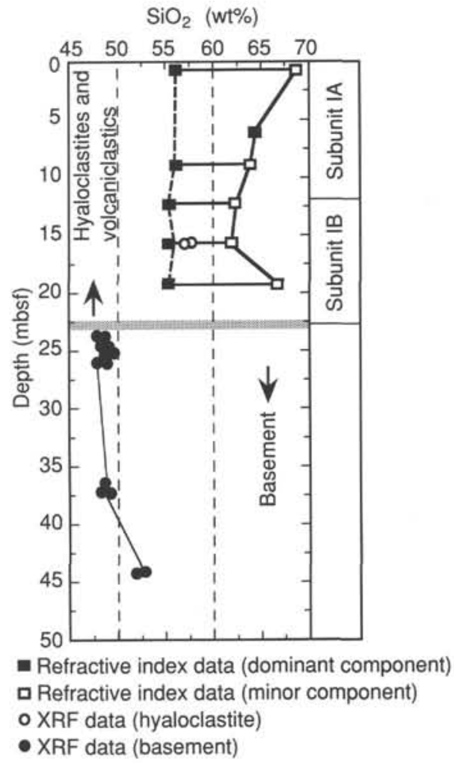

Figure 11. Downhole plot of SiO2 concentrations in vitric shards from epiclastic ashes and hyaloclastites, Holes 836A and 836B, as estimated from refractive indices of optically clear volcanic glass and determined by XRF analyses. The occurrence of two distinct populations of shards in individual samples is indicated by connecting lines.

with maximum grain sizes of 200 to 1000 µm (Fig. 12). One pure volcaniclastic bed, 100 cm thick (in Section 135-836A-3H-4), is characterized by an overall inverse grain-size grading and maximum diameters of black vitric clasts of about 3 cm. The predominantly vitric nature of these clasts and the scarcity of mafic minerals in the hyaloclastites is confirmed by a very constant and low magnetic susceptibility throughout the sedimentary succession that remains unchanged even in intervals with thick coarse-grained hyaloclastites (see "Paleomagnetics" section, this chapter). The presence of Fe-Ti oxides, which are otherwise very common in the groundmass of basaltic andesitic and andesitic volcanics, would drastically increase the magnetic susceptibility.

The average thickness of layers increases downhole (Fig. 13), with 5–7 individual layers per meter of core in the depth interval 12 to 15 mbsf. This corresponds to a very high deposition rate of up to 13 layers per 50,000 yr, compared with 1–3 layers per 50,000 yr in Subunit IA. Shards in these deposits are often blocky and angular. Vesicularity is highly variable and ranges approximately from 10 to 50 vol% (see "Igneous Petrology" section, this chapter). Vesicles are normally 5–700 µm in diameter and are mostly slightly elongate to very elongate in shape. They often show a subparallel orientation, as do some elongate phenocrysts (e.g. hypersthene). Compound vesicles, indicative of bubble coalescence, are very common.

Millimeter-sized angular shards with very straight or only slightly curved edges may be vesicular or devoid of vesicles (Fig. 14). Igneous minerals present include plagioclase (as individual grains or microlites within the vitric shards), orthopyroxene, and, less commonly, green, augitic clinopyroxene.

We interpret the basaltic andesitic shards in Hole 836B as predominantly derived from hyaloclastites, originating from the

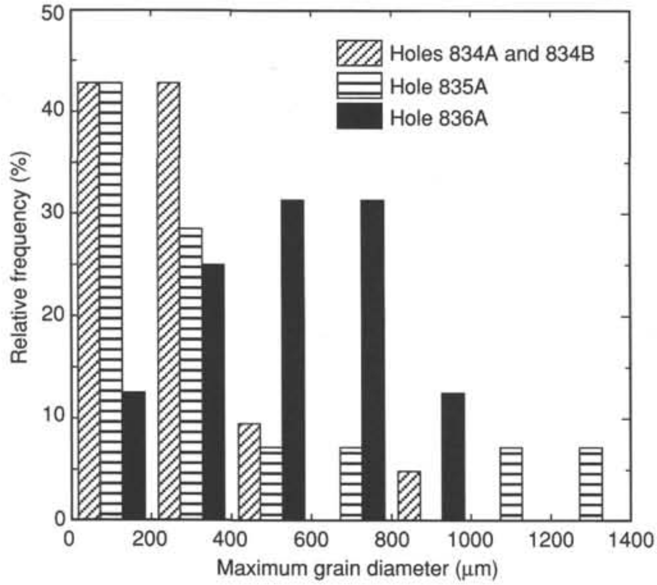

Figure 12. Histogram illustrating the frequency of maximum grain sizes in volcaniclastic/hyaloclastic deposits in Holes 834A, 834B, 835A, and 836A. Note that hyaloclastites in Hole 836 are distinctly coarser grained than volcaniclastics at previous sites.

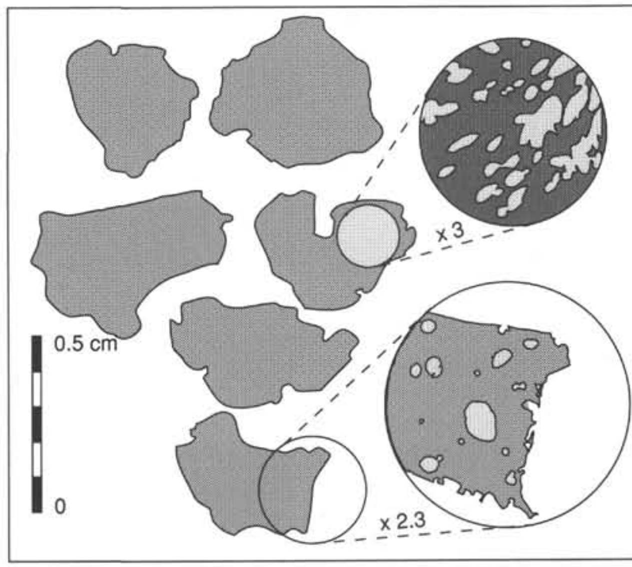

Figure 14. Shapes and vesicular texture of typical basaltic andesitic to andesitic vitric clasts from the hyaloclastites.

spalling of glassy pillow rinds and/or chilled margins of sheet-flow lavas, as determined from the predominantly blocky shapes and often low vesicularity. The high vesicularity in many shards may simply reflect the enhanced magmatic volatile content implied by the overall high vesicularity of basement rocks recovered during Leg 135 (see "Igneous Petrology" section, this chapter). The top parts of andesitic sheet-lava flows (which are one likely

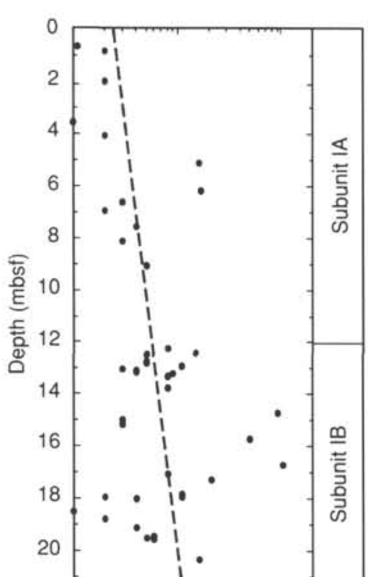

Figure 13. Downhole plot illustrating the thicknesses of individual layers enriched in volcaniclastic material, mainly hyaloclastite. The dashed line indicates the calculated trend for the overall decreasing thickness of layers uphole. Note the abundance of individual layers in the interval from 12 to 14 mbsf.

source of hyaloclastite shards) are often highly brecciated and highly vesicular in the Troodos ophiolite Extrusive Series (Schmincke and Bednarz, in press). Good sorting and abundant graded bedding indicate redeposition, probably on a local scale. Similar hyaloclastites are found accumulated in small hollows on the flanks of pillow mounds at the top of the Troodos ophiolite volcanic sequence (Bednarz and Schmincke, in press), mainly <1 km away from their sources.

An origin of the hyaloclastites from a rather proximal source is consistent with the large maximum and average grain-sizes (Figs. 12 and 14), the angular to subangular shapes of clasts, high sediment accumulation rates (see "Sediment Accumulation Rates" section, this chapter), and the high relative abundance of hyaloclastites. The decreasing thickness and abundance of the hyaloclastite beds upsection (Fig. 13) may be related to the greater distance away from the active volcanic zone, perhaps because of continued seafloor spreading and/or cessation of the volcanic activity in one segment of the volcanic center.

The deposition of a 1-m-thick, inversely graded sequence of hyaloclastites at Section 135-836A-3H-4 with angular clasts up to 2 cm in diameter may be related to the effusion of a single sheet flow or a cogenetic series of pillow tubes that moved toward Hole 836B, thereby successively reducing the distance to the site and permitting the deposition of increasingly coarser grained hyaloclastite. Alternatively, steepening of slopes during an individual eruption by syn-volcanic faulting and/or buildup of a volcanic topography may have permitted the deposition of successively coarser grained material in a single hyaloclastite deposit.

Depositional History

The first period of relatively undisturbed hemipelagic sedimentation at Site 836, immediately following the end of effusive volcanic activity at ~0.64 Ma, probably lasted <50,000 yr. Mafic, angular fragments <2 cm in diameter, which occur in thin discontinuous layers within the nannofossil ooze, suggest sporadic input of volcaniclastics from nearby volcanoes. Volcanic input became much more intense about 0.6 Ma, when volcanism was still active in the vicinity of the site, resulting in the frequent deposition of coarse-grained hyaloclastite layers, which are as thick as 101 cm. Increasing distance from the source (a volcanically active area, perhaps the backarc spreading center or an isolated seamount) resulted in less voluminous input of finer grained hyaloclastites into the site area. At about 0.5 Ma, when half of the sedimentary section (about 10 m) had accumulated, the deposition of hyaloclastite layers decreased sharply.

From 0.5 Ma to the present, hemipelagic sedimentation of clayey nannofossil ooze dominated the sedimentary record. This change is clearly reflected by a sharp decrease of sedimentation rates (see "Sediment Accumulation Rates" section, this chapter). An epiclastic, silicic, volcaniclastic deposit at 6.18 mbsf is interpreted to be derived from a distal source (e.g., Lau Ridge, Tofua Arc, or Zephyr Shoal). This sequence was emplaced as a thin, well-defined turbidite and corresponds to an age of 0.24 Ma. Apart from this, evolved vitric shards are dispersed within the hemipelagic oozes and constitute as much as 25 vol% of the sediment. Three distal to medial, 2–3-cm-thick, fine-grained fallout tephras are preserved in the upper 7 m of the core. All are <0.26 m.y. old.

STRUCTURAL GEOLOGY

Sediments

The sediment section at Hole 836A is dominated by clayey nannofossil ooze, interrupted by thin graded epiclastic turbidite layers and two 1-m-thick hyaloclastite sequences. Few bedding planes were visible, and those that could be measured were gently dipping (Fig. 15). We observed no fractures and no evidence of tectonic disruption in the sedimentary section of the hole.

Igneous Rocks

No evidence for any faulting was found in igneous rock core recovered from Holes 836A or 836B. In the same manner as described in the "Structural Geology" sections of Sites 834 and 835, planar to irregular joints are common within the volcanic rocks. These joints can be distinguished from drilling-induced fractures by the presence of minor amounts of clay minerals, zeolites, and/or iron oxide/hydroxide coating the joint surfaces. Alteration halos of orange iron oxide up to 4 cm in width are locally present on either side of the joint planes. Such halos are also common at the ends of individual pieces of core, even those with polishing marks that indicate the core was spun during drilling. This suggests that joints are exploited during the disaggregation of the core and joint surfaces are obliterated during the drilling process.

The igneous rock cores were not demagnetized in the shipboard measurements, and the multishot orientation tool cannot be used in conjunction with XCB or RCB drilling. Thus, there were no means of orienting the joint planes measured from Holes 836A and 836B.

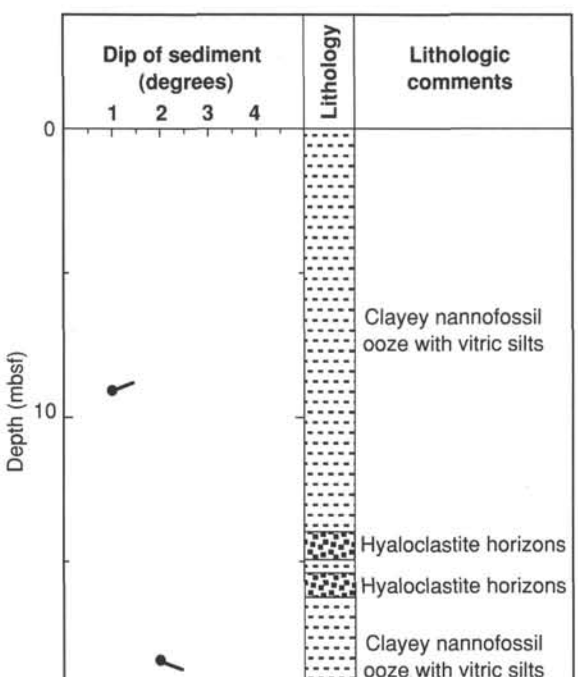

Figure 15. Dipmeter-type plot of sedimentary bedding orientation vs. depth, Hole 836A. The position of the filled circles corresponds to the magnitude of dip (on the scale indicated at the top of the diagram) and the position of the bar to the dip direction. $N = 3$.

BIOSTRATIGRAPHY

The biostratigraphic results for Sites 836A and 836B are summarized in Figures 16 and 17.

Calcareous Nannofossils

Pleistocene

Sample 135-836A-1H-CC contains a flora including *Pontosphaera indooceanica, Gephyrocapsa oceanica, G. caribbeanica,* and abundant *Emiliania huxleyi.* On this basis, this sample was assigned to Zone CN15.

Samples 135-836B-1R-CC and 135-836A-2H-CC yield a flora that includes very abundant small gephyrocapsids, *Helicosphaera inversa,* and *Gephyrocapsa oceanica* but lacks *Emiliania ovata.* Therefore, the samples are assigned to Subzone CN14b.

Samples 135-836A-3H-3, 7–8 cm, through -4H-CC and -6X-CC, Samples 135-836B-2R-CC and -4R-CC, and a sample from the top of Core 135-836A-7X contain floras that include *Emiliania ovata* and *Gephyrocapsa oceanica.* These samples were assigned to Subzone CN14a. Very rare *Helicosphaera sellii* found in Samples 135-836A-4H-CC and -6X-CC, and a single *Discoaster tamalis* in Sample 135-836A-6X-CC are reworked.

Planktonic Foraminifers

The sediments of Sites 836A and 836B contain abundant and well-preserved planktonic foraminifer assemblages. Only the middle and late Pleistocene are represented.

Late Pleistocene

Sample 135-836A-1H-CC contains a good, diverse fauna that includes *Bolliella calida calida, Globorotalia (Truncorotalia) truncatulinoides,* and *Pulleniatina finalis,* without either *Bolliella adamsi* or *Globorotalia (Globorotalia) tumida flexuosa,* indicating Zone N23 of Blow (1969) and the *Pulleniatina finalis* Subzone of Chaproniere (in press).

Middle Pleistocene

Faunas from the sandy foraminifer-nannofossil sediments in the lower part of the section are diverse and well preserved; in contrast, the assemblages from the ash deposits associated with the basalts forming the base of the section are of lower diversity and poorer preservation. Sample 135-836A-2H-CC contains *Bolliella praeadamsi, Globigerina (Globoturborotalita) rubescens tenellus, Gr. (Tr.) truncatulinoides, Gr. (Tr.) crassaformis hessi, Gr. (Gr.) cultrata neoflexuosa, Gr. (Gr.) tumida flexuosa, Gr. (Obandyella) bermudezi,* and *Pulleniatina obliquiloculata* (dextrally coiled); *B. calida calida* and *P. finalis* were not recorded. This fauna is typical of the *Bolliella praeadamsi* Subzone (Chaproniere, in press) of Zone N22 (Blow, 1969).

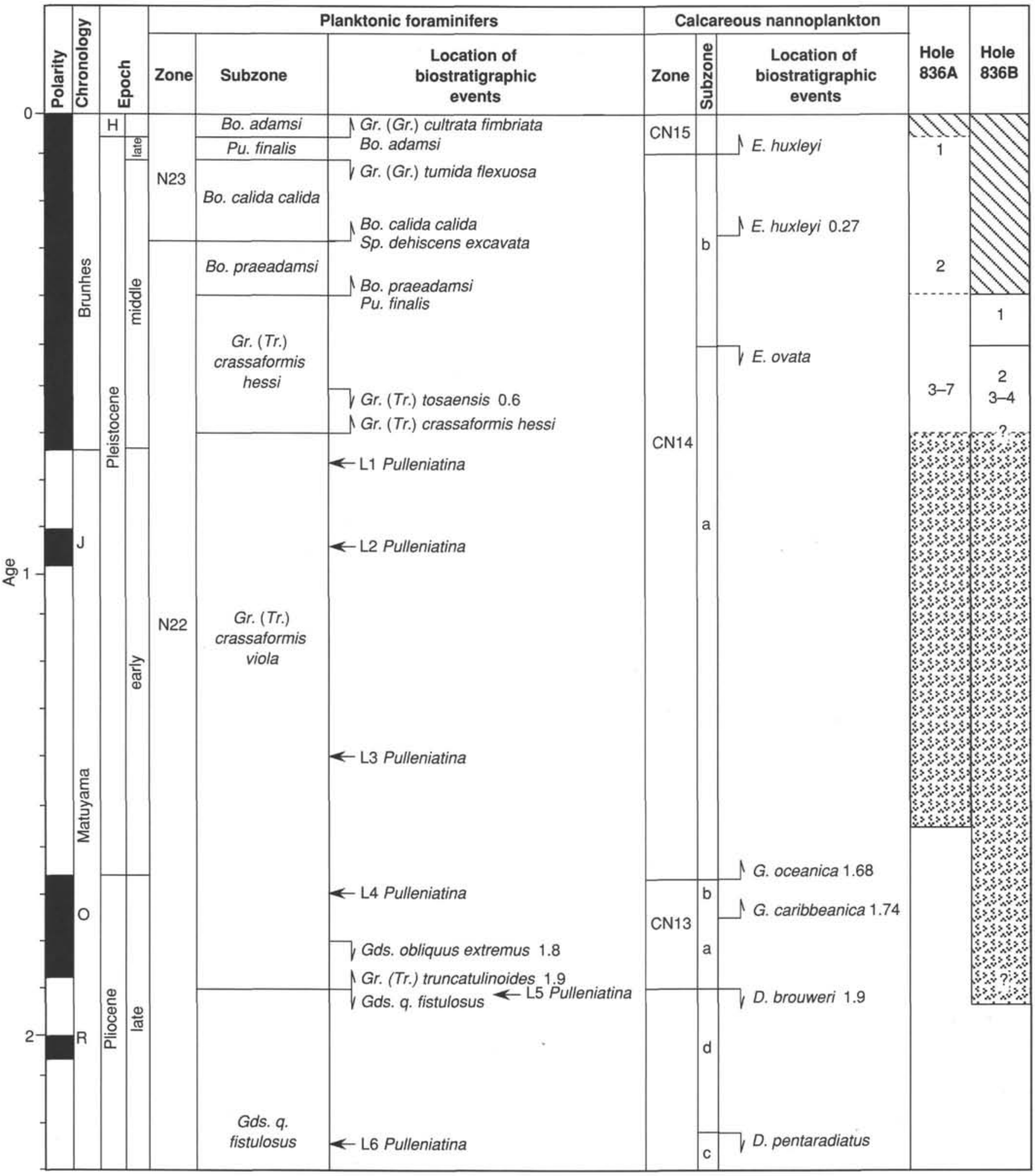

Figure 16. Biostratigraphic results, Site 836.

Samples 135-836A-3H-CC and -6X-CC contain similar assemblages to those noted above but differ in the absence of *B. praeadamsi*. The presence of dextrally coiled *Gr.* (*Tr.*) *crassula* in Sample 135-836A-3H-CC, and *Gr.* (*Tr.*) *crassaformis hessi* in both samples indicates the *Gr.* (*Tr.*) *crassaformis hessi* Subzone (Chaproniere, in press) of Zone N22.

SEDIMENT ACCUMULATION RATES

Both biostratigraphic and paleomagnetic data indicate that only the middle and late portion of the Pleistocene (all within the Brunhes Chron) is present in the sedimentary sequence at Site 836. The sediment sequence consists of calcareous oozes with

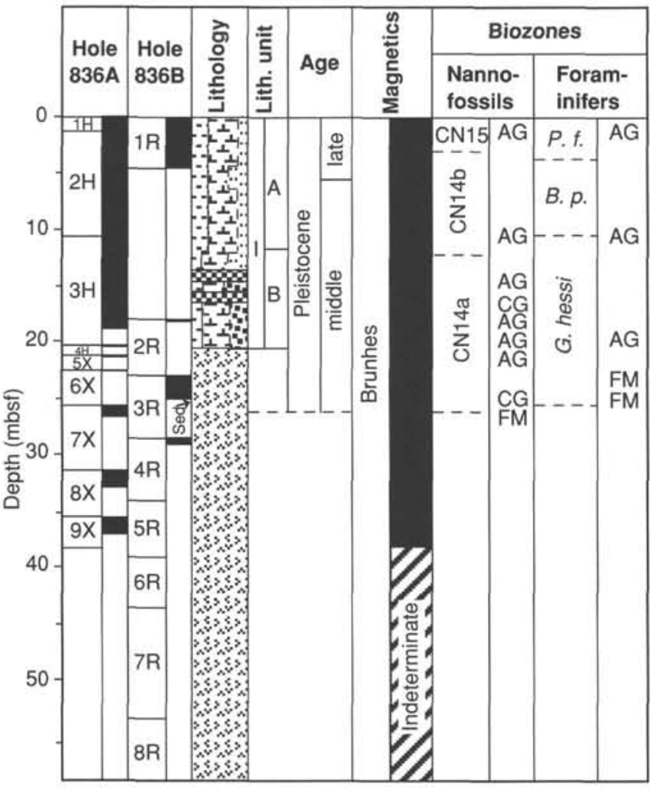

Figure 17. Paleontology summary chart, Site 836. See Figure 1 caption for an explanation of the symbols and abbreviations used.

interbedded coarse volcanic ash horizons; the amount of volcanic material greatly increases downcore, beginning with Core 135-836A-3H. The calcareous planktonic assemblages in the Pleistocene oozes and volcanic ash sands are very well preserved, but diversity is lower and preservation poorer in sediments associated with the basalt sequence.

Figure 18 is a graphic presentation of depth and age data from Site 836. The ages are based on the bioevents presented in Table 4. Paleomagnetic data have not been included in Figure 18 because no magnetic reversals were found. The curve may be divided into two parts: Section A, which represents sedimentation of the interbedded pelagic oozes and volcaniclastic sediments, was deposited at rates of about 25 mm/k.y. Section B contains thick volcaniclastic sediments and represents that part of the section overlying, and including, the basaltic sequence. This part of the curve is steeper, representing sedimentation rates of about 75 mm/k.y. The high sedimentation rates at Site 836 can be explained by the large amount of volcanic debris within the sequence, as the rates are higher than would be expected from pelagic sedimentation alone. The change in the slope of the curve at around 0.5 Ma represents a decrease of the volcanic component in the sediment.

PALEOMAGNETISM

The paleomagnetic measurement program at Site 836 was similar to that used at Sites 834 and 835. Archive halves of sediment and basalt cores were measured at 5-cm intervals with the pass-through cryogenic magnetometer, primarily to determine magnetic polarity. In addition to measuring the natural remanent magnetizations (NRMs) of the core sections, they were also magnetically "cleaned" using alternating-field (AF) demagnetization steps of 5, 10, and 15 mT. Because of time limitations, no discrete samples were studied. Volume magnetic susceptibility measurements were also made, using the Bartington MS-1 susceptibility meter with a 100-mm pass-through sensor on the multisensor track (MST). Susceptibility readings were made on whole-round core sections at 3-cm intervals on all Hole 836A APC cores and on relatively full basalt core sections from Holes 836A and 836B.

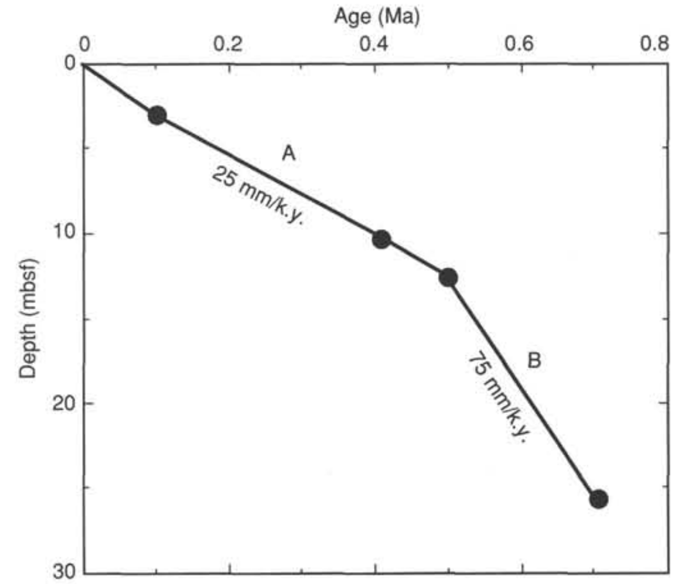

Figure 18. Graphic representation of age vs. depth data illustrating the sedimentation rates at Site 836 by means of the bioevents and depths given in Table 4.

Table 4. Depths and ages of bioevents used to plot accumulation rates for Site 836.

Depth (mbsf)	Age (Ma)	Events
3.0	0.10	FAD *E. huxleyi*
10.0	0.40	FAD *B. praeadamsi*
12.5	0.50	LAD *E. ovata*
20.0	0.60	LAD *Gr. (Tr.) tosaensis*

Remanent Magnetism

Magnetic Properties

Sediments from Hole 836A displayed magnetic properties much like those at previous sites. NRM intensities were generally strong, ranging from about 9 to 8000 mA/m, but typically falling between 10 and 100 mA/m. As at previous sites, the sediments are strongly magnetic in part because of abundant volcanic material and in part because of a pervasive, upward-directed overprint thought to be caused by the exposure of the sediments to strong magnetic fields in the drill string during coring. The sediments have low coercivity values, so they readily acquired a drill-string-induced isothermal remanent magnetization (IRM). Because of the low coercivity magnetic component, typical sediment median destructive forces (MDF) are low (2–5 mT; Fig. 19). However, the drill-string overprint seems to be effectively removed by AF demagnetization to 15 mT.

Basalt samples from Holes 836A and 836B had NRM intensities that ranged from 400 to 7000 mA/m. The basalts displayed low and high coercivity components. The drill-string IRM was usually apparent, but so was another, lower coercivity overprint that appeared random in direction (Fig. 19). This low-coercivity overprint was sometimes directed downward, so that a sample would become more magnetic at low AF demagnetization steps

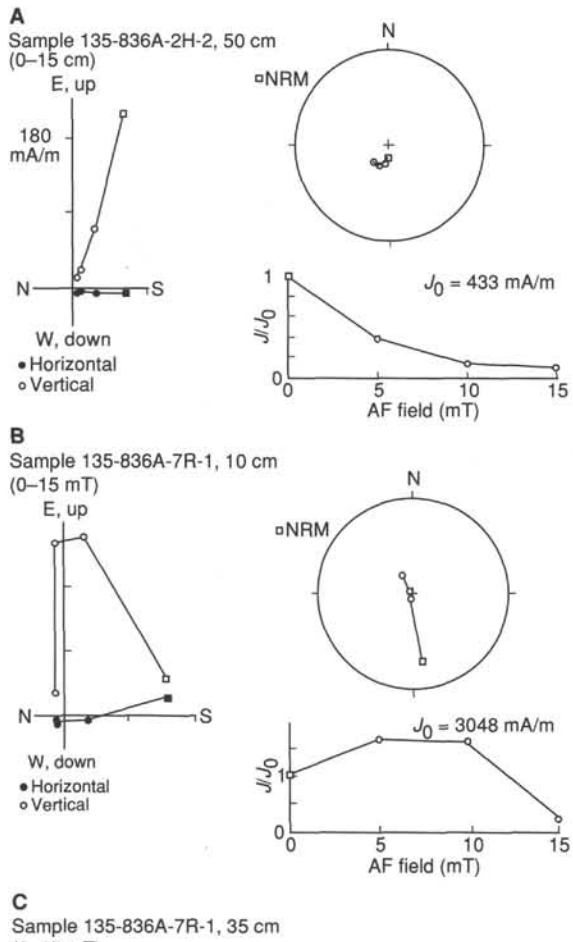

Figure 19. Behavior of Hole 836A samples during alternating-field (AF) demagnetization. **A.** Sedimentary Sample 135-836A-2H-2, 50 cm. **B–C.** Basalt Samples 135-836A-7R-1, 10 and 35 cm, respectively. For each sample, the following plots are given: upper right = equal-angle stereonet plot of magnetization vector endpoints at 0 (NRM), 5, 10, and 15 mT AF demagnetization steps; lower right = plot indicating the percentage of NRM remaining at various AF demagnetization steps; and left = orthogonal vector plot of vector endpoints during AF demagnetization. The sediment sample displays an upward-directed, drill-string-induced overprint that is largely removed by the 10-mT demagnetization step. This overprint is less obvious in the basalt samples.

as this overprint was removed and the upward drill-string overprint became more apparent. The low basalt coercivity values were characterized by MDFs typically <15 mT. Evidence of higher coercivity components was provided by the observation that the orthogonal vector plots of most basalt samples do not show a stable remanent magnetization direction at the 15-mT AF demagnetization step (Fig. 19). Because of this, polarity determinations of Site 836 basalt samples are somewhat uncertain.

Magnetic Polarity Stratigraphy

The sediments at Site 836 appeared to be faithful magnetic field recorders, revealing a reliable magnetic polarity after AF demagnetization to 15 mT (Fig. 19). Only three sediment cores (135-836A-1H through -3H) were recovered at Site 836 and all display magnetizations with negative inclinations averaging about –45° (Fig. 20), implying normal polarity. As these sediments are young (see "Biostratigraphy" section, this chapter), this normal period must represent the Brunhes Chron.

Only Core 135-836A-3H was oriented, so the magnetization declinations were variable (Fig. 20); however, in Core 135-836B-3H, the measured magnetic declinations are mostly near zero, as expected for a normal polarity magnetization. Departures from a consistent inclination and declination pattern occurred in hyaloclastite sand and gravel layers in Core 135-836A-3H. Because of their large grain sizes, these layers were unlikely to have accurately recorded the geomagnetic field when they were deposited. Moreover, they were also unlikely to have remained undisturbed during coring and subsequent processing of the cores.

Basalt samples in Holes 836A (Fig. 20) and 836B displayed dominantly normal polarities, consistent with having erupted during the Brunhes Chron. However, given the problems with determining the characteristic remanent magnetization directions of the basalt samples mentioned above, the true polarities are somewhat uncertain.

Magnetic Susceptibility

Volume magnetic susceptibility readings within the sediments ranged from 9×10^{-6} cgs to 319×10^{-6} cgs, with typical values of about 60×10^{-6} cgs. In the relatively homogeneous upper part of the sedimentary section (i.e., above about 12 mbsf), small susceptibility oscillations with wavelengths of about 20 cm to 1 m (Fig. 21) are similar to those observed at Site 834 that may represent Milankovitch cycles. The sedimentation rate determined for Site 836 (see "Sediment Accumulation Rates" section, this chapter) suggests that the 19 cycles in the upper 10 m of sediment have an average period of about 21 k.y., nearly that expected for the Milankovitch precession period.

Farther down, the cycles appear less regular, perhaps disrupted by being interspersed with hyaloclastite sands and gravels in Core 135-836A-3H (see "Lithostratigraphy" section, this chapter). The hyaloclastite layers yielded low, relatively constant susceptibility values, suggesting that they contain little magnetic material. At 17 mbsf, a susceptibility peak reaching 319×10^{-6} cgs correlates with a dark brown sediment layer. At Sites 834 and 835, the sediments containing the greatest amount of ferric oxyhydroxides were found to be darker brown and very magnetic (see "Paleomagnetics" section, "Site 835" chapter, this volume), so ferric oxyhydroxides may be the cause of this susceptibility peak.

Magnetic susceptibility values for basalts from Holes 836A and 836B display scatter over two orders of magnitude, partly because of variable volumes of material within the whole-round core sections. Thus, as mentioned in previous chapters, these measurements are minimal values and should be used only for reconnaissance. Most of the susceptibility values are between 200×10^{-6} and 2000×10^{-6} cgs, with the highest reading at 2124×10^{-6} cgs. Furthermore, it appears that the susceptibility values of basalts above and below about 42 mbsf are different. Those below are generally around $300–500 \times 10^{-6}$ cgs, whereas those above are mostly $700–2000 \times 10^{-6}$ cgs (Fig. 21). This change corresponds approximately to the boundary between igneous Units 3 and 4 with Unit 5, which shows a change from aphyric basalt to moder-

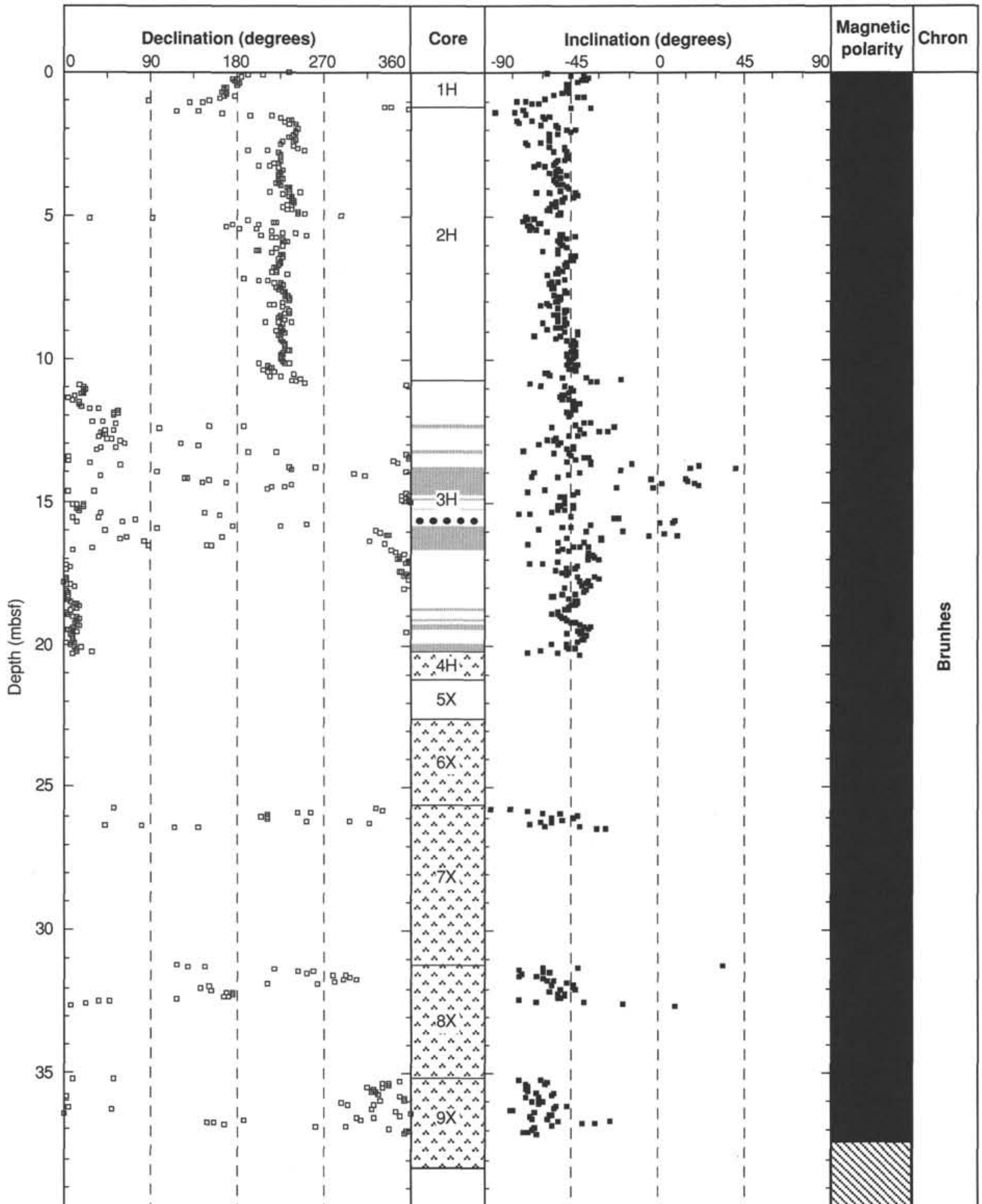

Figure 20. Magnetic polarity stratigraphy, Hole 836A. Large columns, left and middle, illustrate magnetization declination and inclination measurements, respectively, made with the pass-through cryogenic magnetometer on archive core halves after 15-mT AF demagnetization. Column in middle presents the core boundaries and a summary of the lithology. The chevron pattern is used to illustrate the cores containing basalt; stipple pattern denotes hyaloclastite layers in Core 135-836A-3H; and dot pattern indicates core with severe drilling disturbance. Column at far right shows magnetic polarity. Magnetic polarity chrons labeled at far right.

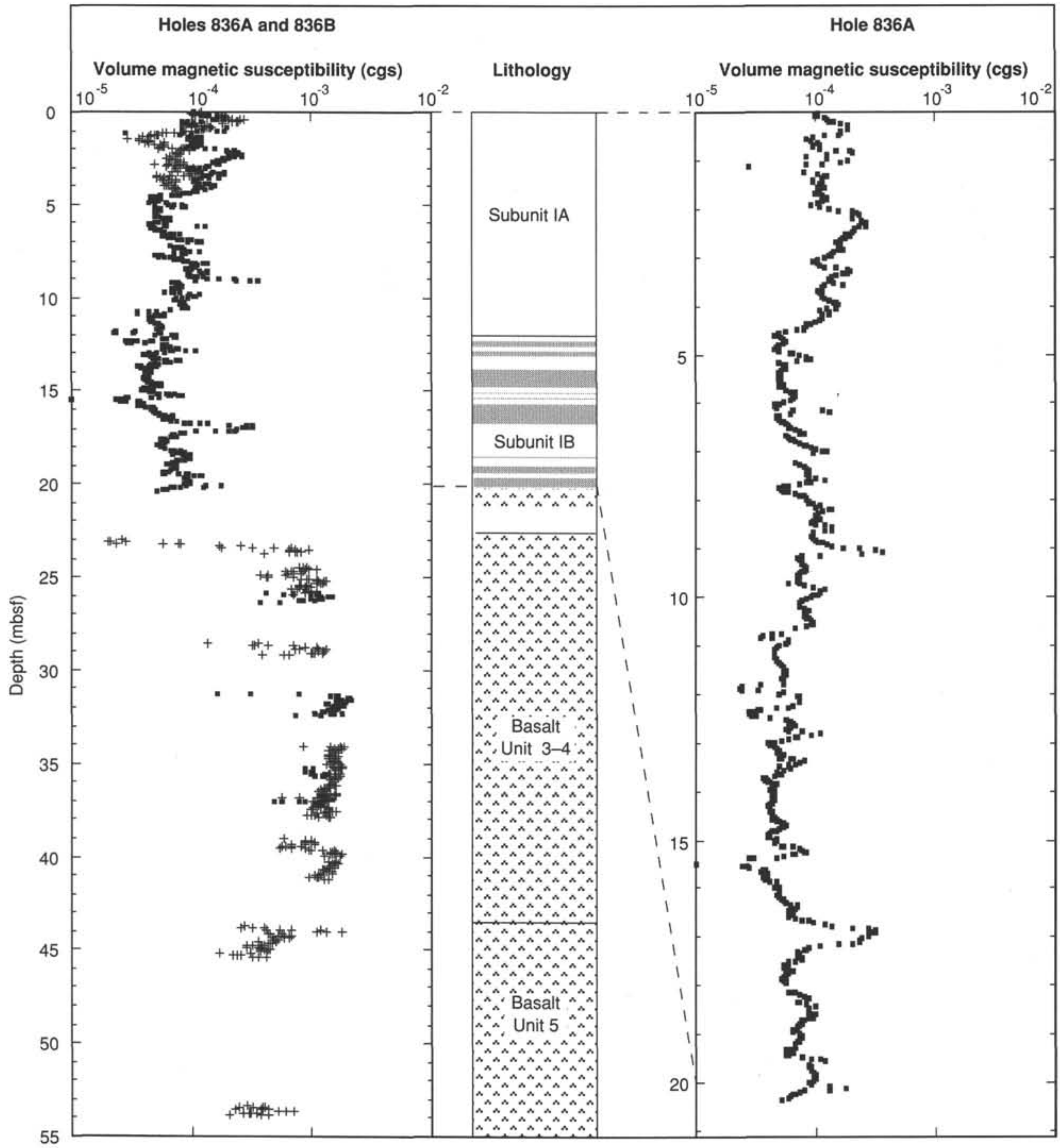

Figure 21. Volume magnetic susceptibility, Holes 836A and 836B. Column at left shows susceptibility values for both holes; squares represent measurements from Hole 836A, whereas crosses denote those from Hole 836B. Column at right is an enlargement of the susceptibility plot for the sediments of Hole 836A. Column in middle summarizes lithology. Sedimentary Units IA and IB shown at top; igneous Units 3–5 shown below. Stipple pattern denotes hyaloclastite layers; chevron pattern represents basalt.

ately phyric plagioclase-olivine basalt (see "Igneous Petrology" section, this chapter).

Core Orientation

Cores 135-836A-3H and -4H were oriented using the multishot tool. Core 135-836A-4H encountered basalt and returned virtually empty; thus, Core 135-836A-3H is the only oriented core obtained at Site 836. Orientation data for these cores are given in Table 5.

INORGANIC GEOCHEMISTRY

Introduction

Only two interstitial water samples were collected in Hole 836A, in Cores 135-836A-2H and -3H. Core 135-836A-1H was short (1.2 m), and the basement was reached at the bottom of Core 135-836A-4H at 21 mbsf. Standard ODP squeezing techniques were used for the removal of water samples (see "Explanatory Notes" chapter, this volume). The results are summarized in Table 6.

Table 5. APC core orientation data, Site 836.

Core no.	Camera no.	Compass	Inclination Direction	Inclination Drift	Declination
135-836A-					
3H	3209	A	N55°E	1°	132°
4H	3209	A	140°	0.5°	264°

Notes: Magnetic declination at the site is 13°E. Inclination is the off-vertical angle of the core; drift and direction are the dip angle and dip direction (clockwise from north) of a plane perpendicular to the core axis. Declination is the angle between the double line on the core liner and magnetic north (measured clockwise).

In Hole 836A, dissolved major constituents (chloride, sodium, calcium, magnesium, potassium, and sulfate) were determined. Magnesium measurements were made by EDTA titration and by means of flame AA spectrophotometry. Subsequent charge balance calculations yielded the sodium concentrations in the interstitial water samples. Ammonia, phosphate, silica, strontium, and manganese were also conducted with colorimetric methods and flame AA spectrophotometry.

Results

The chemical data obtained from these analysis of the dissolved constituents showed the same characteristics as those obtained in Holes 834A and 835A. The major constituent concentrations show values that are comparable with the average values for seawater. The values of dissolved ammonia and phosphate concentrations are very low and are consistent with the sulfate concentrations which vary little with depth. The values of dissolved ammonia, phosphate, silica, and strontium in Hole 836A are comparable with those obtained in the upper part of Holes 834A and 835A. However, note that the NH_4 concentrations are slightly higher than those obtained in these previously studied holes.

Mn concentrations reach values below the limit of detection of the flame AA spectrometer (e.g., 10 µM, considering a dilution of about 1:5 in the samples). These low Mn concentrations must be related to the thin sedimentary cover sequence.

Conclusion

As previously mentioned for Holes 834A and 835A, the interstitial water data obtained in Hole 836A suggests a downwelling flow of bottom seawater through the sedimentary column, with little evidence of interstitial water-rock exchange.

ORGANIC GEOCHEMISTRY

Shipboard organic geochemical analysis of samples from Hole 836A consisted of two determinations of volatile hydrocarbons in sediments using the Carle gas chromatograph, eight determinations of total nitrogen, carbon, and sulfur using the Carlo Erba NCS analyzer and 18 determinations of total inorganic carbon using the Coulometrics 5011 coulometer equipped with a System 140 carbonate/carbon analyzer. The low number of analyses reflects the thin sedimentary section encountered at this site. Details of the analytical procedures used are outlined in the "Organic Geochemistry" section of the "Explanatory Notes" chapter (this volume), and are described in detail by Emeis and Kvenvolden (1986).

The volatile hydrocarbon gases were obtained from the bulk sediment using the head-space sampling technique and were routinely monitored for methane, ethane, and propane. One sample was taken from each of the second and third APC cores. The concentration of methane in both samples was between 2 and 3 ppm, which is very low and at the laboratory background level. Ethane and propane were not detected. The extremely low concentration of methane indicates that methanogenesis is not occurring in these sediments. Unless the bottom waters were anoxic, which is extremely unlikely in an open-ocean depositional setting, this would be expected because of the shallow sediment depths penetrated.

Determinations of inorganic carbon (IC) contents were performed on the samples used for physical properties and on additional samples selected by the sedimentologists. Percent $CaCO_3$ is calculated according to the equation:

$$CaCO_3 = IC \cdot 8.334.$$

This equation assumes that all the carbonate is present as calcite. The data from these analyses are presented in Table 7. Carbonate values range from <15.7% to 56.3%. Carbonate values are discussed in more detail and related to the lithostratigraphic units in the "Lithostratigraphy" section (this chapter).

Also shown in Table 7 are the percentages of total carbon and sulfur for the eight samples measured. The nitrogen content was also measured but not detected in any of the samples analyzed. Total organic carbon (TOC) is defined here as the difference between the total carbon and the inorganic carbon values. The sediments from Site 836 have organic carbon contents between 0.07% and 0.53%. This latter value from a depth of 0.55 mbsf in early Pleistocene sediments is the highest value obtained so far on Leg 135. The TOC content shows no correlation with depth or with percentage of carbonate. Sulfur was only detected in four of the eight samples analyzed and in these was in extremely low abundance.

IGNEOUS PETROLOGY

Introduction

Site 836 is located on what is interpreted as relatively young Lau Basin crust, formed at the active ELSC (the present backarc axis), which lies approximately 50 km east of the site. The site lies approximately 100 km south of the southern termination of the actively southward propagating CLSC (Parson et al., 1990), and 60 km east of the postulated line of an extinct spreading axis, the Western Lau Spreading Center (WLSC).

Five igneous units were identified in the two holes drilled at this site (Fig. 22); Units 2 and 3 are interbedded with, and Units 3–5 overlain by, sediments having a maximum age of middle

Table 6. Interstitial water chemistry data, Hole 836A.

Core, section, interval (cm)	Depth (mbsf)	pH	Alkalinity (mM)	Salinity	Ca^{2+} (mM)	Mg^{2+} (1) (mM)	Mg^{2+} (2) (mM)	K^+ (mM)	Cl^- (mM)	SO_4^{2-} (mM)	NH_4^+ (µM)	PO_4^{3-} (µM)	Si^{4+} (µM)	Sr^{2+} (µM)	Na^+ (1) (mM)	Na^+ (2) (mM)
135-836A-																
2H-4, 140–150	7.2	7.71	3.094	35.4	10.8	52.4	52.7	11.2	549	27.8	17	3.6	290	99	468	467
3H-5, 140–150	16.7	7.49	2.384	35.0	10.3	51.9	52.6	11.6	548	28.0	42	2.4	288	104	467	468

Notes: Mg (1) derived from EDTA titration; Mg (2) derived by flame AA spectrometry; Na (1) derived from charge balance calculations using Mg (1); Na (2) used those of Mg (2).

Table 7. Concentrations of inorganic and organic carbon and total sulfur, Hole 836A.

Core, section, interval (cm)	Depth (mbsf)	Total carbon (%)	Inorganic carbon (%)	Organic carbon (%)	$CaCO_3$ (%)	S (%)	OrgC/S	OrgC/N
135-836A-								
1H-1, 55–56	0.55		3.42		28.5			
1H-1, 57–58	0.57	3.64	3.11	0.53	25.9			
2H-1, 62–63	1.82	3.08	2.83	0.25	23.6	0.01	25	
2H-2, 74–75	3.44		4.31		35.9			
2H-3, 63–64	4.83	5.90	5.69	0.21	47.4	0.01	21	
2H-3, 85–86	5.05		5.58		46.5			
2H-4, 70–71	6.40	5.18	5.11	0.07	42.6	0.07	1	
2H-5, 67–68	7.87		6.50		54.1			
2H-6, 71–72	9.41	6.9	6.76	0.14	56.3			
2H-6, 125–126	9.95		6.31		52.6			
3H-1, 79–80	11.49	6.02	5.89	0.13	49.1	0.02	6.5	
3H-2, 45–46	12.65		2.22		18.5			
3H-2, 69–70	12.89		1.89		15.7			
3H-5, 20–21	16.78	3.87	3.67	0.20	30.6			
3H-5, 66–67	17.24		4.69		39.1			
3H-6, 16–17	18.24		3.31		27.6			
3H-6, 69–70	18.77	4.76	4.43	0.33	36.9			
3H-6, 104–105	19.12		3.73		31.1			

Pleistocene (see "Biostratigraphy" section, this chapter), confirming the young age of the igneous units. The two uppermost units are fresh, glassy, sparsely phyric, andesitic hyaloclastites. Underlying these are three basaltic units composed of moderately phyric olivine-plagioclase basalt (Unit 3); a fine-grained, but somewhat diabasic-textured, sparsely phyric plagioclase basalt (Unit 4); and a sparsely to moderately phyric olivine-clinopyroxene-plagioclase basalt (Unit 5). Table 8 summarizes the lithology, thicknesses, and core depths of the units.

Core recovery was very low for Unit 3 (2.8%–6.2%), between 27.5% and 44.4% for Unit 4, and 15.9% for Unit 5. The numbers of individual cooling units within Units 4 and 5 have been estimated from the numbers of glassy to microlitic zones per meter of recovered core and from calculating a core average (Fig. 23). The results indicate the presence of multiple cooling units. Unit 4 is relatively massive, but there seems to be a slight increase in the number of cooling units toward the top. Unit 5 appears to comprise thinner cooling units than Unit 4.

Lithology and Petrography

Units 1 and 2

Sparsely Phyric Plagioclase Andesite

Units 1 and 2 were recovered only in Hole 836A; Hole 836B, situated 20 m south of Hole 836A, was washed down from 4.5 to 18.0 mbsf, thus precluding their recovery. The topmost igneous unit (Unit 1) was intersected at 13.39 mbsf and comprises 91 cm of sparsely phyric plagioclase glass-rich andesitic gravel (Section 135-836A-3H-3, 8–99 cm). A 5-cm-thick intercalated ash layer is present 45 cm below the top of the layer. The gravel consists almost entirely of black glassy fragments (<5% gray finely crystalline component), ranging from <1 mm to 2 cm in size. The fragments are vesicular; many fragments are markedly angular with sharp conchoidal fractures, although some preserve delicate vesicular structures, which indicates that little reworking has occurred. The unit is interpreted as a hyaloclastite.

A second sparsely phyric plagioclase glass-rich andesitic horizon (Unit 2) occurs at 15.23 mbsf (Section 135-836A-3H-4, 50–150 cm). This also consists of angular and vesicular fragments, <1 mm to 1.5 cm in size, and is interpreted as a hyaloclastite that has not undergone significant reworking. The unit is overlain by 20–30 cm of indurated and bedded ash.

No thin sections were prepared from Unit 1, but macroscopic examination indicates that it is very similar to Unit 2. Petrographic examination of Unit 2 was made on a thin section comprising six separate fragments, each between 0.5 and 1 cm across. The fragments consist of fresh vesicular glass with rare (≤1%) microphenocrysts of plagioclase, clinopyroxene, and orthopyroxene. Modal analyses are in Table 9.

The color of the glassy groundmass ranges from extremely fresh, light tan glass to a darker glass because of the extensive development of crystallites (considered to be plagioclase), some in distinctive radiating aggregates and with swallow-tail morphologies (Fig. 24). Randomly oriented microphenocrysts occur throughout the glassy matrix. Plagioclase grains (up to 1 mm in length) exhibit quench morphologies such as elongate laths and swallowtail terminations; radial grain clusters are common. The larger phenocrysts typically possess narrow, distinct, more sodic rims. Euhedral to subhedral clinopyroxene and orthopyroxene microphenocrysts are up to 0.7 mm in length. Orthopyroxene in particular develops perfectly formed prismatic crystals (Figs. 25 and 26), whereas many clinopyroxene crystals exhibit inclusions and marginal imperfections. Clinopyroxene-orthopyroxene intergrowths also occur.

The vesicle content of these units ranges from 40% to 45%. Vesicles are up to 1.4 mm across (most are <0.5 mm) and are rounded to subrounded in shape. The largest vesicles have a very irregular shape because of their development by the coalescence of smaller vesicles. In some fragments, the vesicles are highly elongate (perhaps indicating volatile streaming or deformation during flow), whereas in others they are spherical. The majority of vesicles are devoid of infilling, but rare Fe or Mn oxide linings are occasionally present. The rock fragments are coarsely graded, but they are relatively unsorted. The preservation of angular shape and conchoidal fractures indicates that they have not been transported long distances. Although the rocks are very vesicular, they are not pumiceous; thus, it is doubtful that they could have been transported as floating fragments. The relatively high vesicle content of the rock makes an extremely fragile network with the distance between vesicles rarely more than a few tenths of a millimeter. The angular fragments, poor sorting of the unit, conchoidal fractures, and relatively large, yet fragile fragments suggest that the source of the gravel is relatively close to its site of deposition. Thus, it is considered unlikely that these fragments were derived from andesites erupted along the Tofua Arc (125 km

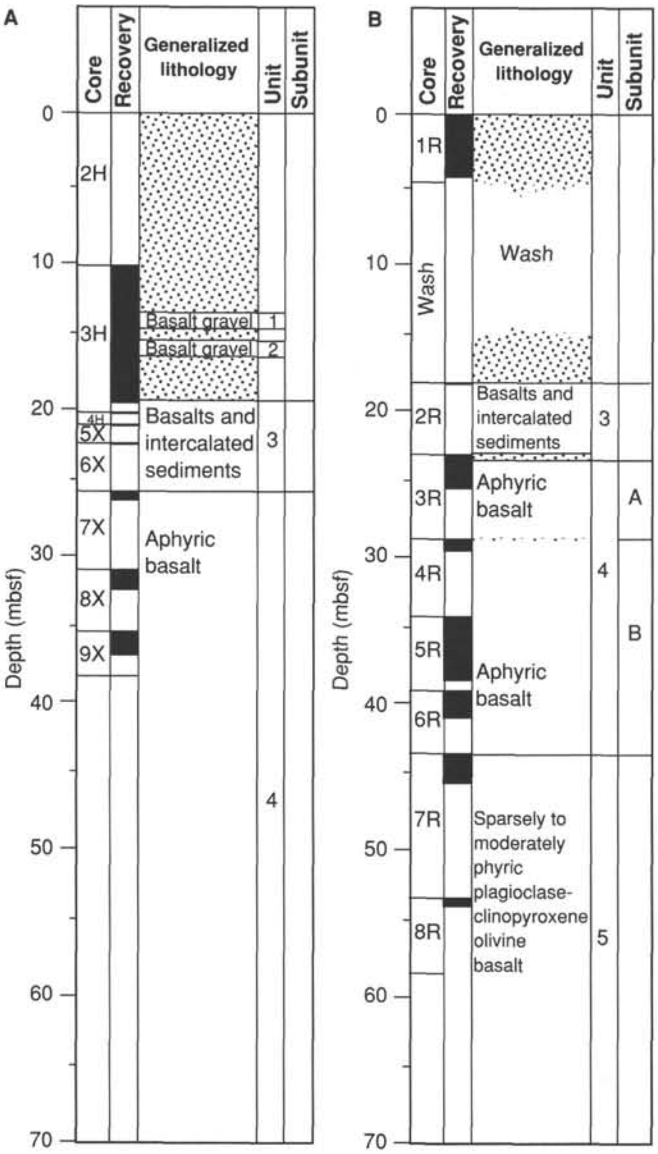

Figure 22. Schematic summary of the igneous lithologic units recovered in Holes 836A (**A**) and 836B (**B**).

to the east of Site 836) and transported by submarine processes to this location. The occurrence of orthopyroxene in this sample, interpreted above as originating within the Lau Basin, is petrologically very interesting, and is consistent with the andesitic chemistry of the sample (Table 10). The only previously reported orthopyroxene occurrence in the Lau Basin is on Zephyr Shoal, about 475 km north of Site 836 (Hawkins, 1976, 1985).

Unit 3

Basalt Fragments with Intercalated Sediments

Unit 3 comprises a sequence of interlayered volcanic and sedimentary lithologies. In Hole 836A, it first occurs in Section 135-836A-3H-CC, 0–10 cm (19.73 mbsf; 10 cm recovered) as one large and several small fragments of fine-grained to microlitic basalt with glass rims and some adhering indurated sediment. More small basaltic rock and glass fragments occur in Sections 135-836A-4H-CC, 0–13 cm (21.1 mbsf), -5X-1, 0–11 cm (21.2 mbsf; 11 cm recovered), and -6X-1, 0–10 cm (22.7 mbsf; the 10-cm recovery includes indurated mudstone fragments). The lower boundary of Unit 3 in Hole 836A is placed at the base of the mixed basalt and sediment intercalation in Section 135-836A-6X-1, 11 cm. There is also a marked petrographic similarity to the basalt fragments down to this depth. The better recovery of massive basalt in Section 135-836A-7X-1 defines the top of Unit 4. This suggests a nominal thickness of 5.97 m for Unit 3 (an estimate that is subject to much uncertainty in view of the very low [6.2%] recovery).

In Hole 836B, the uppermost basalt was recovered in Section 135-836B-2R-1, 12 cm (18.09 mbsf), as irregular, broken fragments equivalent to no more than 6 cm of core length. These fragments are overlain by 11 cm of sediment and underlain by at least 46 cm of sediment that was recovered in Section 136-836B-3R-1 (top at 23.0 mbsf). In hand specimen, the basalt is sparsely plagioclase phyric, fine grained, and vesicular. It is correlated with Unit 3 of Hole 836A. Core recovery was only 2.8%.

The volcanic rocks from Unit 3 are predominantly sparsely phyric, olivine-plagioclase vesicular basalt, with <1%–2% plagioclase and traces of olivine phenocrysts. The fragments in the two lower cores are strongly vesicular (5%–25% vesicles). The groundmass is a matrix of plagioclase, clinopyroxene, olivine, and very fresh cryptocrystalline mesostasis (Table 9). Plagioclase phenocrysts are blocky and tabular, up to 1 mm in size, and comprise 1%–2% of this unit. The largest grains appear to have undergone some incipient resorption. Olivine phenocrysts are up to 0.4 mm in diameter and are typically intergrown with plagioclase in small glomeroporphyritic clusters; some olivines are skeletal (Fig. 27). Trace amounts of euhedral Cr-spinel (to 0.08 mm across) are included in some plagioclase grains and in the groundmass.

Plagioclase and clinopyroxene are the dominant groundmass phases in Unit 3, and both phases commonly show quench morphologies (Figs. 27 and 28). Plagioclase laths (many with swallow-tail morphology) are up to 0.5 mm in length, whereas feathery clinopyroxene grains are <0.25 mm in length. Euhedral to subhedral olivine is a minor (<2%) groundmass phase. Plagioclase, clinopyroxene, and olivine are commonly intergrown to form very fine-grained acicular bundles or feathery aggregates with quenched plagioclase grains having served as nucleation sites for the clinopyroxene. Skeletal and euhedral magnetite grains, <0.01 mm across, are disseminated throughout the groundmass. The remaining groundmass is microcrystalline mesostasis although clinopyroxene crystallites are occasionally discernible in this fine-grained material.

The vesicle content of Unit 3 is 15%–20%, and vesicles range in size up to 1.2 mm. The largest vesicles are elongated and sometimes appear to have developed by the coalescence of a number of smaller vesicles. Relatively large (4–6 mm diameter) dark areas of highly vesicular, quenched, basaltic material occur as discrete patches, linings to vesicles, and bands cutting across the core.

Unit 3 has undergone only minor alteration, with replacement of 1%–2% of the original mesostasis by cryptocrystalline, greenish brown clays. Some vesicles are partially lined with clays and/or iron-oxyhydroxide staining.

Unit 4

Aphyric Basalt

Subunits 4A and 4B, separated by a thin sediment intercalation (see below), are defined in Hole 836B; no such division could be defined in Hole 836A. In Hole 836A, Unit 4 is recognized in Section 135-836A-7X-1, 0 cm (top 25.7 mbsf), through to 135-836A-9X-2, 147 cm (36.81 mbsf, total depth of the hole). Core recovery was approximately 27.5%. The drillers cored 11.11 m of

Table 8. Principal lithologic units defined at Site 836.

Unit	Lithology	Hole 836A Top depth (mbsf) Core, section, interval (cm)	Hole 836A Bottom depth (mbsf) Core, section, interval (cm)	Hole 836B Top depth (mbsf) Core, section, interval (cm)	Hole 836B Bottom depth (mbsf) Core, section, interval (cm)	Distinguishing features
1	Glassy andesitic gravel	13.39 3H-3, 8	14.26 3H-3, 99	Not recovered		Coarse sand to pebble-sized fragments of plagioclase-bearing andesite
2	Glassy andesitic gravel	15.23 3H-4, 50	16.19 3H-4, 150	Not recovered		Coarse sand to pebble-sized fragments of plagioclase-bearing andesite
3	Various basalt fragments with intercalated sediment	19.73 3H-CC, 0 (Piece 1)	25.70 6X-1, 11	18.09 2R-1, 12 (Piece 2)	23.35 3R-1, 46 (Piece 8)	Aphyric basalts, plagioclase-bearing basalts as fist-sized pieces and smaller drill rubble; intercalated sediment or sediment fragments
4	Aphyric basalt	25.70 7X-1, 0 (Piece 1)	36.81 9X-2, 47 (Piece 4)	Split into A and B subunits		Aphyric basalt; massive flows; vesicular
4a	Aphyric basalt	Not defined		23.35 3R-1, 46 (Piece 8)	28.50 4R-1, 0	Aphyric basalt; massive flows; vesicular
4b	Aphyric basalt	Not defined		28.57 4R-1, 9 (Piece 2)	43.77 7R-1, 10 (Piece 2)	Aphyric basalt; massive flows; vesicular
5	Sparsely to moderately phyric plagioclase clinopyroxene olivine basalt	Not recovered		43.77 7R-1, 10 (Piece 3)	53.92 8R-1, 72 (Piece 12)	3%–8% phenocrysts; highly vesicular

Notes: Unit boundaries reflect changes in principal lithology defined in visual and thin section descriptions. Subunits were defined by intervals of sediment between similar lithologies.

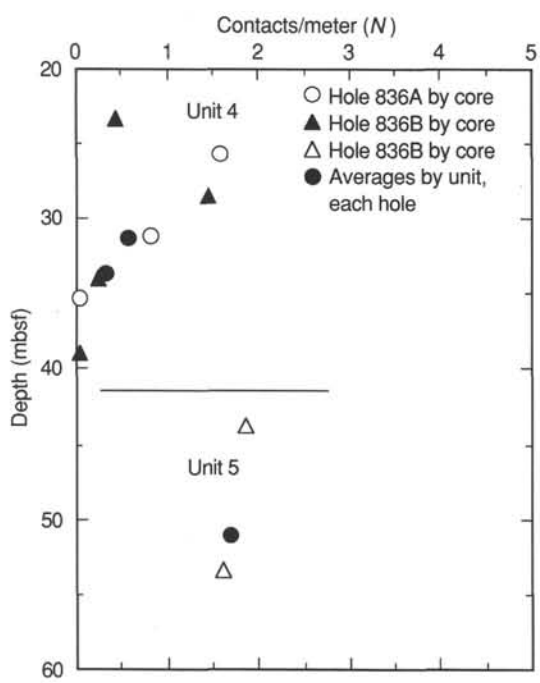

Figure 23. Data for cooling contacts per meter, plotted for Units 4 and 5 cored in Holes 836A and 836B. Recovery from Unit 3 was too low to provide sufficient data. Averages by unit represent total contacts in the unit divided by total meters recovered for that unit. All other points are for individual cores. Methodology is discussed in the "Igneous Petrology" section, "Site 834" chapter (this volume).

Unit 4, but the bottom contact of the unit was not recovered. In hand specimen, this basalt is distinct in possessing a predominantly diabasic and seriate texture, with few or no clearly defined phenocrysts. A thin remnant glassy rind on a fragment in Section 135-836A-7X-1 (Piece 2) and two fine-grained and strongly vesicular fragments in Section 135-836A-8X-1 (Pieces 1 and 2) indicate several cooling units.

In Hole 836B, the top of Unit 4 was recovered in Section 135-836B-3R-1, 46 cm (23.35 mbsf), Piece 8. This topmost fragment has a glassy quenched rim, whereas the underlying fragment (Piece 9) contains mixed sediment and basalt fragments, indicating that the flow top was at least partially recovered. Unit 4 extends down to Section 135-836B-7R-1, 10 cm (43.77 mbsf), but the occurrence of a 10-cm sediment intercalation at the top of Section 135-836B-4R-1, 0–10 cm (28.5–28.6 mbsf), is considered sufficient evidence to establish Subunits 4A and 4B; these have nominal thicknesses of 5.15 and 15.2 m, respectively. The combined core recovery in these subunits is 44.4%.

In hand specimen, the basalt of Unit 4 is massive, aphyric, holocrystalline, seriate, and in places ophitic, approaching a diabasic texture. Fresh samples are gray to dark gray. Interlocking tabular plagioclase and subhedral to anhedral clinopyroxene (± trace olivine) are visible as the main phases. The largest of the plagioclase grains tend to approach phenocryst size, but their abundances are estimated to be <1%. The unit is vesicular, with most specimens estimated to have 20%–40% vesicles, ranging in size from 0.1 to 6.0 mm. Vesicle shapes are generally very irregular. The smaller vesicles are uniformly distributed, but the larger ones are distributed more unevenly in clusters; pipelike vesicle structures are sporadically developed (e.g., Cores 135-836B-3R and -5R).

Table 9. Modal analyses (>700 points) of representative samples from Holes 836A and 836B.

Hole	836A	836B	836A	836A	836B	836B
Core, section	3H-4	2R-1	5X-1	9X-2	5R-2	7R-1
Interval (cm)	75–150	14–16	0–11	45–47	92–93	31–32
Piece	None	2	1	4	2	6
Unit	2	3	3	4	4	5
Depth (mbsf)	16.25	18.12	21.25	36.80	36.42	43.94
Phenocrysts:						
Plagioclase	0.5	1.8	1.4	0.3	0.9	3.1
Clinopyroxene	0.3	—	—	0.3	—	1.0
Olivine	—	0.8	0.4	0.1	—	Tr
Orthopyroxene	0.3	—	—	—	—	—
Total phenocrysts	1.1	2.6	1.8	0.7	0.9	4.1
Vesicles:						
Open vesicles	41.0	14.2	18.2	16.3	27.4	35.7
Filled vesicles	—	0.2	0.8	2.6	1.5	—
Total vesicles	41.0	14.2	19.0	18.9	28.9	35.7
Groundmass:						
Plagioclase	—	12.1	22.3	35.0	33.3	2.4
Clinopyroxene	—	0.8	19.4	23.0	17.8	2.8
Olivine	—	1.5	1.5	2.2	1.7	—
Opaques	—	1.8	1.5	2.1	1.1	3.2
Mesostasis	57.9	66.7	32.1	18.2	16.3	51.6
Total groundmass	57.9	82.9	79.2	80.5	70.2	60.0
N	1121	1069	1035	1057	787	1112
Plag/cpx (phenocrysts)	1.7	—	—	1	—	3.1
Plag/ol (phenocrysts)	—	2.2	3.5	3.0	—	—

Notes: Phenocrysts were generally identified as larger, more blocky or tabular crystals. Several of the samples are seriate porphyritic and the phenocrysts grade in size into the groundmass laths. Plag = plagioclase, cpx = clinopyroxene, and ol = olivine. *N* = number of points counted, and Tr = trace.

The basalt shows extensive zones of brownish discoloration resulting from low-temperature oxidative alteration. Infillings of vesicles by globular zeolites and acicular aragonite (including some spectacular acicular growth clusters; Fig. 29; Section 135-836A-8X-1, Piece 4B), together with minor iron-oxyhydroxides and rare manganese oxides, are present throughout the unit, but are more extensive in the upper part and in the altered zones. Subvertical fractures, 1 mm wide, are sporadically present and are also filled by the same phases as occur in the vesicles. In Section 135-836B-6R-2 (Pieces 1B–1C), a complex set of internal quench zones, flow boundaries, and intrusive structures are observed (Fig. 30).

In thin section, rocks of Unit 4 are fine grained, yet distinctly diabasic and seriate in texture. They are composed of interlocking plagioclase, clinopyroxene, and olivine grains with a small amount of interstitial mesostasis and variable vesicle content. The seriate texture and the glomeroporphyritic intergrowths make the distinction between phenocrysts and groundmass phases arbitrary. Plagioclase is the dominant phenocryst phase (<2%), forming relatively large and equant blocky crystals up to 1.5 mm in diameter.

The groundmass of Unit 4 is composed of interlocking plagioclase and clinopyroxene with minor olivine and opaque minerals and interstitial mesostasis. Plagioclase forms elongate laths and tabular microlites and occasionally exhibits zoning, especially at the crystal margins. Subhedral to anhedral clinopyroxene grains are equant and tend to form ophitic intergrowths with plagioclase (Fig. 31). The clinopyroxene grains show both sector zoning and compositional core-to-rim zoning. Subhedral olivine (up to 0.4 mm) constitutes approximately 2% of the groundmass. It most commonly occurs as isolated grains, but in some instances is intergrown with plagioclase and clinopyroxene.

Magnetite is the dominant opaque phase. It makes up to 3% of the groundmass and occurs as both large, discrete, equant or cruciform grains and as fine, elongate, skeletal crystals in the mesostasis. Ilmenite is absent as a primary phase, but rare ilmenite lamellae within magnetite grains do occur. Rare sulfide globules, <0.01 mm in diameter, occur either as interstitial groundmass grains or on the interior walls of vesicles. Trace amounts of dark brown, euhedral Cr-spinel (≤0.03 mm across) are occasionally included in the plagioclase grains.

Interstitial mesostasis comprises up to 20% of this unit and has been completely replaced by extremely fine-grained to cryptocrystalline green brown clays. This microcrystalline material occurs in fibrous growths and microspherulitic aggregates. Fine-grained, green-brown clays fill vesicles. Despite this alteration, the primary minerals are remarkably fresh.

Some samples from Unit 4 have textures suggesting mixing of magmas. As noted above, in Section 135-836B-6R-2 a complex set of internal quench textures, flow boundaries, and intrusive structures were observed (Fig. 30). In thin section, the basalt has two distinct grain-size lithologies (Fig. 32); one is fine grained with an equigranular texture. The intimately intergrown patches of coarser and finer grain sizes suggest that there was internal magma mixing before crystallization was complete, which produced the apparent recrystallization textures. Embedded in the granular groundmass are phenocrysts and microphenocrysts of euhedral to subhedral plagioclase, olivine, and clinopyroxene. Although the seriate texture makes the distinction between phenocrysts and groundmass somewhat arbitrary, the contrasting size and shape of these crystals compared to the granular groundmass gives the rock a distinctly porphyritic texture. The mineralogical characteristics of the finer and coarser grained areas are similar, although the finer grained lithology may contain slightly more clinopyroxene. Therefore, the major cause of the mottled texture (especially obvious in hand specimen) apparently results from variations in grain size and texture rather than mineralogy. Rare Cr-spinels are associated with plagioclase phenocrysts, and some of these spinels have narrow magnetite rims that may have developed in response to the melt mixing processes (implying differing redox conditions or more evolved residual liquid composition after mixing). The vesicle content in these samples from the mixed region is significantly lower than other portions of Unit 4, with randomly distributed, relatively small (<1 mm) vesicles composing 10% of the rock. In contrast to other samples in Unit 4, vesicles adjacent to this mixed zone are generally completely infilled with clays and zeolites. Typical infills show a zonation from brown and pale green clays at the margins to apple-green, fibrous material followed by iron oxyhydroxides toward the center of the void. Some are completely infilled with acicular aragonite. Sulfide globules occur within or adjacent to vesicle margins in this region and are more abundant than in other portions of Unit 4.

Unit 5

Sparsely to Moderately Phyric Plagioclase Clinopyroxene Olivine Basalt

Unit 5 was recovered in core from Section 135-836B-7R-1, Piece 3 (43.77 mbsf), to Core 135-836B-8R-1 (53.92 mbsf), but the base was not intersected. Thus, it has a minimum thickness of 10.15 m (recovery 15.9%). Additional material belonging to the same unit was also recovered in Core 135-836B-9M-1, but its exact stratigraphic position within the unit is unknown. Relict glassy rinds and unusually highly and coarsely vesicular samples (taken to indicate flow and/or pillow contacts) are seen in Sections

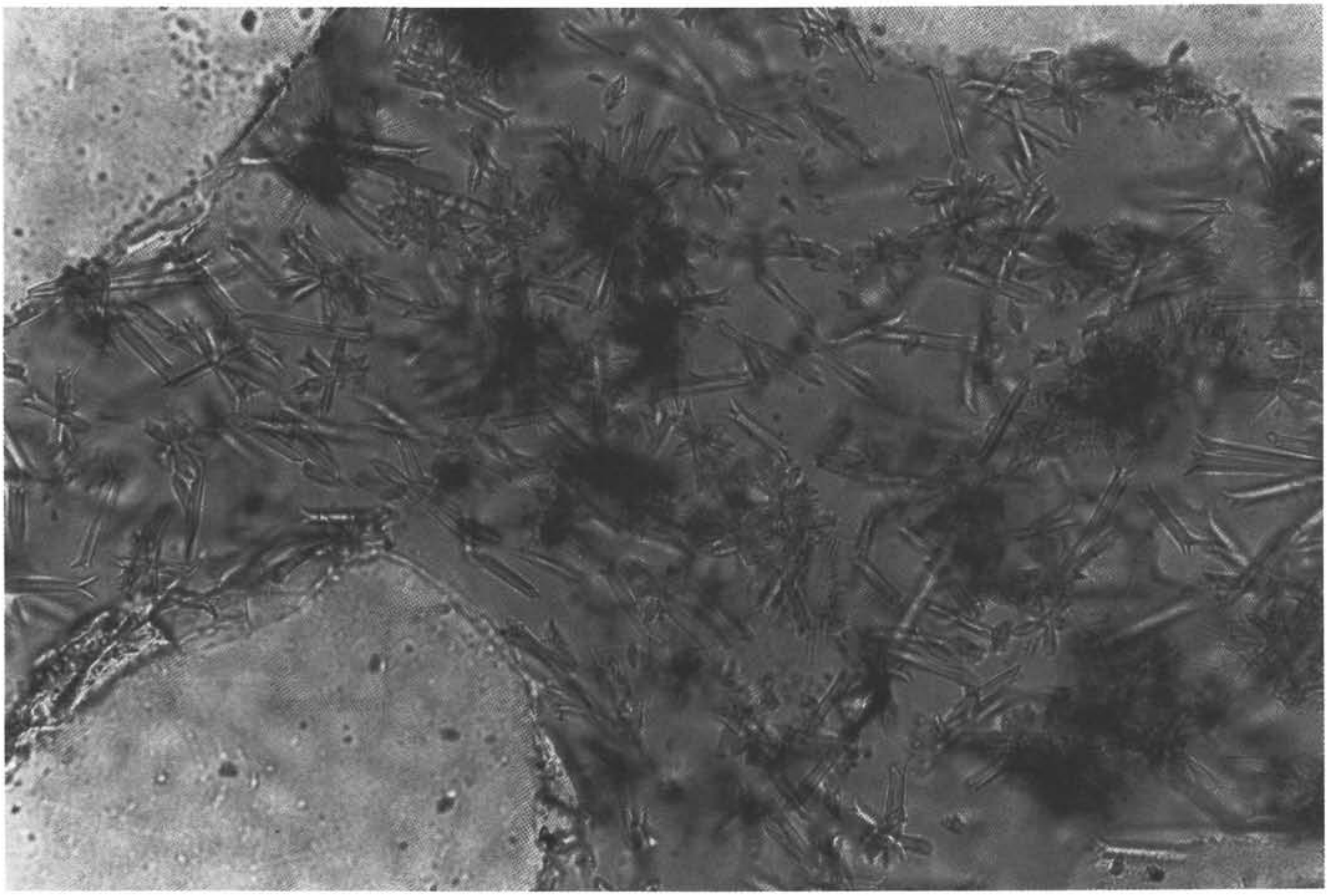

Figure 24. Photomicrograph of plagioclase crystallites in vesicular andesite glass, Unit 2, Section 135-836A-3H-4, 75–150 cm; field of view = 0.3 mm, ordinary light.

135-836B-7R-1 (Piece 4) and -9M-1 (Pieces 1, 5, and 13), indicating multiple cooling units. Hand specimens show the presence of olivine (<1%), pale green clinopyroxene (2%–3%; up to 2 mm), and plagioclase (1%–2%; up to 2 mm) phenocrysts, set in a very fine-grained and highly vesicular dark gray matrix. Vesicle abundances are estimated to range between 25% and 40%; they range in size between <0.1 to 7.0 mm. Vesicle shapes vary from rounded for the smaller vesicles to irregular for the larger ones, probably a result of coalescence. Infillings of yellow-brown to brown clays and iron oxyhydroxides occur, but they are very rare. Thin glassy selvages line some vesicles. Darker, aphyric, and highly vesiculated quenched basaltic material forms segregation infillings within preexisting vesicles. Veins are rare, very thin, and discontinuous when present.

Unit 5 is a highly vesicular, sparsely to moderately phyric, olivine-clinopyroxene-plagioclase basalt. Phenocrysts (plagioclase > clinopyroxene > olivine) comprise approximately 2%–5% of the rock. Euhedral to subhedral plagioclase phenocrysts up to 1.2 mm across form equant and tabular grains. Both normal and reverse zoning are observed and melt inclusions are present in some grains. Clinopyroxene phenocrysts up to 0.35 mm are anhedral to subhedral. The larger clinopyroxenes commonly show curved crystal forms and exhibit undulose extinction, attributed to growth during rapid cooling. Plagioclase and clinopyroxene frequently occur in glomeroporphyritic intergrowths of 2–15 grains. Rare subhedral olivine grains occur as single crystals near the plagioclase-clinopyroxene glomerocrysts.

The groundmass is dominantly microcrystalline interstitial mesostasis. Some euhedral to subhedral, isolated grains occur, but the groundmass is mostly comprised of quenched plagioclase and pyroxene sheaves with disseminated opaques. Unit 5 is very fresh; alteration is limited to very minor replacement of the mesostasis by cryptocrystalline clays and iron oxyhydroxides.

Alteration

Alteration of the rocks at Site 836 is comparable with Sites 834 and 835. Changes in color of the rocks from dark gray to greenish gray occurs with the passage of alteration fronts that can be observed throughout most of the core. The boundary between gray and greenish gray areas is very sharp and does not appear to be controlled by fractures. These zones cannot be distinguished mineralogically. In addition to iron hydroxide, fractures are sometimes covered by a yellowish white, very soft, talclike mineral. These fractures have acted as the surfaces of preferred breakage during drilling. Vesicles, rarely up to 1 cm in diameter, are often lined by smectite that occasionally has thin rims of a globular-textured zeolite. Acicular aragonite aggregates are common in cavities, attaining lengths of up to 1 cm. These aragonite crystals are clear, rarely showing a red or yellow color at their base.

Microscopic observations confirm the macroscopic impression that these are relatively unaltered rocks. Only the groundmass within some units has been altered to a dark brown, very fine-grained, poorly crystallized material (smectite?). Sometimes this material also lines vesicles. Radiating aggregates of the

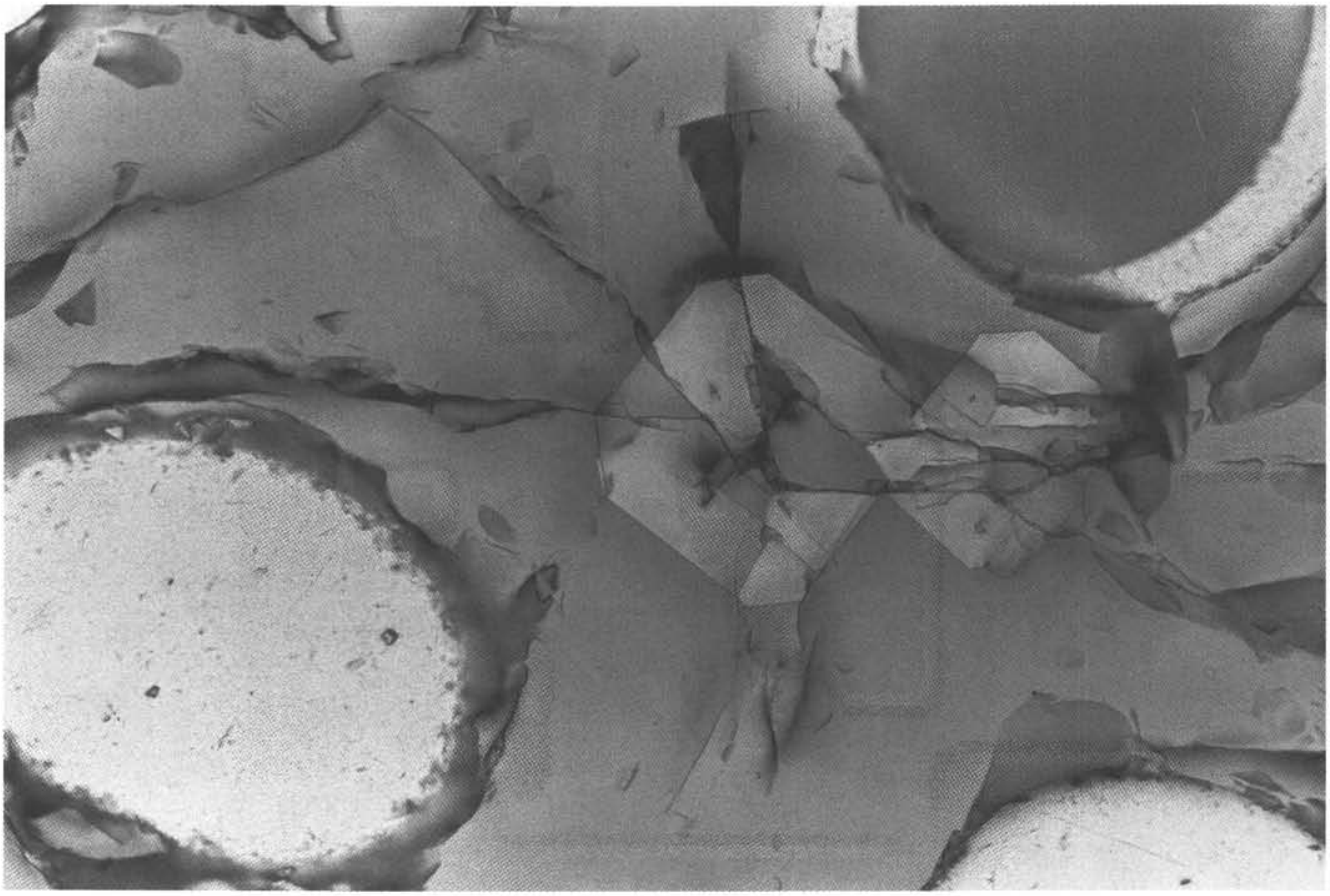

Figure 25. Photomicrograph of cross sections of euhedral orthopyroxene microphenocrysts in vesicular andesitic glass, Unit 2, Section 135-836A-3H-4, 75–150 cm; field of view = 0.3 mm, ordinary light.

acicular zeolites partially and completely fill some vesicles. Their acicular form and the near-parallel extinction angle point to natrolite as the zeolitic species. In three thin sections of specimens from Section 135-836B-3R, aragonite has been identified optically and confirmed by XRD as major vesicle infillings (Fig. 33). The occurrence of aragonite is clearly correlated with the highest Sr content measured in samples from Hole 836 (approximately 300 ppm). In addition, in a single thin section of Sample 135-836B-6R-2 (Piece 1C) an unidentified, dark green, strongly pleochroic, cryptocrystalline mineral (smectite?) lining the wall of a fracture was observed. This core segment contains the zone where internal magma mixing has occurred, and it seems to have undergone atypical alteration processes.

A hand specimen from Section 135-836A-3H-CC shows small sulfide aggregates, the development of which seems to have been controlled, in part, by fractures. These sulfides have partly been oxidized to azurite(?), which suggests that there has been some hydrothermal circulation and activity in the vicinity of Hole 836.

Igneous Geochemistry

Ten samples from Units 2 to 5 were analyzed from Site 836; these data are tabulated in Table 10. Six analyses are from the relatively massive Unit 4; two of these analyses, from the upper part of the unit (135-836B-3R-1, 68–70 cm, and -3R-2, 32–38 cm) are of samples affected by low-temperature alteration, as demonstrated by the pervasive brown to gray-brown coloration in hand specimen. The other four analyses are of dark gray and relatively fresh material. Loss on ignition (LOI; Table 10) values are, however, relatively high in all six samples (1.35%–2.83%), and the relative oxidation states of the samples are unknown. Comparison of the two sets of analyses (Table 11) shows small, but apparently systematic differences in K_2O, Na_2O, CaO, Sr, Rb, Zr, and MgO. Except for MgO, these elements exhibit small increases in the weathered samples.

These small changes, most of which seem to be attributable to alteration, are consistent with the development of aragonite vesicle infillings and partial alteration of the mesostasis by zeolites and clays (thought to be smectitic), leading to mobility of the alkalis and alkaline earths. The differences in Zr, however, suggest that small primary variations in chemistry may also exist within Unit 4 because of crystal fractionation. This is further supported by the small but systematic downhole increase in MgO in Unit 4. The relatively high CaO within the Unit 4 samples is thought to be a primary magmatic feature and not attributable to secondary aragonite precipitation, the modal abundances of which are low (<1%).

In terms of bulk chemistry, Units 2–5 represent contrasting compositions, as shown in Figure 34 in which normative Di, Ol, Hy, and Q are plotted ($Fe_2O_3/FeO = 0.2$). Thus, Unit 2 is andesite, Units 3 and 4 are olivine normative tholeiites, and Unit 5 is quartz normative tholeiite (verging on basaltic andesite). Both Units 2 and 5 are notably enriched in total Fe, coupled with strong depletions in Cr and Ni and relatively enriched V, Zn, Ce, Ba, and Zr (as compared, for example, with the Unit 4 data). These abundance patterns are consistent with fractional crystallization processes as the control on the chemistry of Units 2 and 5. The

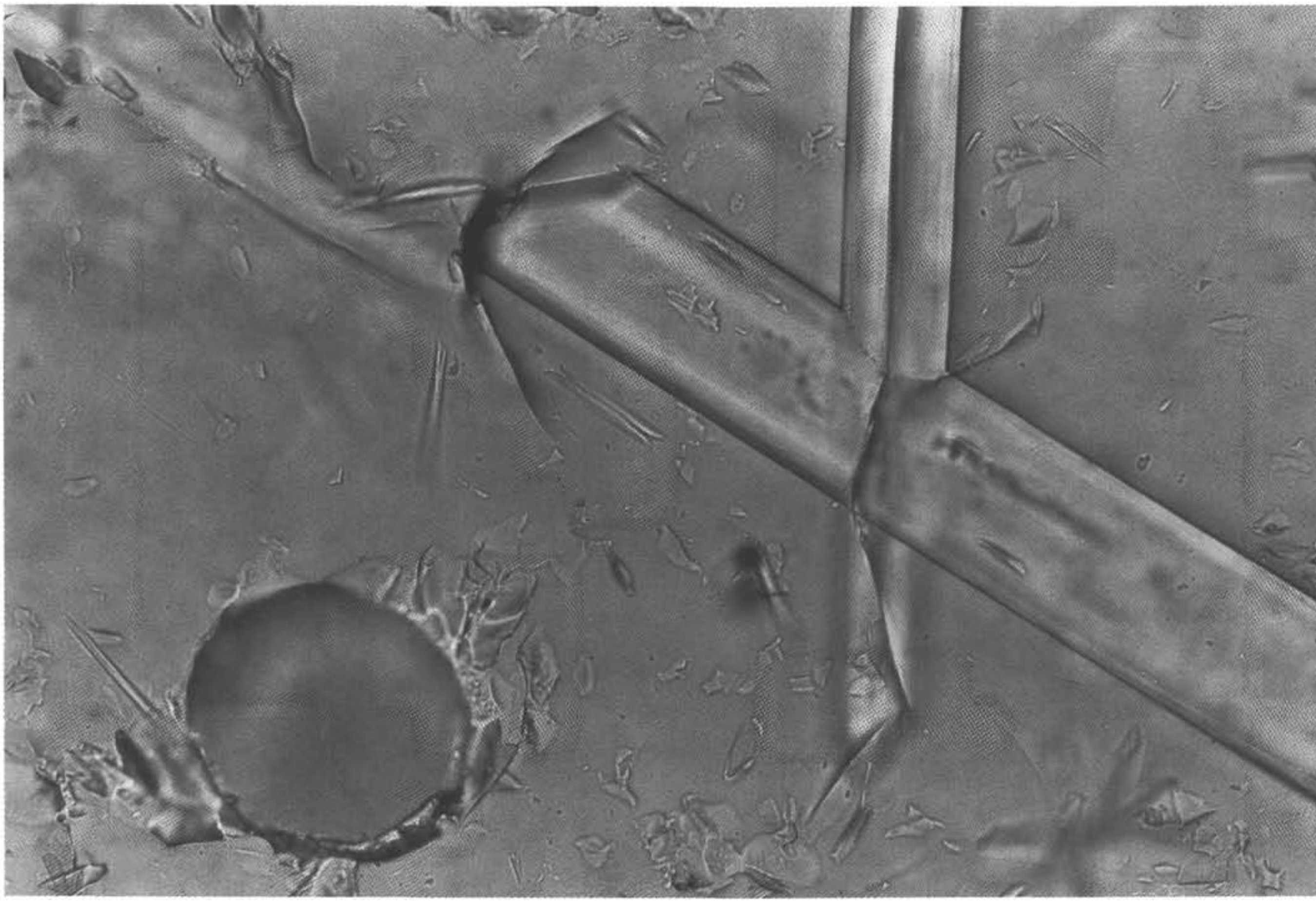

Figure 26. Photomicrograph of intergrown euhedral prismatic orthopyroxene microphenocrysts in vesicular andesitic glass, Unit 2, Section 135-836A-3H-4, 75–100 cm; field of view = 0.3 mm, ordinary light.

occurrence of these more geochemically evolved units at both the top and the lower part of the Site 836 sequence indicates that there is no simple temporal evolution toward more fractionated magmas, and that the recovered interval represents several episodes of fractionation.

Chemical data for Units 2 and 5 are compared to the N-type and T-type Lau Basin basalts and basaltic andesites (Hawkins and Melchior, 1985) and modern Tofua (Tonga) and Kermadec arc basaltic andesites (Ewart and Hawkesworth, 1987) in Table 10 and Figure 35. Compared with the Tofua and Kermadec volcanic arcs, Unit 5 has slightly higher TiO_2, total Fe, P_2O_5, Zr, Y, V, and Ce, and lower Al_2O_3, Sr, Cr, and Ba. These differences are small, and the general comparison indicates compositional similarity, as further emphasized in Figure 35C. Unit 2 also exhibits geochemical abundance patterns similar to the modern arc magmas. Unit 5 is also chemically very close to the transitional-type (T-type) Lau Basin average composition, the only significant differences being the marginally higher concentrations of K_2O, Rb, Ba, Sr, and Zr in Unit 5. It should be noted that none of the Site 836 volcanic rocks show the Zr depletion characteristic of modern Tofua-Kermadec Arc lavas. In this regard, they are more similar to T-type Lau Basin lavas.

The relative enrichments in the large-ion-lithophile elements (LILE), Ce, P, and Sr relative to MORB in Units 2 and 5 are significant (Figs. 35A–35C), as the geochemical patterns are thought to reflect source characteristics associated with a subduction-derived component. Their occurrence in the Lau Basin has important tectonic and petrologic implications and is indicative of distinctive characteristics of their source.

The N-MORB normalized data for the more mafic Unit 4 (Fig. 35B) span a narrow range, except for some scatter among Rb, K, and Sr concentrations, which may reflect selective mobilization of these elements during alteration (Table 11). The mean values of the Unit 4 data are compared in Figure 35D with the range of chemistry shown by the Lau Basin basalts from the active Lau spreading centers (Hawkins and Melchior, 1985; Ernewein et al., in press). It is evident that the Unit 4 chemistry is closely comparable with that for T-type lavas from the active spreading centers (Fig. 35D). Interestingly, the chemistry of Unit 4 also shows some evidence for a subduction-type geochemical signature, although less pronounced than in Units 2 and 5. These Lau Basin data, including Unit 4, do not exhibit the same degree of LILE enrichment and Zr and Ti depletion as seen in the Tofua Arc lavas (Figs. 35C–35D), or as seen in the less evolved tholeiitic basalts from the Kermadec Arc (e.g., Fig. 36); an exception is the olivine tholeiites of Macauley Island, which possess comparable TiO_2 and Zr abundances (Ewart et al., 1977). This is inferred to indicate a generally less extreme preexisting geochemical depletion of high-field strength (HFS) elements and enrichment of the LILE in the magma source(s) of these Lau Basin magmas.

Figure 36 compares selected element abundances of Units 4 and 5 of Site 836 with the range of abundances found in Site 834. The major differences are the lower concentration levels of HFS elements in the Site 836 lavas.

Table 10. Major and trace element data for representative Site 836 samples.

Hole	836A	836B	836B	836B	836B	836A	836B	836A	836B	836B	Lau	Lau	Tongan	Kermadec
Core, section	3H-4	5X-1	3R-1	3R-2	3R-2	7X-1	5R-2	9X-2	7R-1	9M-1	Basin	Basin	basaltic	basaltic
Interval (cm)	75–150	3–9	68–70	32–38	96–100	37–42	84–90	40–47	32–36	43–52	N-type	T-type	andesite	andesite
Unit	2	3	4A	4A	4A	4	4B	4	5					
Depth (mbsf)	15.83	21.23	23.68	24.72	25.36	26.07	36.32	36.78	44.02					
Major elements (wt%):														
SiO_2	56.99	49.34	48.38	48.94	48.96	48.52	48.50	49.17	52.06	52.15	50.24	53.59	52.80	52.83
TiO_2	1.16	0.75	0.75	0.79	0.77	0.76	0.75	0.72	1.14	1.18	0.76	1.05	0.51	0.90
Al_2O_3	14.48	16.62	16.59	16.11	16.37	16.49	16.28	16.49	15.44	15.31	15.80	14.56	16.96	16.98
Fe_2O_3	12.43	8.80	9.29	9.20	9.05	9.48	9.37	9.07	12.16	12.73	10.13	12.82	10.91	12.07
MnO	0.23	0.17	0.15	0.12	0.13	0.14	0.15	0.14	0.20	0.20	0.21	0.21	0.18	0.20
MgO	3.53	8.66	7.98	7.68	8.66	9.43	9.52	9.80	5.33	5.37	7.39	5.27	5.33	4.68
CaO	8.06	14.10	14.46	14.85	14.32	13.93	13.06	13.43	10.72	10.53	13.37	10.22	11.36	9.78
Na_2O	2.91	1.72	1.98	1.96	1.78	1.89	1.81	1.88	2.22	2.27	2.10	2.34	1.56	2.19
K_2O	0.26	0.12	0.11	0.15	0.04	0.04	0.04	0.05	0.30	0.33	0.11	0.17	0.34	0.30
P_2O_5	0.14	0.06	0.06	0.06	0.05	0.05	0.05	0.05	0.11	0.11	0.09	0.11	0.07	0.06
Total	100.17	100.40	99.72	99.84	100.12	100.70	99.50	100.78	99.66	100.15	100.20	99.12	100.02	99.99
LOI	0.78	0.32	2.06	2.76	1.64	2.83	1.49	1.35	0.38	0.27	0.76			
Mg#	36.0	66.1	63.0	62.3	65.4	66.3	66.8	68.1	46.5	45.5	59.1	44.9	49.2	43.4
Trace elements (ppm):														
Nb	2	1	1	1	1	1	0	1	1	1			0.56	0.76
Zr	78	43	56	53	45	46	42	41	57	60	40	45	18	39
Y	34	18	18	18	17	17	17	18	26	27	21	26	12	21
Sr	138	155	356	288	187	228	143	143	153	148	166	98	196	174
Rb	4	3	7	3	0	0	1	1	5	5	2	0.5	4.4	4.9
Zn	102	44	35	51	41	39	57	39	88	87			84	92
Cu	135	100	114	117	110	95	110	109	104	114			133	
Ni	8	117	103	139	118	114	113	106	28	27	94	33	23	16
Cr	9	344	342	318	352	280	293	284	19	15			54	27
V	402	244	234	230	233	267	221	260	404	427			305	346
Ce	13	11	10	4	6	6	9	7	13	13			3.7	6.2
Ba	89	20	11	14	16	13	21	18	53	53	10.8	32.5	88	111

Notes: Analyses for N-type (Sample 123-74-1) and T-type (Samples ANT 225-4) Lau Basin basalts are from Hawkins and Melchior (1985). Average Tonga and Kermadec basaltic andesite (excluding Ata Island) is from Ewart and Hawkesworth (1987) with all iron recalculated as Fe_2O_3. Mg# is $100 \cdot [Mg/(Mg + Fe^{2+})]$, where Fe^{3+}/Fe^{2+} is assumed to be 0.2. LOI = loss on ignition.

PHYSICAL PROPERTIES

Introduction

A full suite of standard ODP physical properties measurements were made at Site 836. Index properties on sediments and sedimentary rocks from Holes 836A and 836B were determined using a pycnometer and a balance, and include bulk density, grain density, porosity, water content, and void ratio. Bulk density was also measured using the continuous gamma-ray attenuation and porosity evaluator (GRAPE) on full APC cores from Hole 836A. Representative samples were selected from the 44.5 m of basalt recovered from Holes 836A and 836B. These samples were run through the 2-min GRAPE process to determine bulk densities; they were also powdered and the weight and volume of the dried powder determined to yield grain density values.

Compressional wave velocities were measured on whole cores using the continuous P-wave logger and on discrete samples using the Hamilton Frame apparatus. The P-wave logger data for the upper 10 m of Hole 836A were lost because of equipment malfunction. Velocities of unconsolidated sediments that could not be removed from the core liner were measured in only one direction. Velocities were measured in both horizontal and vertical directions when possible in unconsolidated sediments and on most of the consolidated sedimentary rocks and basalts.

Vane shear strength was measured on selected undisturbed intervals of fine-grained sediments from Hole 836A until the sediment became too stiff for valid measurements (when cracking of the sediment indicated that the assumption of uniform shear by the vane was no longer valid).

Thermal conductivity was measured on undisturbed sediment cores from Hole 836A and on cut cores of lithified sedimentary rocks and basalts from Hole 836B.

The lithologic units referenced in this section are those described in the "Lithostratigraphy" section (this chapter). Results from laboratory measurements are listed in Tables 12 and 13 and plotted on Figures 37 through 43.

Index Properties

Grain density, wet-bulk density, water content, porosity, and void ratio for sediments and sedimentary rocks from Hole 836A are plotted vs. depth in Figure 37, and values for the gravimetrically determined index properties are listed in Tables 12 and 13.

The few gravimetrically determined index properties show minor variations in the sediments, particularly in a sample from the hyaloclastites at 15.78 mbsf. The bulk and grain density values of the eight samples measured average 1.47 and 2.64 g/cm^3, respectively. The bulk density of the volcanic rock clasts at 15.78 mbsf is substantially higher at 1.7 g/cm^3, and the water content, porosity, and void ratio are correspondingly low. Water content averages 124%, porosity 77%, and the void ratio 3.6. Deviations from the average are observed at 6.4 mbsf, where high water content, porosity, and void ratio were measured from a clayey nannofossil ooze, and at 15.78 mbsf, where low values of these index properties were measured in the hyaloclastite sample.

The GRAPE bulk density have been processed and averaged at 5-cm intervals to remove spurious data points caused by core section ends and void spaces within the core. The GRAPE data (Fig. 38) average 1.52 g/cm^3 and are rather uniform in the upper

Figure 27. Photomicrograph of skeletal olivine phenocryst and plagioclase laths, in fine-grained mesostasis with quench clinopyroxene-plagioclase intergrowths, Unit 3, Section 135-836B-2R-1, 14–16 cm; field of view = 1.5 mm, crossed polarized light.

12 m of the hole. However, significant density increases (to 1.85 g/cm^3) are present between about 13 and 17 mbsf and are caused by the high-density, high-velocity basaltic fragments in thick (to 100 cm) black mafic hyaloclastite units. These high-density peaks are separated by thin, low-density zones that correlate to the interbedded, low-density, nannofossil-dominated clayey oozes. The average density at the base of the measured sediments, from about 17 to 20.3 mbsf (the depth of the last measured GRAPE value) is about 0.5 g/cm^3 higher than in the sediments in the upper 12 m of the hole, reflecting an increased volcanic component.

The bulk density for nine basalt samples (Tables 12–13 and Fig. 39) averages 2.69 g/cm^3 and ranges from 2.49 to 2.80 g/cm^3, whereas grain densities average 2.98 g/cm^3 and range from 2.92 to 3.03 g/cm^3. For comparison, the average value for basalts from a variety of localities is a bulk density of 2.74 g/cm^3 and a grain density of 3.01 g/cm^3 (Johnson and Olhoeft, 1984). The two deepest basalt samples, at 44.57 and 53.39 mbsf, respectively, had significantly lower bulk densities (2.49 g/cm^3) than the average. These relatively low bulk densities are caused by the high vesicularity of the basalts in igneous Unit 5, a moderately phyric plagioclase olivine basalt (see "Igneous Petrology" section, this chapter).

Compressional Wave Velocity

Compressional wave velocity data measured with a Hamilton Frame device and the *P*-wave logger are shown in Figures 40–41 and are listed in Tables 12–13.

In the sediments of Hole 836A (Figs. 40A–40B), the compressional wave velocity is relatively constant with depth for the discrete samples and averages 1521 m/s. The *P*-wave logger data (Fig. 41) give a similar average value of 1527 m/s, but the much greater number of measurements reveals a high degree of variability around the average, with a range of values from 1443 to 1629 m/s. High velocities (to 1629 m/s) are caused by the hyaloclastite layers. The density peaks on the GRAPE data have corresponding high velocity peaks on the *P*-wave logger data, although the highest values of these peaks were not measured by the *P*-wave logger system because of the extreme attenuation of the acoustic wave through the coarse hyaloclastite layers. Increasing velocities at the base of the measured section (the deepest measured *P*-wave logger value was recorded at 20.25 mbsf) are from indurated sediment.

Basalt velocities (Tables 12–13 and Fig. 40C) for 11 samples average 4442 m/s and range from about 3900 to 4800 m/s, values similar to the velocities measured in basalts at Site 834. Velocity measurements of the basalts were made in both horizontal and vertical directions to test for velocity anisotropy in the basalts caused by the flow structure or by differential cooling, but no significant differences were found.

No clear unit-related velocity variations are obvious in the basalt velocities. However, the basalts in igneous Unit 4 (25.7 through 38.2 mbsf in Hole 836A, and 23.46 through 43.8 mbsf in Hole 836B) are characterized by relatively low velocities (4000 to 4400 m/s) in the upper part of the unit (in Unit 4A) compared

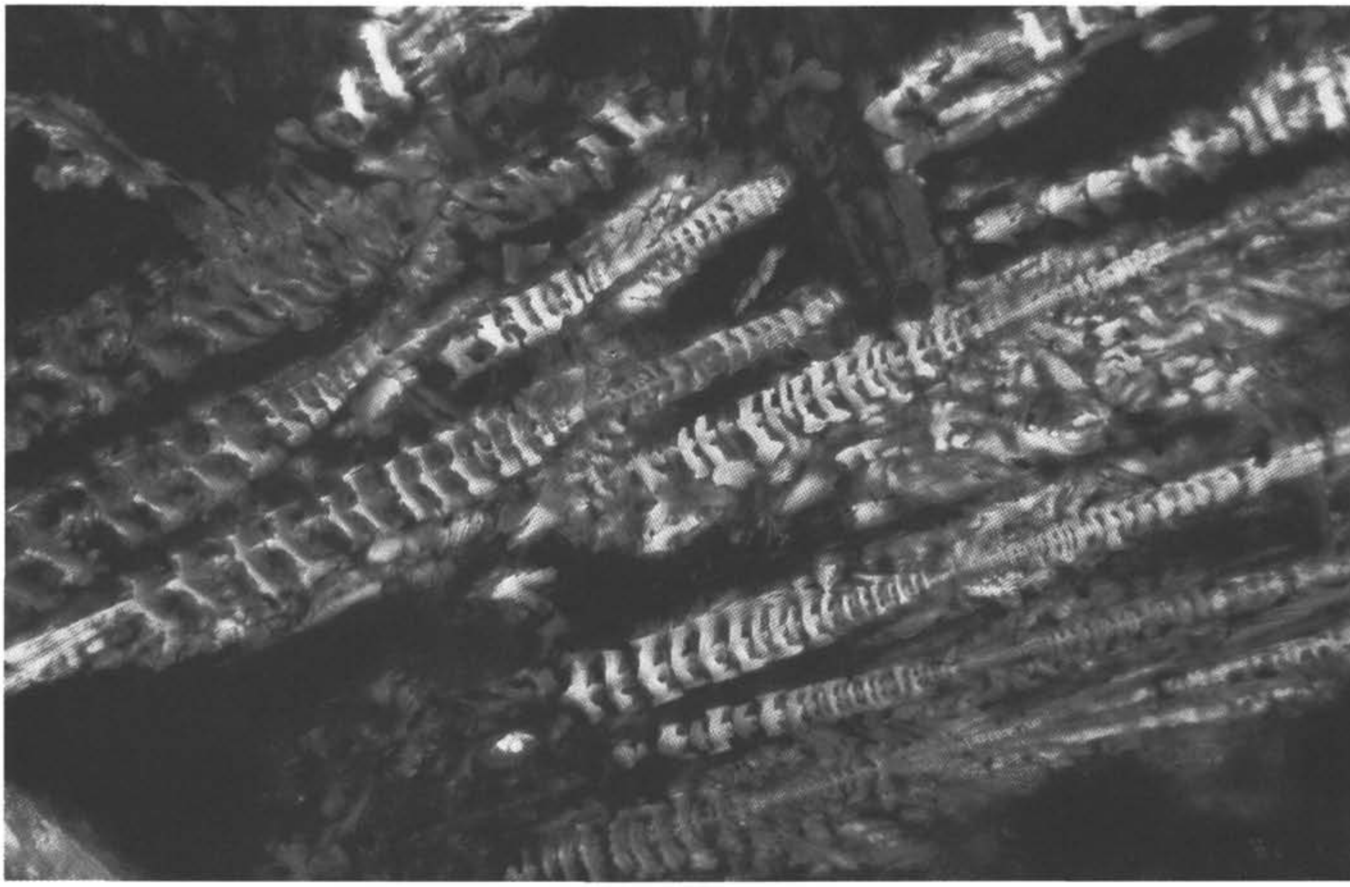

Figure 28. Photomicrograph of skeletal and feathery groundmass clinopyroxene, with interstitial plagioclase, Unit 3, Sample 135-836B-2R-1, 14–16 cm; field of view = 0.3 mm; crossed polarized light.

with velocities of 4600 to 4800 m/s in the lower part of the unit (in Subunit 4B). Unit 4A is affected by extensive alteration, resulting in vesicles lined with clays and zeolites, whereas Subunit 4B is only locally altered (see "Igneous Petrology" section, this chapter). Fluid movement through Subunit 4A may have altered some of the basalt grains to clays, which could lower the measured velocity. However, a high velocity was also measured in altered samples from Subunit 4A, so not all parts of the unit are affected equally. The velocity differences may also simply reflect small differences in the vesicularity of the basalts, with the differences not obvious in hand specimen.

The velocities of two samples from igneous Unit 5 differ significantly. This unit is composed of multiple flow units, and the low-velocity sample from the upper part of the unit may have come from a margin of one of these flow units, whereas the high-velocity sample may have come from the interior of a more massive flow unit deeper within Unit 5.

Undrained Vane Shear Strength

Values of undrained shear strength were obtained using the standard on-board miniature vane shear apparatus on unconsolidated sediments in Hole 836A; the results are plotted in Figure 42 and reported in Table 12. The shear strength reflects the smoothly increasing consolidation of the fine-grained sediments from the upper 20 mbsf of the hole. Values remain low (<10 kPa) to 10 mbsf, then rapidly increase at the top of and between the hyaloclastite layers, reaching a maximum value of 45.2 kPa at the last measured point (18.83 mbsf).

Thermal Conductivity

In soft sediment cores, all values were obtained using needle probes inserted through core liners into full core sections. For basalts, thermal conductivity was measured on the split core face. The thermal conductivity results for both full and split cores from Holes 836A and 836B are illustrated in Figure 43 and listed in Tables 12–13.

Thermal conductivity in the sedimentary section of Hole 836A averages 0.87 W/(m · °K). A slight increase (to 0.95 W/[m · °K]) in conductivity at 9.3 mbsf correlates with an interval of pure clayey nannofossil ooze, and a decrease in conductivity (to 0.77 W/[m · °K]) at 15.8 mbsf occurs in a hyaloclastite layer.

Thermal conductivity on six basalt samples averages 1.4 W/(m · °K), similar to values in basalts at Sites 834 and 835. Too few measurements were made to define trends within the basalts.

Temperature Measurements

No temperature measurements were made at Site 836.

Discussion

The most apparent correlation in the physical properties data from Site 836 is high velocity and high density values in the hyaloclastite layers within the sedimentary section. This correlation is readily seen on the GRAPE and *P*-wave logger data. Marked variations in the basalt velocity values could be a result of alteration, but they may simply reflect the variable vesicularity of the basalts as we suggested for the basalt velocities at Site 834.

Figure 29. Photograph of acicular, pseudohexagonal aragonite developed within an open vesicle, Section 135-836A-8X-1, Piece 4B; photograph width = 2 cm.

Otherwise, the physical properties at this site for both the sediments and the basalts are similar to the properties measured at Sites 834 and 835.

DISCUSSION

The principal objective for Site 836 was to determine of the nature of the basement rock and to deduce its mantle-source characteristics and petrogenetic history. In addition, we hoped that the dating of the sedimentary cover and the assessment of the evolutionary trends using biostratigraphic data would pinpoint a minimum age of basement formation. This age would be crucial for the testing of models of crustal formation in the central Lau Basin.

Site 836 was selected on the basis of inconclusive seismic reflection profiles, although support for suggestions of a significant sediment thickness came from 3.5-kHz seismic profiles. Coring success at Site 836 was limited because of (1) a restricted sedimentary sequence only 20 m thick, and (2) operational difficulties involving the drilling of fractured and relatively unaltered young basalt. After only 58 m of total penetration, we decided to stop coring at the site and to divert efforts to obtain the site objectives at one of the alternate locations. Trace and minor element chemistry of the igneous rocks at Site 836 indicate that they consisted of basalts and andesitic hyaloclastite, the andesitic hyaloclastite being more evolved than the igneous lithologies cored at Sites 834 and 835. The rapidly deposited volcaniclastic sediments immediately overlying the "basement" have similar relatively SiO_2-rich compositions, and these are overlain by hemipelagic deposits with subordinate interspersed volcanic glass. The middle Pleistocene age for foraminifers and calcareous nannofossils contained by the lowermost sediments is consistent with the paleomagnetic determination that the cored sediments lie entirely within the Brunhes Chron; provisionally, the site may mark the oldest crust generated at the ELSC. The thin (20 m) sediment cover at the site suggests that sediment removal associated with bottom-water currents may have occurred, situated as it is in a narrow north-northeast basinal trough.

REFERENCES

Blow, W. H., 1969. Late middle Eocene to Recent planktonic foraminiferal biostratigraphy. *In* Brönniman, P., and Renz, H. H. (Eds.), *Proceedings of the First International Conference on Planktonic Microfossils, Geneva, 1967:* Leiden (E. J. Brill), 1:199–422.

Bednarz, U., and Schmincke, H.-U., in press. Basaltic andesitic to rhyodacitic submarine volcanoes in the Troodos Extrusive Series (Cyprus, Eastern Mediterranean). *J. Geophys. Res.*

Chaproniere, G.C.H., in press. Pleistocene to Holocene planktic foraminiferal biostratigraphy of the Coral Sea, offshore Queensland, Australia. *BMR J. Aust. Geol. Geophys.*

Church, B. N., and Johnson, W. M., 1980. Calculation of the refractive index of silicate glasses from chemical composition. *Geol. Soc. Am. Bull.*, 91:619–625.

Emeis, K.-C., and Kvenvolden, K. A., 1986. Shipboard organic geochemistry on *JOIDES Resolution. ODP Tech. Note,* No. 7.

Ernewein, M., Pearce, J. A., Bloomer, S. H., Parson, L. M., Murton, B. J., and Johnson, L. E., in press. Geochemistry of Lau Basin volcanic rocks: influence of ridge segmentation and arc proximity. *Contrib. Mineral. Petrol.*

Ewart, A., Brothers, R. N., and Mateen, A., 1977. An outline of the geology and geochemistry, and the possible petrogenetic evolution of the volcanic rocks of the Tonga-Kermadec-New Zealand island arc. *J. Volcanol. Geotherm. Res.*, 2:205–250.

Ewart, A., and Hawkesworth, C. J., 1987. The Pleistocene-Recent Tonga-Kermadec arc lavas: interpretation of new isotope and rare earth data in terms of a depleted mantle source model. *J. Petrol.*, 28:495–530.

Hawkins, J. W., 1976. Petrology and geochemistry of basaltic rocks of the Lau Basin. *Earth Planet. Sci. Lett.*, 28:283–298.

———, 1985. Low-K rhyolitic pumice from the Tonga Ridge. *In* Scholl, D. W., and Vallier, T. L. (Eds.), *Geology and Offshore Resources of Pacific Island Arcs—Tonga Region*. Circum-Pac. Counc. Energy Miner. Resour., Earth Sci. Ser., 2:171–178.

———, 1988. Cruise Report—PAPATUA Expedition, Leg 04, R/V *Thomas Washington*. SIO Ref. Ser., No. 88-14.

———, 1989. Cruise Report—ROUNDABOUT Expedition, Legs 14, 15, R/V *Thomas Washington*. SIO Ref. Ser., No. 89-13.

Hawkins, J. W., and Melchior, J. T., 1985. Petrology of Mariana Trough and Lau Basin basalts. *J. Geophys. Res.*, 90:11,431–11,468.

Hawkins, J. W., Melchior, J., Florendo, F., and Nilsson, K., 1989. Evolution of backarc basin magmas and their mantle sources—examples from the Lau Basin and Mariana Trough. *Eos*, 70:1389.

Johnson, G. R., and Olhoeft, G. R., 1984. Density of rocks and minerals. *In* Carmichael, R. S. (Ed.), *CRC Handbook of Physical Properties of Rocks* (Vol. 3): Boca Raton, FL (CRC Press), 1–38.

Lawver, L., Hawkins, J. W., and Sclater, J. G., 1976. Magnetic anomalies and crustal dilation in the Lau Basin. *Earth Planet. Sci. Lett.*, 33:27–35.

Malahoff, A., Kroenke, L. W., Cherkis, N., and Brozena, J., in press. Magnetic and tectonic fabric of the North Fiji Basin and Lau Basin. *In* Kroenke, L., and Eade, J. V. (Eds.), *Basin Formation, Ridge Crest Processes, and Metallogenesis in the North Fiji Basin*. Circum-Pac. Counc. Energy Miner. Resour., Earth Sci. Ser.

Murthy, S.K.M., 1990. Seafloor spreading magnetic lineations in Lau back-arc basin, southwest Pacific. *Inst. Oceanogr. Sci. Deacon Lab. Tech. Rep.*

Nilsson, K., Florendo, F. F., and Hawkins, J. W., 1989. Petrology of a nascent triple junction, northeastern Lau Basin. *Eos*, 70:1389.

Parson, L. M., et al., 1989. RRS *Charles Darwin* Cruise 33/88, 5 May–1 June 1988. Geophysical and geological investigations of the Lau Basin, SW Pacific. *Inst. Oceanogr. Sci. Deacon Lab. Cruise Rep.*, No. 206.

Parson, L. M., Pearce, J. A., Murton, B. J., and RRS *Charles Darwin* Scientific Party, 1990. Role of ridge jumps and ridge propagation in the tectonic evolution of the Lau back-arc basin, southwest Pacific. *Geology*, 18:470–473.

Schmincke, H.-U., 1981. Ash from vitric muds in deep sea cores from the Mariana Trough and fore-arc regions (south Philippine Sea) (Sites 453, 454, 455, 458, 459). *In* Hussong, D. M., Uyeda, S., et al., *Init. Repts. DSDP*, 60: Washington (U.S. Govt. Printing Office), 473–481.

Schmincke, H.-U., and Bednarz, U., in press. Pillow, sheet-flow, and breccia-flow volcanoes and volcano-tectonic-hydrothermal cycles in the northeastern Troodos Extrusive Series. *In* Malpas, J., Moores, E., Panayiotou, A., and Xenophontos, C. (Eds.), *Troodos '87—Ophiolites and Oceanic Lithosphere*. Geol. Surv. Dep., Nicosia (Cyprus).

Sclater, J. G., 1972. Heat flow and elevation of the marginal basins of the western Pacific. *J. Geophys. Res.*, 77:5685–5696.

Sun, S.-S., and McDonough, W. F., 1989. Chemical and isotopic systematics of oceanic basalts: implications for mantle composition and processes. *In* Saunders, A. D., and Norry, M. J. (Eds.), *Magmatism in the Ocean Basins*. Geol. Soc. Spec. Publ. London, 42:313–345.

von Stackelberg, U., 1990. R.V. *Sonne* Cruise SO48: summary of results testing a model of mineralisation. *Mar. Min.*, 9:135–144.

Weissel, J. K., 1977. Evolution of the Lau Basin by the growth of small plates. *In* Talwani, M., and Pitman, W. C. (Eds.), *Island Arcs, Deep Sea Trenches and Back Arc Basins*. Am. Geophys. Union, Maurice Ewing Series, 1:429–436.

Ms 135A-106

NOTE: All core description forms ("barrel sheets") and core photographs have been printed on coated paper and bound separately as Part 2 of this volume, beginning on page 681.

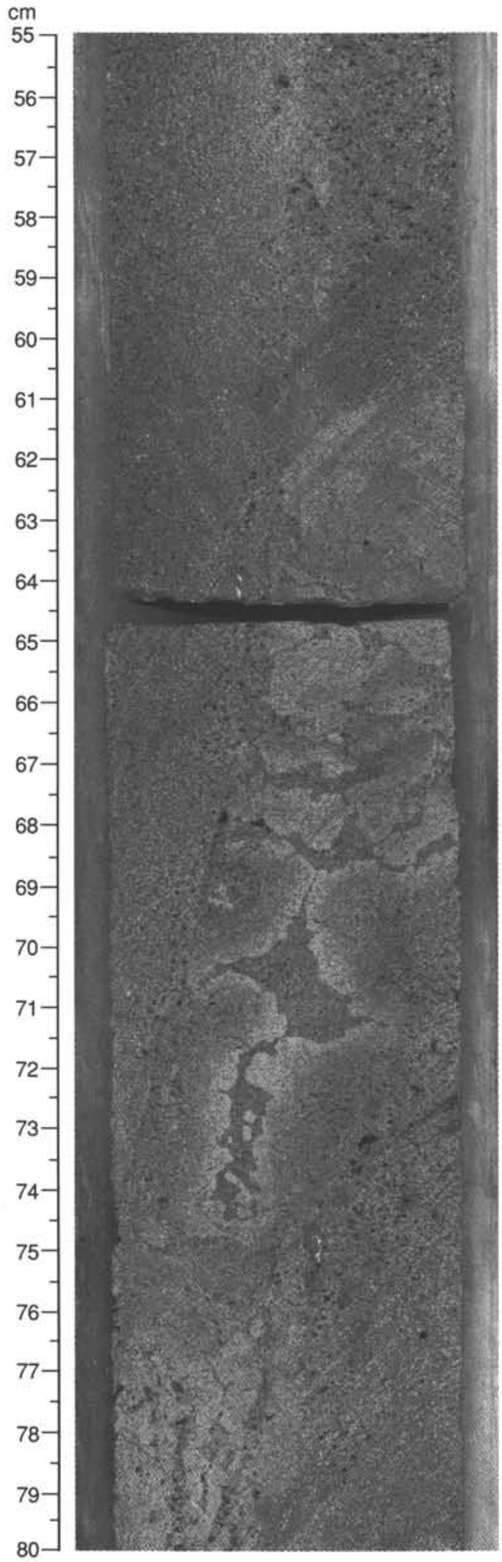

Figure 30. Closeup photograph of Section 135-836B-6R-2, 55–80 cm, showing the zone of complex internal magma-mixing flow boundaries and quenched contacts, Unit 4.

Figure 31. Photomicrograph of ophitic texture developed in Unit 4, Section 135-836A-7X-1, 42–43 cm; field of view = 3 mm; crossed polarized light.

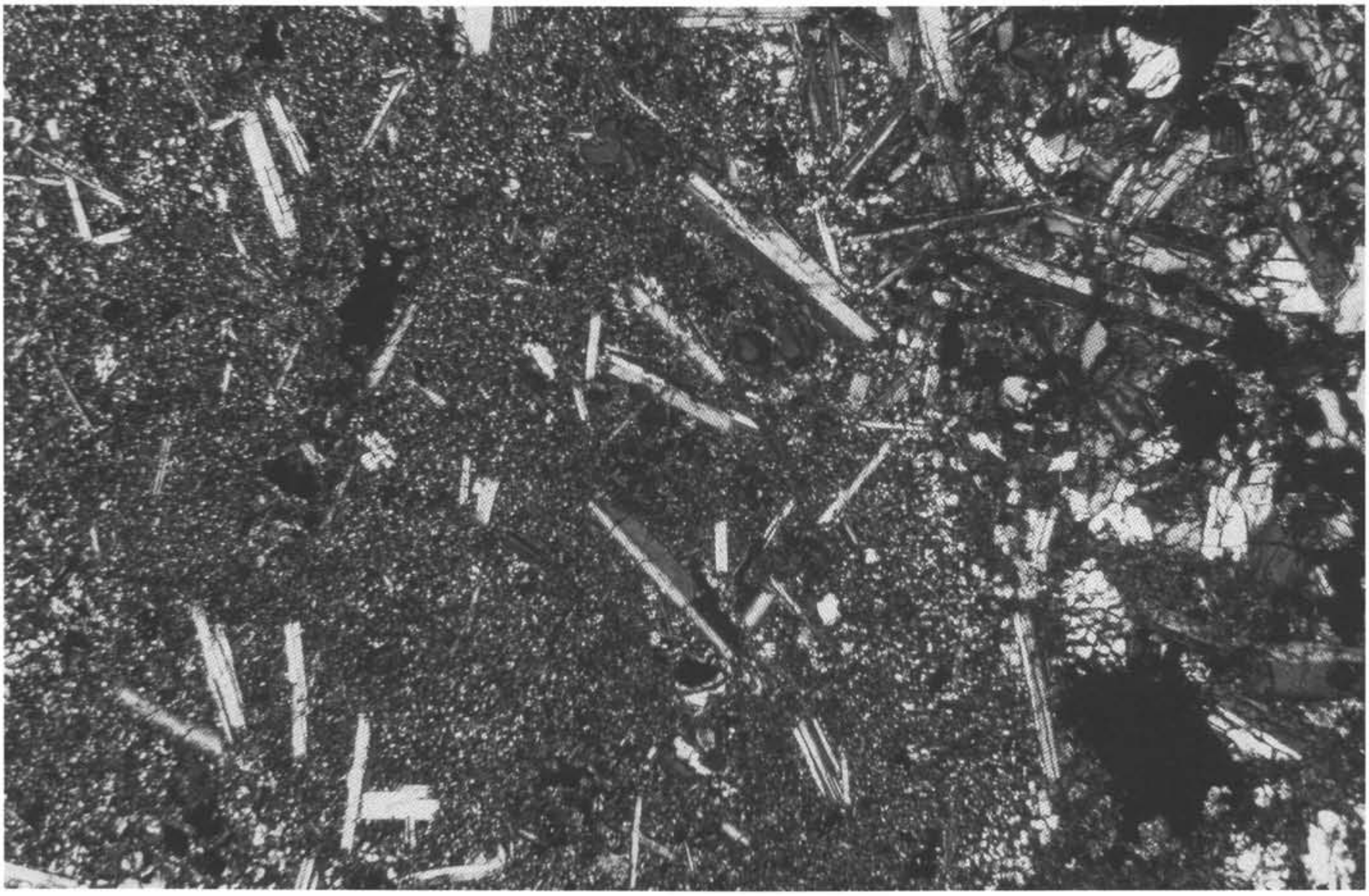

Figure 32. Photomicrograph of Unit 4 contrasting grain-size lithologies, which have been interpreted as being caused by internal magma mixing and quenching, Section 135-836B-6R-2, 59–63 cm; phenocrystal plagioclase visible; field of view = 5 mm, crossed polarized light.

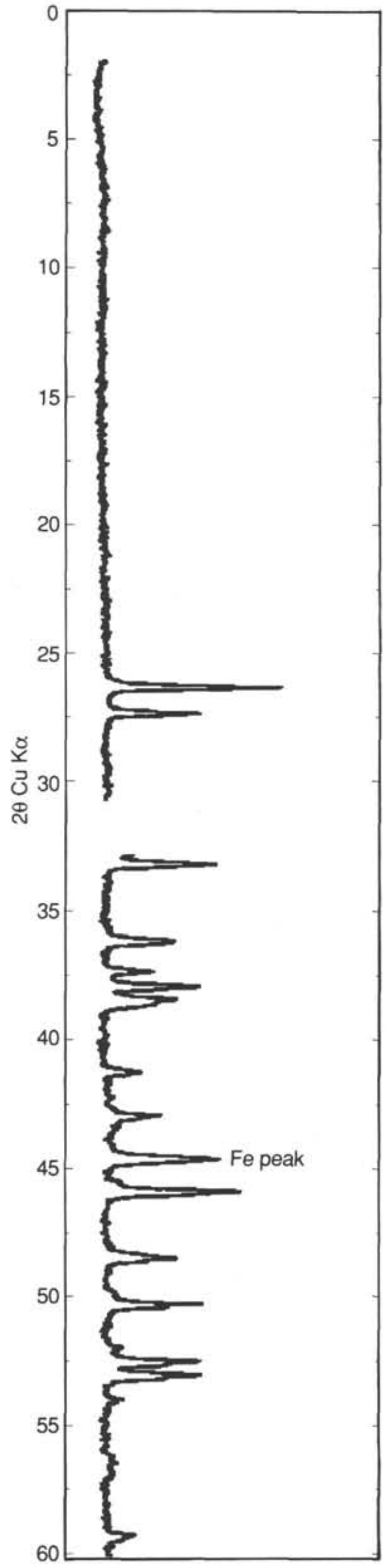

Figure 33. X-ray diffraction pattern of hand-picked acicular infilling within Section 135-836A-8X-1, Piece 4B, confirming aragonite as the only mineral present. Fe peak at 44.62° is a result of steel reflection. Plot is 2θ against relative intensity.

Table 11. Summary of the geochemical differences between altered and fresh samples in Unit 4 at Site 836.

	Altered (2 samples) (brown to gray-brown)		Fresh (4 samples) (dark gray)	
Element	Mean	Range	Mean	Range
K_2O (%)	0.13	0.11–0.15	0.04	0.4–0.05
Na_2O (%)	1.97	1.96–1.98	1.84	1.78–1.89
CaO (%)	14.66	14.46–14.85	13.69	13.06–14.32
Sr (ppm)	322	288–356	175	143–228
Rb (ppm)	5	3.7	0.5	0–1
Zr (ppm)	54.5	53–56	43.5	41–46
MgO (%)	7.84	7.68–7.98	9.35	8.66–9.80

Notes: The two altered samples are from the upper part of Unit 4; they have been affected by low-temperature alteration, as demonstrated by the pervasive brown to gray-brown coloration.

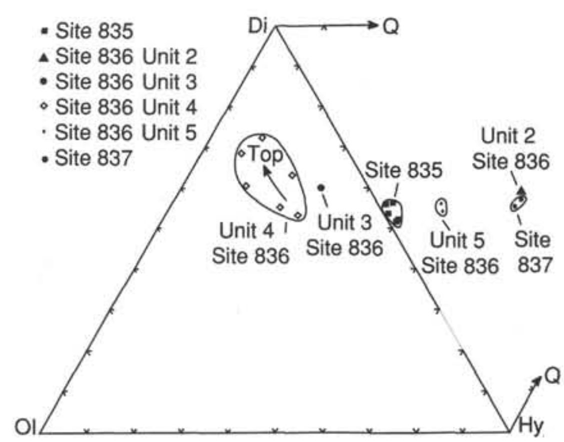

Figure 34. Normative Di-Ol-Hy-Q plot for the analyzed samples from Holes 835, 836, and 837. The assumed Fe_2O_3/FeO ratio is 0.2.

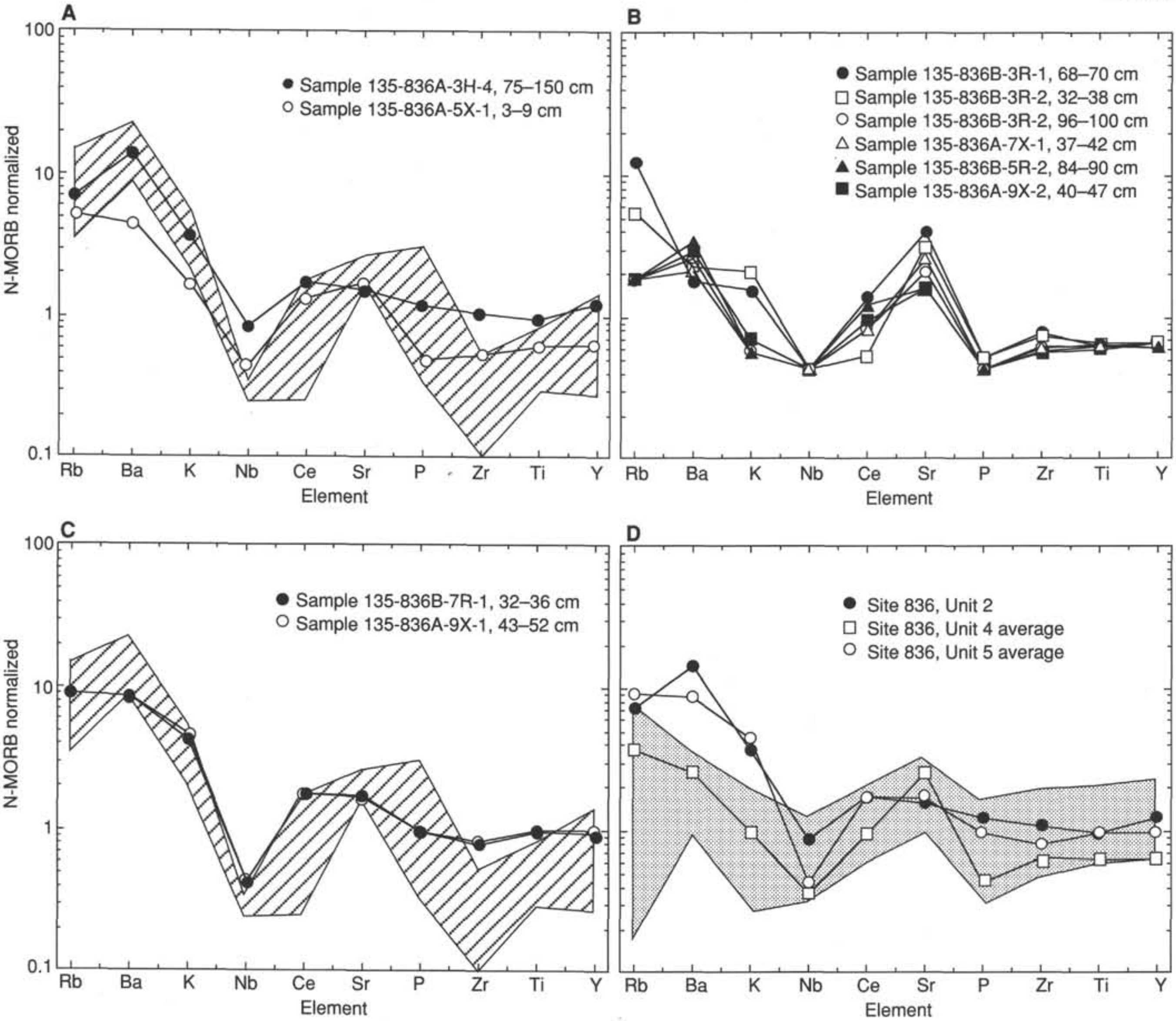

Figure 35. Trace elements normalized to N-MORB for samples from Units 2, 4, and 5, Holes 836A and 836B. **A.** Units 2 and 3. **B.** Unit 4. **C.** Unit 5. **D.** Averages. The striped patterns in Figures 35A and 35C are the ranges of abundances found in the modern Tofua Arc volcanics (excluding Ata; after Ewart and Hawkesworth, 1987), whereas the stippled area in Figure 35D is the range of abundances found in the modern Lau Basin basalts (Ernewein et al., in press; Hawkins and Melchior, 1985). The lowest Ba, Rb, and K values for the Lau Basin are for Samples STO-63-1 and STO-63-4 from the Central Lau Spreading Center (CLSC; Hawkins and Melchior, 1985). Normalizing values from Sun and McDonough (1989).

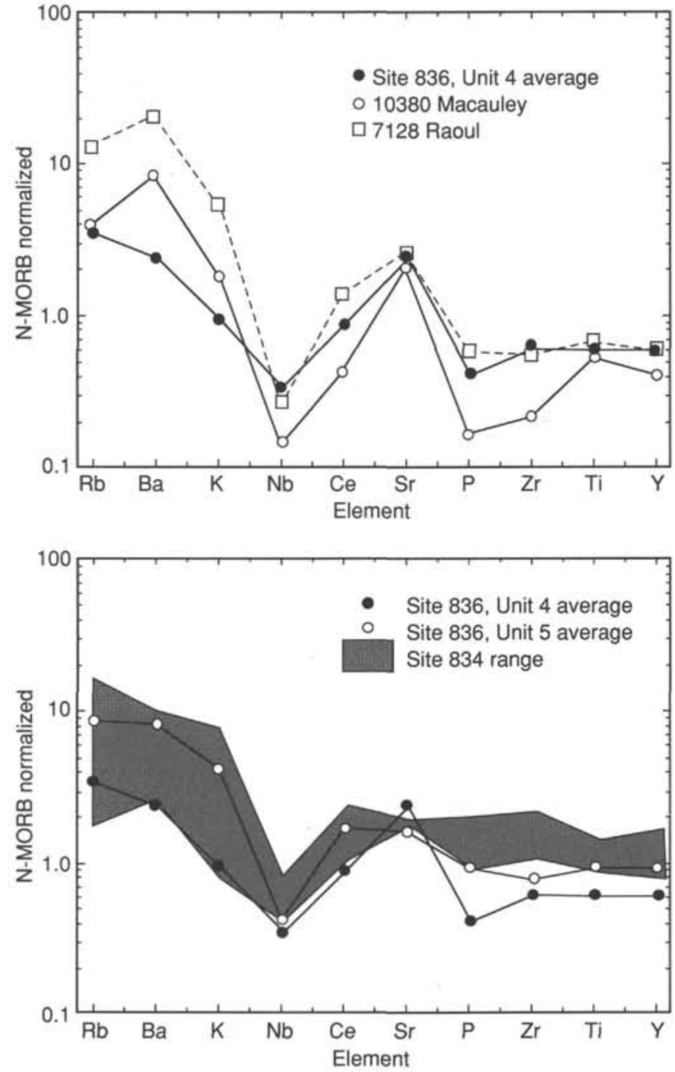

Figure 36. Trace elements normalized to N-MORB comparing the averaged data from Units 4 and 5 (Holes 836A and 836B), the range of Site 834, and two basalts from Macauley and Raoul islands in the Kermadec Arc (Ewart et al., 1977; J. A. Pearce, unpubl. data, 1991).

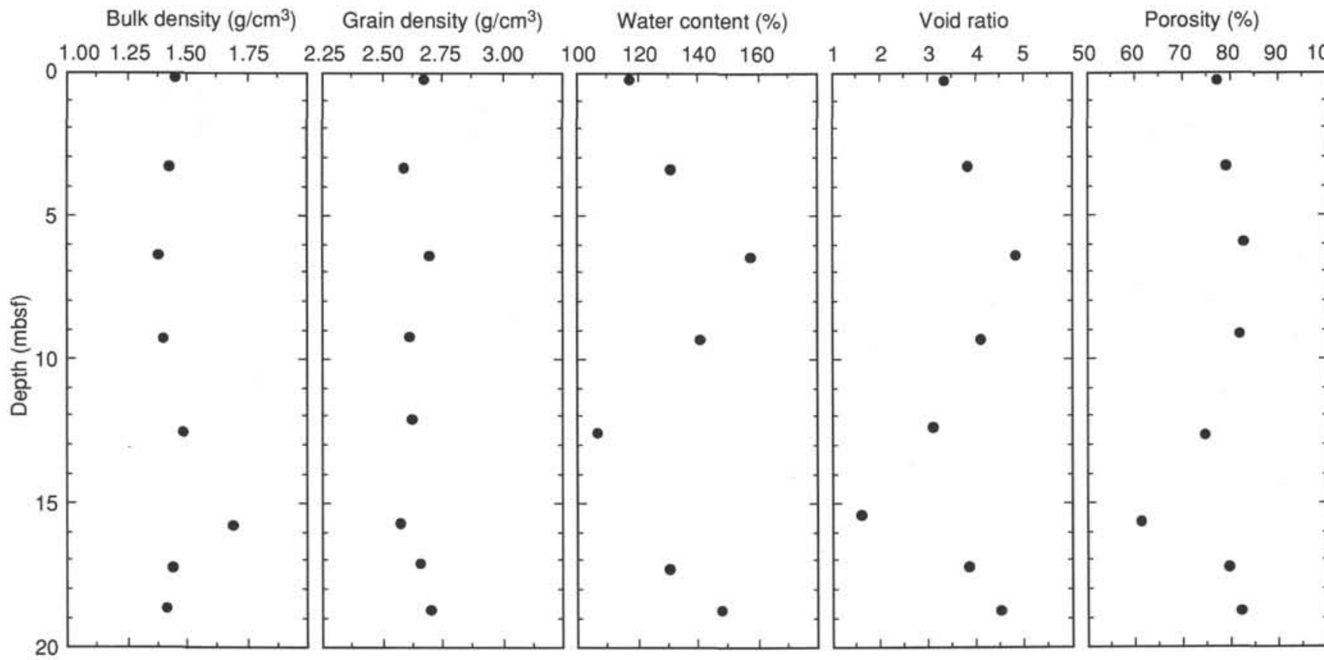

Figure 37. Index property data (bulk density, grain density, water content, porosity, and void ratio) vs. depth, Hole 836A.

Table 12. Physical properties data, Hole 836A.

Core, section, interval (cm)	Depth (mbsf)	Su (kPa)	TC (W/[m · °K])	Bulk density (g/cm³)	Grain density (g/cm³)	Porosity (%)	Water content (%)	Void ratio	V_p (m/s)	V_p dir.
135-836A-										
1H-1, 30–32	0.30			1.46	2.68	77	117	3.3	1530	C
1H-1, 34–35	0.34	4.1								
2H-2, 60	3.30		0.9279							
2H-2, 68–70	3.38			1.43	2.59	79	131	3.8	1546	C
2H-2, 75–76	3.45	3.7								
2H-3, 60	4.80		0.8628							
2H-4, 38–40	6.08								1558	C
2H-4, 60	6.30		0.8292							
2H-4, 70–72	6.40			1.39	2.69	83	158	4.8	1501	C
2H-4, 75–76	6.45	4.1								
2H-6, 60	9.30		0.9455							
2H-6, 70–72	9.40			1.41	2.60	80	141	4.1	1489	C
2H-6, 75–76	9.45	8.5								
3H-2, 41–44	12.61			1.49	2.63	75	106	3.0	1529	C
3H-2, 46–47	12.66	23.1								
3H-2, 60	12.80		0.8919							
3H-2, 120–121	13.40	37.5								
3H-3, 60	14.98		0.8352							
3H-4, 70–71	15.78			1.70	2.57	59	56	1.5		
3H-4, 60	15.80		0.7777							
3H-5, 65–68	17.23			1.44	2.67	80	131	3.9	1540	C
3H-5, 75–76	17.33	45.0								
3H-6, 65–68	18.73			1.41	2.71	82	148	4.6	1521	C
3H-6, 60	18.80		0.9025							
3H-6, 75–76	18.83	45.2								
7X-1, 39–41	26.09			2.75	2.98				4665	A
8X-1, 105–107	32.25			2.79	2.94				4600	A
9X-1, 129–131	36.49			2.74	3.03				4750	A

Notes: Su = undrained vane shear strength, TC = thermal conductivity, V_p = compressional (*P*-wave logger) velocity, and V_p dir. = velocity direction, where A is the vertical velocity along the core and C is the horizontal velocity perpendicular to the core face.

Table 13. Physical properties data, Hole 836B.

Core, section, interval (cm)	Depth (mbsf)	TC (W/[m · °K])	Bulk density (g/cm³)	Grain density (g/cm³)	V_p (m/s)	V_p dir.
135-836B-						
1R-3, 60	3.60	0.8406				
3R-2, 3–5	24.53				4258	A
3R-2, 3–5	24.53				4461	B
3R-2, 82–88	25.32	1.4233				
3R-2, 140–142	25.90		2.73	2.98	4165	A
3R-2, 140–142	25.90				4139	B
3R-2, 140–142	25.90				4216	C
4R-1, 49–55	28.99	1.1593				
4R-1, 62–64	29.12		2.69	2.95	4090	A
4R-1, 62–64	29.12				4091	B
4R-1, 62–64	29.12				4001	C
5R-2, 76–86	36.26	1.4356				
5R-2, 89–91	36.37		2.75	2.99	4560	A
5R-2, 89–91	36.37				4572	B
5R-2, 89–91	36.37				4448	C
6R-1, 7–9	39.07				4688	A
6R-1, 7–9	39.07				4664	B
6R-1, 69–80	39.69	1.3968				
6R-1, 120–122	40.20		2.80	3.00	4694	A
6R-1, 120–122	40.20				4790	B
6R-1, 120–122	40.20				4633	C
7R-1, 68–78	44.38	1.6252				
7R-1, 87–89	44.57		2.49	3.06	4019	A
7R-1, 87–89	44.57				4055	B
7R-1, 87–89	44.57				3910	C
8R-1, 9–11	53.39		2.49	2.92	4298	A
8R-1, 9–11	53.39				4425	B
8R-1, 9–11	53.39				4338	C
9M-1, 82–90	58.30	1.4187				

Notes: TC = thermal conductivity, V_p = compressional (P-wave logger), and V_p dir. = velocity direction, where A is the vertical velocity along the core, B is the horizontal velocity parallel to the cut core face, and C is the horizontal velocity perpendicular to the core face.

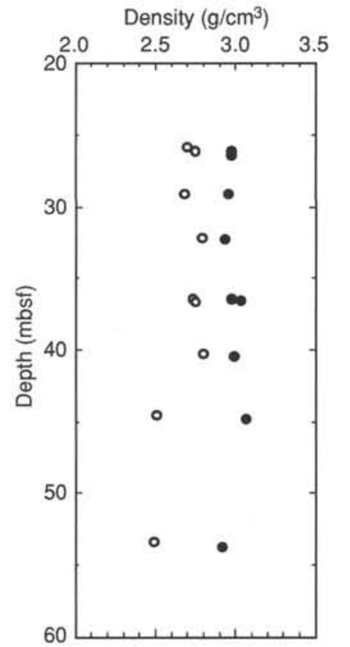

Figure 39. GRAPE bulk density (2 min) and gravimetrically determined grain density for basalts from Holes 836A and 836B. Bulk-density variations are mainly caused by the vesicularity of the basalts. Open circles = bulk density and filled circles = grain density.

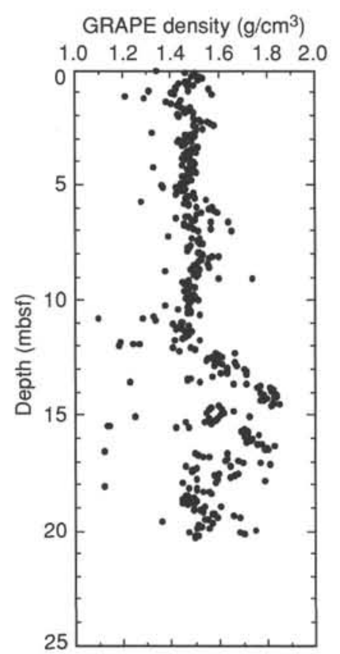

Figure 38. GRAPE bulk density vs. depth, Hole 836A. Average GRAPE bulk density is similar to the bulk density measured on the discrete samples illustrated in Figure 37.

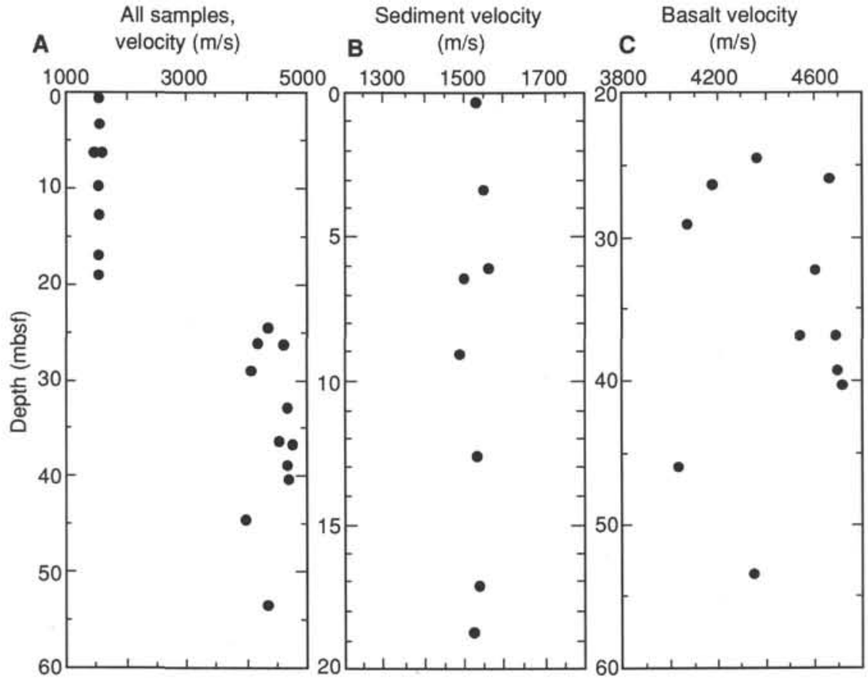

Figure 40. **A.** Compressional wave velocity vs. depth for all samples from Holes 836A and 836B. **B.** Compressional wave velocity vs. depth for sedimentary strata from Hole 836A (0–20 mbsf). **C.** Compressional wave velocity vs. depth for basalt samples from Holes 836A and 836B (20–60 mbsf).

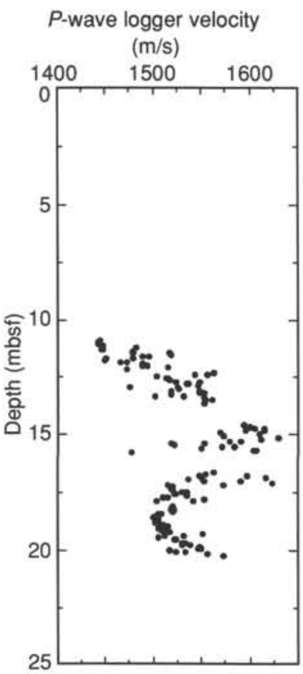

Figure 41. *P*-wave logger data vs. depth, Hole 836A.

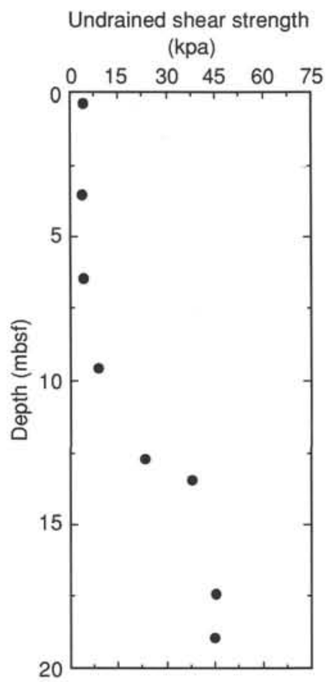

Figure 42. Undrained vane shear strength vs. depth, Hole 836A.

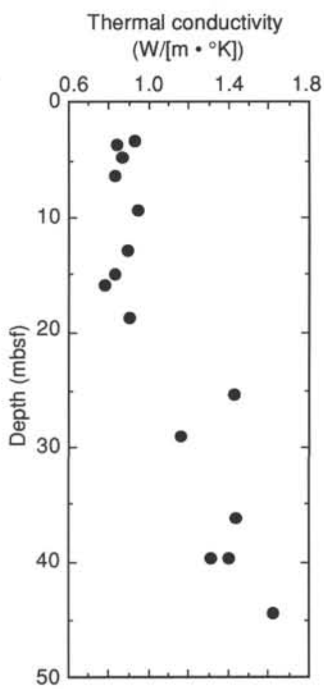

Figure 43. Thermal conductivity vs. depth, Holes 836A and 836B.